ELECTRONIC, OPTICAL, AND TRANSPORT PROPERTIES OF WIDEGAP II-VI SEMICONDUCTORS

By

JIANZHONG LI

A DISSERTATION PRESENTED TO THE GRADUATE SCHOOL
OF THE UNIVERSITY OF FLORIDA IN PARTIAL FULFILLMENT
OF THE REQUIREMENTS FOR THE DEGREE OF
DOCTOR OF PHILOSOPHY

UNIVERSITY OF FLORIDA

1997

Dedicated to my beloved China and family

ACKNOWLEDGMENTS

The author would like to thank his thesis advisor, Professor C. J. Stanton, for guidance and encouragement throughout the course of this thesis. Also the author would like to thank Professor K. A. Muttalib for wholehearted support during his years at the University of Florida.

The author is honored and grateful to have Professors John R. Klauder, David H. Reitze, and Joseph H. Simmons serve on his supervisory committee.

Professors J. H. Simmons, R. M. Park and P. H. Holloway are instrumental to this thesis by providing experimental data and discussions. Dr. G. D. Sanders offered immeasurable assistance whenever needed. Dr. V. J. Sosa greatly improved the accuracy of the XPS data.

The author appreciates a dissertation fellowship from the Threadgill family and enjoyed every minute during his stay at the Mikroelektronik Centret (MIC) at the Technical University of Denmark.

Gratitude goes to those friends who played soccer and bridge with the author during these years; to those officemates who shared their thoughts with the author; and to those secretaries in the Physics offices, in particular, Julie Smith and Cathy Knudsen, without whose technical assistance it would have been impossible for the author to make it through. Special thanks go to the Graduate Seminar and pizzas.

Last but not the least, the author would like to extend his appreciation to his family's unlimited and invaluable encouragement and support.

TABLE OF CONTENTS

Page

ACKNOWLEDGMENTS . . . iii

LIST OF TABLES . . . vii

LIST OF FIGURES . . . viii

ABSTRACT . . . xiii

PARTS

I INTRODUCTION . . . 2

- 1. OVERVIEW . . . 2
- 2. IIB-VIA COMPOUND SEMICONDUCTORS . . . 8
  - ZnS . . . 8
  - ZnSe . . . 12
  - CdTe . . . 13

II OPTICAL PROPERTIES AND XPS SPECTRUM OF ZnS . . . 17

- 3. INTRODUCTION . . . 17
- 4. THEORIES . . . 19
  - X-ray Photoemission Spectroscopy (XPS) . . . 19
  - Linear Optical Properties—Interband Transition Theory . . . 21
- 5. RESULTS AND DISCUSSION . . . 24
- 6. CONCLUSIONS . . . 35

III QUANTUM CONFINEMENT EFFECTS IN CdTe . . . 37

- 7. INTRODUCTION . . . 37
- 8. THEORIES . . . 44
  - Truncated Crystal Approximation . . . 44
  - Envelop Function Approximation . . . 47
  - Hamiltonian Models . . . 49
    - 3D 30 × 30 $\vec{k} \cdot \vec{p}$ Theory . . . 51
    - 1D 2 × 2 $\vec{k} \cdot \vec{p}$ Model . . . 52
    - 1D White-Sham Model . . . 52

9. RESULTS . . . 54
    Truncated Crystal Approximation . . . 55
    Envelop Function Approximation . . . 59

10. DISCUSSION . . . 66
    Truncated Crystal Approximation . . . 66
    Envelop Function Approximation . . . 68

11. CONCLUSIONS . . . 70

IV STATIC SCREENING AND MOBILITY IN n-ZnSe . . . 72

12. INTRODUCTION . . . 72

13. BACKGROUND . . . 75

14. THEORIES . . . 79
    Chemical Potential . . . 79
    Electronic Mobility due to Ionized Impurity Scatterings . . . 82

15. RESULTS AND ANALYSIS . . . 86
    Series A . . . 87
    Series B and C . . . 101
    Experimental Results . . . 117

16. DISCUSSION . . . 124

17. CONCLUSIONS . . . 129

V CONCLUDING REMARKS . . . 132

18. SUMMARY . . . 132

APPENDICES

A. EMPIRICAL 30×30 $\vec{k} \cdot \vec{p}$ THEORY . . . 135
    Reduced Schrödinger Equation . . . 135
    Basis Functions . . . 136
    Matrix Elements . . . 137

B. GILAT-RAUBENHEIMER SCHEME . . . 141

C. GENERALIZED DEBYE THEORY . . . 144
    Basics . . . 144
    Applications of Generalized Debye Theory . . . 146
        Degenerate Electron Gas in 3D . . . 146
        Classical Electron Gas . . . 147

Singly Charged Donors 147

BIBLIOGRAPHY 148

BIOGRAPHICAL SKETCH 155

LIST OF TABLES

Table Page

1. Collection of Important Parameters of ZnS, ZnSe, and CdTe , , ... 9
2. $\vec{k} \cdot \vec{p}$ Results for ZnS Compared with Experimental Values 24
3. 30×30 $\vec{k} \cdot \vec{p}$ Method Input Parameters for ZnS, ZnSe, and CdTe. 25
4. QD Sizes with 200 meV Discrepancy between Calculated Absorption Edges by 30×30 $\vec{k} \cdot \vec{p}$ Model and Approximate Band Models. 39
5. $\vec{k} \cdot \vec{p}$ Results for CdTe Compared with Reported Values in Literature. 51
6. Results of CdTe QDs and Calibrated Absorption Edges by Potter 54
7. ZnSe Material Parameters Used in the Calculations of Part IV. 80
8. Input Parameters Used in the Calculations of Part IV. 87
9. Donor and Acceptor Concentrations in the Experiments 117
10. Empirical 30×30 $\vec{k} \cdot \vec{p}$ Theory Basis States 137
11. Linear Momentum Parameters for 30×30 $\vec{k} \cdot \vec{p}$ Theory 139
12. Antisymmetric Potential Parameters for 30×30 $\vec{k} \cdot \vec{p}$ Theory 139
13. Spin-orbital Coupling Parameters for 30×30 $\vec{k} \cdot \vec{p}$ Theory 140

LIST OF FIGURES

Figure Page

1. Unit cell of the FCC lattice of zincblende structure. 4

2. Connections of the Present Doctoral Research. 7

3. Schematic diagram of the thin-film MISIM structure and bandedge diagram of TFELD under high electric field. Indicated are the main processes: tunnel emission from interface states, impact excitation of activators, impact ionization of electron-hole pairs, and capture at arrival at the anode interface. . 10

4. Bandstructure of zincblende ZnS by the empirical 30×30 $\vec{k} \cdot \vec{p}$ method. . . . 26

5. Density of states for zincblende ZnS, calculated by GR scheme. 28

6. XPS spectrum (dark curve) and theoretical DOS calculation of ZnS 29

7. Convoluted theoretical DOS (dark curve) of ZnS with a Gaussian distribution of FWHM=1.25 eV 30

8. Dielectric constants and reflectivity for zincblende ZnS. Real part of the dielectric constant predominantly contributes to the reflectivity. 32

9. Theoretical reflectivity compared with experiment. The measurement covers up to 9.5 eV and the peak at 3.4 eV is due to Fabry-Perot effect. 34

10. Comparison of non-parabolic model with 30×30 $\vec{k} \cdot \vec{p}$ model for conduction band. Clearly, previous model is unsuitable to describe carrier energies even at 5% off Γ point. 40

11. Comparison of Luttinger model with 30×30 $\vec{k} \cdot \vec{p}$ model. As shown, Luttinger model is deficient in predicting carrier energies off Γ point. 41

12. Measured absorption edge of CdTe quantum dots compared with calculated absorption edge . The blue-shift effect, due to kinetic confinement, on the absorption edge is about 1.0 eV at 24 Å and slightly offset by the red-shift effect due to Coulomb interaction. 43

13. Bandstructure of zincblende CdTe computed by the empirical 30×30 $\vec{k} \cdot \vec{p}$ method. 50

14. Truncated Crystal Approximation (TCA) result of 30 Å CdTe quantum film. The TCA method maps the quantized cross sections of the electronic structure onto the unaffected plane. Shown are the first three subbands from each band in the bulk. Reflected clearly are the warping nature of the valence bands and the lift of the double degeneracy at the top of the valence bands. 56

15. Predicted bandedges at symmetrical points of CdTe quantum cube by the TCA method. No inverse square behaviors are found and asymptotic saturation of quantum confinement effect on the bandedges is predicted. . . . 57

16. Predicted transition energies of CdTe quantum cube by the TCA method. Γ point is the absorption edge above 16 Å and then replaced by an unidentified point in some general direction. 58

17. Experimental data compared with TCA predictions for CdTe quantum dots. The experimental data are corrected by considering size distribution and tunneling into finite glass barriers. Discrepancy at large L limit is because the TCA predictions are for QDs at zero temperature. 60

18. Comparison between numerical EFA and TCA results. Solid lines are EFA calculations with 4 mesh points in finite difference scheme. Inset shows 1D 2×2 $\vec{k} \cdot \vec{p}$ model, which is asymptotically parabolic for both bands. 62

19. Comparison between numerical EFA and TCA results. Solid lines are for EFA calculations with 20 mesh points. Compared to EFA results with 4 mesh points (Fig. 18) and TCA results, no agreements between EFA results with different mesh points and between EFA and TCA results have been achieved. 63

20. Analytical, numerical and TCA results of the White-Sham model. Straight solid lines are for viewing guide. The inset shows the bands as predicted by the White-Sham model. Excellent agreements have been achieved among all results. 65

21. Derivative of the ionized donor concentration with respect to the chemical potential for Series A. It indicates the screening capability of the ionized donors. At low temperature, compensation increases the capability as the filled states become partially occupied. Sharp transition occurs at 26.5 K. At high temperature, the β factor kicks in and reduces the capability. 90

22. Derivative of the free electron concentration with respect to the chemical potential for Series A. At low temperature, thermal excitation increases the screening capability of electrons for systems of low compensation. For highly compensated systems, due to MI transition, they show the behavior of degenerate electrons. The β factor affects the screening in all temperature range but dominates at high temperature. 91

23. Debye Length (in Å) versus temperature for Series A. At the *critical temperature* of 26.5 K, MI transition due to static screening occurs at low compensation. The transition temperature decreases with the acceptor concentration and vanishes above the *critical acceptor concentration* where the system becomes metallic. Below the critical temperature, screening effect is predominated by compensation. The β factor effect weakly increases the Debye length in non-transitional regime. 92

24. Binding energy of donors versus temperature for Series A. Below the *critical temperature*, donor level is reduced as acceptor concentration increases. Away from the transition region, it increases due to the β factor effect. 94

25. Ionized donor concentration versus temperature for Series A. At low compensation, thermal ionization of donors increases the ionized population exponentially. Increase in acceptor concentration accordingly creates the same amount of ionized donors at low temperature. Above the critical acceptor concentration, ionized donor concentration increases weakly with temperature. There is slight change in the ionized donor concentration above the *critical temperature*. 95

26. Chemical potential as a function of temperature for Series A. MI transition occurs at a critical acceptor concentration of $5 \times 10^{15} cm^{-3}$ for compensated systems or at a critical temperature of 26.5 K for uncompensated systems. Below the critical temperature and the critical acceptor concentration, chemical potential is frozen around -13 meV. At high temperature, the chemical potential decreases towards the middle of the bandgap. 97

27. Free electron concentration as a function of temperature and acceptor concentration for Series A. The concentration tends to saturation above the critical temperature and critical acceptor concentration. Freeze-out occurs at low acceptor concentration, but the slope varies with acceptor concentration. . 99

28. Dependence of Hall mobility on temperature and acceptor concentration for Series A. The mobility decreases drastically with temperature in correlation with the ionized impurity concentration below the critical temperature and the critical acceptor concentration and changes weakly in other regions. 100

29. Ionized donor concentration versus temperature for Series B and C. The two series differ around and below the critical temperature. At high temperature, the ionized population tends to saturate for the two series. Thermal ionization dominates at low temperature in Series B and compensation dominates in Series C. Metallic systems saturates at all temperature. 103

30. Debye length versus temperature for Series B and C. The length decreases with donor concentration for both series. For Series C, the Debye length increases with temperature. For Series B, it decreases below the critical temperature and increases above the temperature. 104

31. Debye length versus electron density for Series B and C. Series B follows power law dependence on density with a power of $-.42$ while Series C shows diverse dependence from weak at low donor concentration to power law dependence with a power of .33 at high concentration. 106

32. Donor level versus temperature for Series B and C. Donor level is reduced by screening effect. In both series, donor level decreases with donor concentration. In Series B, donor level is drastically shrinked below 26.5 K and becomes zero above $10^{17} cm^{-3}$ of donor concentration. It increases above the transition region. For Series C, donor level reduces with temperature. . 107

33. Chemical potential versus temperature for Series B and C. Series B shows MI transition above $10^{17} cm^{-3}$ of donor concentration and the critical temperature reduces with donor concentration. Series C features gradual increase of chemical potential and MI transition occurs above $10^{17} cm^{-3}$ of donor concentration. 109

34. Electron concentration versus temperature for Series B and C. Generally, electron density in Series C is an order of magnitude lower than in Series B except for metallic systems below the critical temperature. Non-metallic systems show freeze-out and saturation regimes as normal, while temperature dependence differs in the freeze-out regime between the two series. Series C begins deviating from normal at a donor concentration of $10^{16} cm^{-3}$. Electron density increases after MI transition for both series. 111

35. Hall mobility versus temperature for Series B and C. In Series C, mobility decreases with temperature above donor concentration of $10^{16} cm^{-3}$ and increases below that concentration. In Series B, mobility reduces with temperature faster than in Series C and MI transition slows the reduction. . 113

36. Hall mobility versus electron density for Series B and C. At high density, two series follow nearly the same power law with a power of about -1.6 for Series C. At low density, Series B follows power law with a power of $-.89$ while Series C changes insensitively with electron density. 115

37. Ratio of Hall mobility to drift mobility versus temperature for Series B and C. In Series B, the ratio converges to 1.89 at low temperature and in Series C the ratio is approximately unity at high donor concentration. 116

38. Measured chemical potential for n-ZnSe 120

39. Measured free-electron density for n-ZnSe 121

40. Measured Hall mobility versus temperature for n-ZnSe 122

41. Debye length versus temperature for Series A with linear functional form for donor level. 123

42. Brillouin Zone of face-center-cubic (FCC) and zincblende lattices. 143

Abstract of Dissertation Presented to the Graduate School
of the University of Florida in Partial Fulfillment of the
Requirements for the Degree of Doctor of Philosophy.

ELECTRONIC, OPTICAL, AND TRANSPORT PROPERTIES OF WIDEGAP II-VI SEMICONDUCTORS

By

Jianzhong Li

December, 1997

Chairman: Dr. Christopher Jay Stanton
Major Department: Physics

Different properties of three zincblende IIB-VIA compound semiconductors, of importance to the optoelectronic industry, are investigated. Firstly, the electronic structures of ZnS and CdTe are obtained by the empirical 30×30 $\vec{k} \cdot \vec{p}$ method, which is fitted to well-established experimental data and agrees with other calculations. Then the derived bandstructure of ZnS is employed in satisfactory modelling of the X-ray photoemission spectroscopy spectrum and reflectivity data by Dr. P. H. Holloway at UF. The density of states, computed numerically by the Gilat-Raubenheimer scheme, of the material clearly indicates two salient features for an excellent blue/green electroluminescent phosphor candidate: a large bandgap (*3.7 eV*) and concentrated density of states for superhot electrons (at *3 eV*). In parallel, the bandstructure of CdTe is used in modelling of the quantum confinement effect measurements on the absorption edge energy of semiconducting crystallites embedded in a transparent glass matrix, done by Dr. J. H. Simmons at UF. The truncated crystal approximation is applied, with an equivalent volume scheme, to the quantum dots and excellent agreement is achieved between theory and experiment. In addition, a self-consistent theory including static screening effect is proposed to explain behaviors of chemical potential, free-carrier concentration, and low-temperature Hall mobility due to ionized impurity scatterings in intermediately to heavily doped *n*-ZnSe, as used in injection-type devices to realize ohmic contacts. The theoretical results are qualitatively comparable to the experimental data by Drs. J. H. Simmons and R. M. Park at UF. In particular, the theory predicts that compensation reduces carrier concentration and increases screening capability of semiconductors.

PART I
INTRODUCTION

CHAPTER 1
OVERVIEW

Modern society is more and more revolutionized by technological breakthroughs. Replacement of massive manual labor by machinery has been completed in the developed countries. Great progress in communication, transportation, energy consumption, health-related industry, and so on, move the world towards a more environment-friendly, long-lifespan biosphere. And materials research and development (R&D) has tremendously facilitated this advancement. For instance, steel made the first industrial revolution into a reality; copper wire enables the long distance transportation of electricity; aluminium allows airplanes to take to the sky; plastics are widely used in packaging; and ceramics are versatile in insulation. But the semiconductor presents the best example.

Semiconductors have been making resounding impacts upon the way of life of mankind since Bardeen and Brattain [1, 2] discovered the point-contact transistor, and Shockley, Sparks, and Teal [3] first observed the junction transistor action. This realization of the solid-state version of the vacuum-tube triode began the era of circuit integration and a computing revolution. The rapid progress in compound-semiconductor technology introduces a new class of ultrafast devices—heterostructure devices. Without them for information processing, high-speed computing would not be possible. However, it would be ignorant without mentioning that optoelectronic devices, which are essential in solid state lasers, telecommunication and display technologies. They are transforming the field of telecommunications. Nowadays, semiconductors research is indispensable in the success and development of the microelectronic and the optoelectronic industries.

A semiconductor is a solid with an electric conductivity between that of a metal and an insulator [4]. Discussion in this overview is restricted to the sub-group of IV, III-V, and II-VI crystalline compound semiconductors. Because of the nature of the predominantly covalent bonding, group IV elements crystallize in diamond lattice (space group O_h^7); most III-V compounds, *e.g.*, GaAs, crystallize in zincblende lattice (space group T_d^2; see Fig. 1); many of the II-VI compounds crystallize in both the zincblende and the wurtzite lattices (space group C_{6v}^4) [5], as ionicity of the bonding increases. Their electric conducting ability ranges from a semi-metal (*e.g.*, α-Sn and HgTe) to a widegap semiconductor (*e.g.*, CdS and GaN), which means a small conduction-valence band overlap to a bandgap as large as $6.2eV$ for AlN. The electronic and phonon structures of these crystalline semiconductors are predominantly determined by the nature of their chemical bonding [6], which, in turn, determines the prospects of a potential candidate of technical and scientific interest.

The unique ability for semiconductors to be modified extensively by external means is the very reason why they are so versatilely employed in transistors, switching devices, voltage regulators, photocells, photodetectors, and so on. Doping is the original, and still is, the most effective way to modify the conducting properties of a semiconductor [7]. In order to achieve this, shallow impurity states are desired so that, under thermal excitation, free carriers can be generated into the conduction (electron conduction) and/or valence band (hole conduction). Bipolar and *p-n* junctions are made, by means of doping, for circuit switching, signal amplification, and current rectifying. Even though doping supplies a semiconductor with carriers, it restricts its mobility by presenting scattering centers in the system. Modulation doping greatly reduces this restriction by separating

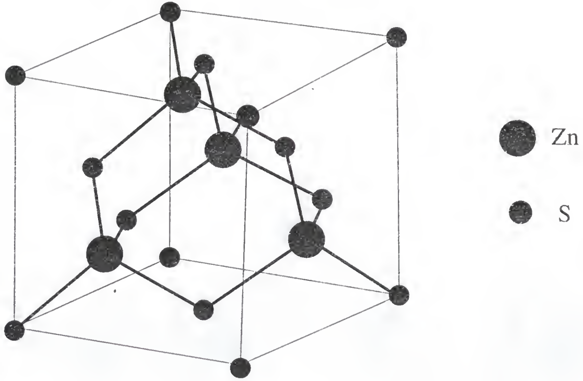

Figure 1: Unit cell of the FCC lattice of zincblende structure.

the carriers and impurities in different regions. Over-doping a bulk semiconductor can convert it into a metal, and this process is often called metallization. On the other hand, the luminescent properties of a semiconductor can be modified by doping the material with deep-level impurities, since the quantum efficiency of photon generation intricately depends upon the interplay of radiative and non-radiative channels.

By physically and/or chemically controlling the interfacial abruptness, one can make semiconductor heterostructures. This introduces a whole new world of opportunities for new concepts for devices and physics [8-11]. Various quantum devices are made into reality with progress in growth technologies. Quantum wells, wires, dots, and superlattices allow improved electronic properties from the bulk system, enhanced oscillator strengths, and density of states. Wave-packet dynamics in quantum confined systems can be used to implement Bloch oscillation, and to generate Tera-Hertz electromagnetic waves. Just as carriers (electrons and holes) are restricted in real space, confinement may also occur for phonons and photons. In heterostructures, there are many physical parameters which can be manipulated for the advantage of devices. Bandgap engineering [12], which means targeted alteration of bandstructure, can be done by alloying in the barrier and/or active region, introducing strain effect due to lattice mismatch, or creating internal electric field due to charge transfer. Nanostructured systems[1] [13] condense many developments in the area of heterostructures and play an irreplaceable role in integrated electro-machinery, electronics and optoelectronics. Heterostructures make high-mobility, high-efficiency, low-threshold, low-dimension possible in semiconductors.

External fields can manipulate the response of semiconductors so as to achieve what is impossible at equilibrium. High electric fields can modify the electronic structures and dynamics of semiconductors. Two dimensional electron gas exhibits novel physical phenomena, such as mesoscopic transport, quantum Hall effect, and enhanced many-body effects [14]. Also, under high electric field, hot electrons are generated, due to acceleration by the field and bottlenecks in the relaxation. Some systems show the Gunn effect [15] in bulk semiconductors and avalanche processes in reversed *p-n* junctions [16]. Thin-film electric-field-related displays [17] are under active pursuit in the phosphor community for high electric field inside a semiconductor thin film efficiently yields visible light, under certain circumstances. Magnetic field tends to localize and polarize electronic states with Landau levels formed in a semiconductor, which manifests interesting magneto-optical effects [18] and quantum Hall effects [19, 20]. Nowadays, powerful lasers are not only useful in spectroscopy [21] but also capable of driving a semiconductor far from equilibrium. Femtosecond spectroscopy provides information on the dynamical behavior of carriers. New physical systems, such as excitonic plasma, are artificially created to test theoretical predictions, such as Bose-Einstein condensation [22]. Though some important methods of manipulation, such as current injection and sound waves, are neglected in the present discussion, it is quite amazing that in so many ways external sources can be employed to detect, modulate, and manipulate a semiconductor system.

---

[1] Low-dimensional structures that exhibit manifest quantum effects.

Above is an incomplete general summary of semiconductor physics and technology. Reliability and magnetic-effects-related topics are not covered. In the next chapter, the author will focus on three II-VI semiconductors, ZnS, ZnSe and CdTe. The following diagram illustrates the logical connections of this research.

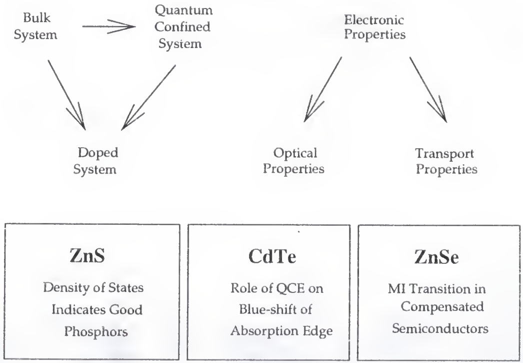
Bulk System
Quantum Confined System
Doped System
Electronic Properties
Optical Properties
Transport Properties
ZnS
Density of States Indicates Good Phosphors
CdTe
Role of QCE on Blue-shift of Absorption Edge
ZnSe
MI Transition in Compensated Semiconductors

Figure 2: Connections of the Present Doctoral Research.

CHAPTER 2
IIB-VIA COMPOUND SEMICONDUCTORS

The present thesis deals exclusively with zincblende, widegap chalcogenide semiconductors. All of the three materials that are considered possess a direct bandgap, which is instrumental in optical and optoelectronic applications. Narrow-bandgap chalcogenide semiconductors are extensively investigated for their involvement in infrared photoemission, detection and optical modulation [23]. The need for high-speed, wide-bandwidth transmission of information pushes for R&D into the widegap semiconductors [24], both III-V compounds and IIB-VIA compounds which are composed of Zn, Cd, Hg (group IIB) and S, Se, Te (group VIA). In accord with the progress in processing technology for these compounds, the study of IIB-VIA chalcogenides inevitably benefits and consequently Hg/CdTe detectors [25], ZnSe-based blue/green LEDs [26], and other optoelectronic applications [27] are available commercially today.

ZnS

As one of the most important phosphors [30] and ultraviolet (UV) coating materials [31], great efforts in academia and industry have been dedicated to ZnS. Theoretically, the electronic, transport, and optical properties of ZnS have been investigated thoroughly (for a complete list of references, see the bibliography in Cohen and Chelikowsky [32]). Nevertheless, there are rejuvenating activities in ZnS, due to interest in the alternating-current thin-film electroluminescent display (AC TFELD) research [33-36] and the coming of a heterostructure age.

Table 1: Collection of Important Parameters of ZnS, ZnSe, and CdTe [4, 28, 29].

Parameter	ZnS	ZnSe	CdTe
Lattice constant, a (Å)	5.4093	5.6687	6.481
Energy gap at 0 K, E_g (eV)	3.84	2.94	1.59
$\frac{dE_g}{dT}$ (10^{-4} eV/K)	-4.6	-8	-3
$\frac{dE_g}{dP}$ (10^{-6} eV/bar), (at R.T.)	5.7	0.7	8.0
Spin-orbit splitting, Δ_0 (eV)	0.072	0.403	0.811
Electron effective mass, m_e^* (m_e)	0.27	0.17	0.11
Heavy hole effective mass, m_{hh}^*	0.58	0.60	0.40
Light hole effective mass, m_{lh}^*	0.230	0.149	0.13
Valence band parameters:			
γ_1	6.12	4.3	5.3
γ_2	0.53	1.14	1.7
γ_3	1.00	1.84	2.0
High frequency dielectric constant, ε_∞	5.7	6.2	7.2
Low frequency dielectric constant, ε_0	8.9	9.6	10.4

Electroluminescence (EL) is a cold light-emitting phenomenon when a high electric field is applied onto a non-metallic material. With the advent of VLSI technology, TFELD becomes a viable alternative, among flat panel displays (FPD), to the existing bulky, high-voltage cathode-ray tube (CRT) technology. There presents a challenge, however, to the R&D in phosphorescent semiconductors, which is how to improve their performance and reduce their price. In technical respect, understanding basic physical processes, such as carrier dynamics, radiative relaxations that control the EL phenomenon and then optimizing TFEL devices are the major concerns of display R&D.

To understand EL in a Metal-Insulator-Semiconductor-Insulator-Metal (MISIM)

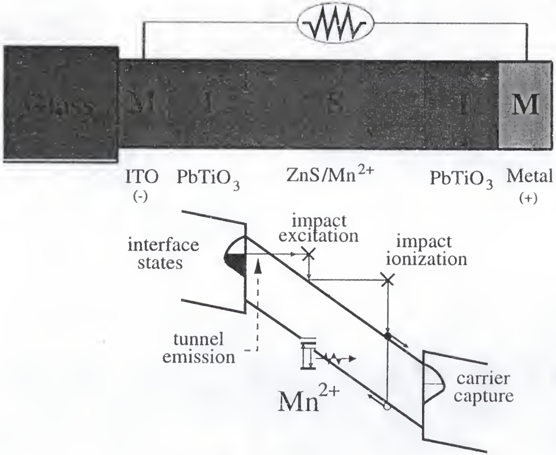

Figure 3: Schematic diagram of the thin-film MISIM structure and bandedge diagram of TFELD under high electric field. Indicated are the main processes: tunnel emission from interface states, impact excitation of activators, impact ionization of electron-hole pairs, and capture at arrival at the anode interface.

structure (see Fig. 3), free carrier dynamics has to be investigated for it determines the quantum efficiency of photon generation by impact excitation of the luminescent impurities (activators). For dilute free carrier systems that lack long range interactions, a kinetic description of the carrier distribution functions has been found to be overwhelmingly successful [37-42]. However, Boltzmann kinetic equation (BKE)[1] is notoriously difficult to solve analytically. Nowadays, solutions of BKE require numerical computations and Monte Carlo simulations [43-45]. These require immense computing time and restrict their applications to large-scale dynamics modeling. Full Brillouin zone electronic structures that are required in sophisticated computations increase the demand for computing power considerably.

Inhomogeneity in the MISIM EL system introduces spatial degrees of freedom into BKE and demands self-consistent treatment with respect to the non-uniform local electric field. To meet this numerical challenge, numerical integration scheme, *i.e.*, adaptive stepsize Runge-Kutta method [46, 47], may be adopted to solve BKE with the electronic structure of the system, derived from the fast empirical 30×30 $\vec{k} \cdot \vec{p}$ method (see Appendix A), included. Part II of the present thesis covers preparatory research for this future project. Bandstructure calculations for ZnS are implemented and employed for modeling the X-ray photoemission spectroscopy spectrum and optical reflectivity measurement. Simultaneously, the calculated bandstructure is compared to well-established experimental and theoretical results for accuracy check. The results are in excellent agreement with the well-established data and fit the measurements satisfactorily.

---

[1] also known as Boltzmann transport equation (BTE).

ZnSe

Due to its similarity to ZnS, research in ZnSe has always been done in conjunction with the research in ZnS [28]. The major differences between these two materials are twofold: (1) ZnS has an energy gap of *3.84 eV* and ZnSe possesses one of *2.94 eV*; (2) spin-orbital coupling in ZnSe is much more important than in ZnS, thanks to the large atomic weight of selenium. However, their technological importance is more related to the availability of high quality materials that industry can produce. In applications concerning phosphors, the materials are in polycrystalline structures while modern developments are more and more inclined towards single crystalline structures. In this aspect, ZnSe is chosen more than ZnS in quantum structure R&D. It is not within the scope of this dissertation to provide a review of bulk ZnSe. For a list of references on the physical properties of bulk ZnSe, see the bibliography in Cohen and Chelikowsky [32].

The current research interests in ZnSe concentrate upon the area of blue/green LEDs and lasers [26]. These quantum-well devices with ZnSe, as the confined and active region, sandwiched between barrier layers, provide light as a result of carrier injection through the electrodes and radiative recombination in the confined region. One of the technical challenges, once severely impeding R&D in these devices, is low-resistivity *p*-type shallow-impurity doping in ZnSe, which is required for making ohmic contacts in injection-type LEDs and lasers. It was solved by the ingenious method of Park *et al.* [48]. Even though available on the market today, there are still plenty of interesting physics to be done in these quantum-structured devices. Among them is the study of the physical properties of intermediately to heavily doped bulk systems. Optical properties of these systems affect the performance of the doped semiconductors as the transparent window for light output. Transport properties are the major issue in the making of ohmic contacts and quantum efficiency of these injection-type devices.

Part IV of the present thesis treats the *n*-type shallow-impurity doping problem in ZnSe. The major difference in treating *p*-type doping is that the transport is *hole*-type and degeneracy in the bands complicates the problem. The *n*-type doping problem has been treated by Harry Ruda [49]. A shortcoming of his analysis is it does not consider the change in the chemical potential when the system undergoes intermediate to heavy doping. In reality, there are different kinds of extrinsic impurities, in addition to native point defects and their complexes in the *n*-type doped ZnSe. The present research considers the most simplified case, which is a system with only independent hydrogen-like dopants and acceptors under the assumption of complete compensation, but takes into account self-consistent static screening for impurity ionization. The model allows the chemical potential to change with doping and thus modify the carrier concentration as well as the mobility correspondingly. Qualitative agreements for chemical potential, carrier concentration are found between the related experiment and the present research, but lack of low temperature measurements on the mobility impedes comparison in this aspect.

CdTe

Crystalline cadmium telluride [50] has been employed in nuclear radiation detection, electro-optic modulation, and as an infrared optical material. Alloys of $Cd_xHg_{1-x}Te$ have become important as infrared detectors, and CdTe is a key substrate for the fabrication of devices based on $Cd_xHg_{1-x}Te$ alloys and superlattices. Potential applications in EL and microwave devices, high power laser windows, *etc.*, have stimulated considerable interests of basic research in CdTe. Optical and photoemission studies were undertaken in aid of the construction of CdTe bandstructure (see reference 50, page 84). The electronic structure of CdTe was studied by applications of the dielectric bonding theory of Philips and Van Vechten [6] and various other more detailed approaches (see reference 50, page 81), which provide good interpretations to experimental data. Transport properties of CdTe provide further information such as the effective masses of charged carriers, interactions of charged carriers and phonons with impurities and elementary excitations in the material. Moreover, defects in CdTe are extensively investigated because their structures influence performances of CdTe in devices. For the latest experimental and theoretical data, Landolt-Börnstein New Series [29], pages 225–230, may be consulted.

Semiconductor microstructures and nanostructures are important in integrated systems and broaden the possibilities of improving optoelectronic properties of semiconductors by exhibiting behavioral transitions from bulk materials to molecules. These *quantum size effects* in CdTe micro- and nanostructures have been explored extensively in the last twenty years [13, 28]. Quantum wells, wires, dots, and superlattices are configurations of those well-studied quantum structures. Among these structures, quantum dots (QDs) show carrier confinement effects in all three dimensions, which receive a great deal of attention for their significant optical nonlinearity. One way to make QDs is chemically embedding isolated semiconductor crystallites in a transparent glass matrix [51], and these systems are widely investigated. CdS and CdTe crystallites are the main focus of researches because of their utility in integrated optical systems. Systematic researches of the quantum confinement effects (QCEs) on various properties of nanostructures have been carried out to elucidate fundamental physics in these systems [42, 52-57], not necessarily only on CdTe.

Despite impressive efforts, there are issues in CdTe crystallites that remain. One of them is the QCEs on the absorption edge. The saturation of QCEs at extreme confinement seen by Potter *et al.* [58] was shown to disagree with current theoretical models. To better model QCEs in widegap QDs, it is essential to realize that although Coulomb interaction is important in modifying the oscillator strengths of optical transitions, bandstructure effect is predominant in affecting the optical transition states. Part III of the present thesis deals with the problem along this line with an approximate approach—the truncated crystal approximation, with the bulk bandstructure given by the empirical 30×30 $\vec{k} \cdot \vec{p}$ method. Excellent agreement is found between the experiment of Potter *et al.* and the present theoretical work.

As a note, CdTe is classified in this research as a widegap semiconductor, despite the fact that it has a bandgap of *1.59 eV*. This is simply because its bandstructure (Fig. 13) greatly resembles those of the other widegap semiconductors, such as ZnS (Fig. 4). As far as the study of its optical properties is concerned, no differences are discerned compared with the other widegap systems in reality.

PART II
OPTICAL PROPERTIES AND XPS SPECTRUM OF ZnS

CHAPTER 3
INTRODUCTION

Zinc sulfide has been one of the most important phosphors, used as visual displays in scientific instruments, entertainment, and radars. It is also an indispensable coating material in applications of ultraviolet optics. Though tremendous progress has been made in the field of information exchange since the invention of optical fiber, high demand on speed and bandwidth in communications has always been in place. Faster, higher frequency and more efficient optoelectronic materials are under active pursuit. In addition, nonlinear optical properties are of great interest in telecommunications, which is instrumental in signal amplification and modulation.

Despite the fact that it has been known for decades as a phosphorescent material, ZnS has not finished showing improvements in efficiency, spectrum, and refreshing rate. For the last three decades, great interest has been shown in development of the material as a promising active blue/green phosphor [28]. Zincblende ZnS is a direct bandgap semiconductor with a bandgap of $3.7\ eV$ at room temperature. This absorption-free window for visible light and excellent properties as a phosphor make ZnS one of the top candidates for R&D in solid state blue/green light emitting diodes (LEDs) and lasers. Study of optical properties, both linear and nonlinear, aids understandings towards development and optimization of microelectronic and optoelectronic devices.

In the present part of this research, numerical computation of the linear optical properties from microscopic theory is needed for checking bandstructure, matrix elements calculation, and Gilat-Raubenheimer (GR) scheme code. In this calculation, (1) the empirical 30×30 $\vec{k} \cdot \vec{p}$ full zone bandstructure calculation (see Appendix A) for zincblende ZnS (see Fig. 4 on page 26) has been implemented; (2) density of states (DOS) (see Fig. 5 on page 28), joint density of states (JDOS), and dielectric functions (see Fig. 8 on page 32) are computed, (3) valence band DOS of ZnS data was compared with XPS experiments [59] by Dr. Holloway of Materials Science and Engineering at UF; (4) calculated dielectric functions are examined against both well-established theoretical and experimental data for ZnS; (5) reflectivity and absorption, contributed by linear interband transitions, are computed and compared to experimental data by Dr. Holloway, which show good agreement (see Fig. 9 on page 34).

CHAPTER 4
THEORIES

X-ray Photoemission Spectroscopy (XPS) [60]

Photoelectron spectroscopies are among the most powerful experimental tools for probing the electronic structure of solids. Photoemission spectra can extract information on the absolute position of an energy band. It is even possible to determine directly the electronic structure. Also photoemission is sensitive to surface conditions, either intrinsic or extrinsic in nature. Careful tuning of the incident radiation enables emphasizing either bulk or surface spectral features. Two major technical developments have aided photoemission measurements immensely: ultrahigh vacuum and synchrotron radiation. Photoemission techniques can be classified according to how the energy and momentum of the incident photon and ejected photoelectron are controlled.

The three-step model is a most often used physical model of photoemission. The first step is a photon absorption by a bulk excitation. Then the excited electron propagates to the surface, and the third step is its escape through the crystalline surface. Owing to the bulk nature of the first step, the initial and the final wavevectors are identical so that a direct transition occurs. The probability for an excitation to occur between two bands is dictated by dipole interactions, and energy is conserved in the process. The number of photoelectrons ejected with a specific energy for a given incident photon energy can be formulated as

$$\begin{aligned} n(E_{kin},\hbar\omega) = c_1 \times \sum_{\vec{k},i,f} P_{if}\left(\vec{k}\right)\delta\left(E_f\left(\vec{k}\right) - E_i\left(\vec{k}\right) - \hbar\omega\right) \\ \times\delta\left(E_f\left(\vec{k}\right) - E_{kin} + E_v\right) \end{aligned} \tag{1}$$

where $\hbar\omega$ is the photon energy, E_{kin} is the kinetic energy of the photoelectron, E_v is the vacuum level, $E_i\left(\vec{k}\right)$ is the energy of the initial state, and $E_f\left(\vec{k}\right)$ is the energy of the final state. $P_{if}\left(\vec{k}\right)$ is the dipole matrix element between initial state and final state. The first δ function in Eq. (1) comes from energy conservation in the first step; and the second δ function imposes energy conservation in the third step.

Under certain assumptions, Eq. (1) reduces to an extremely useful form. For instance, consider the assumptions of (1) constant matrix elements independent of $\vec{k}$ and of (2) flat valence (or conduction) bands or non-conservation of $\vec{k}$. The former assumption is usually valid though the latter assumption is usually not. Under these additional approximations, it is possible to obtain [32]

$$\begin{aligned} n(E_{kin}, \hbar\omega) = c_2 \times N_i(E_{kin} - E_v - \hbar\omega) \\ \times N_f(E_{kin} - E_v) \end{aligned} \tag{2}$$

where c_2 is a constant, N_i is the DOS for the initial states, and N_f is the DOS for the final states.

For XPS, the mode of operation is to measure, as a function of energy, the number of emitted photoelectrons by fixing the incident photon energy. At high photon energies, photoemission spectra are fairly easy to interpret. From an operational point of view, they appear to replicate the valence band DOS. In a more formal sense, if the photon wavevector is not insignificant compared to a reciprocal lattice vector, which may be the case at large photon energies, then $\vec{k}$-conservation still holds, but the transitions involved are not direct. Therefore, it effectively averages over the final states in Eq. (1). Moreover, at large photon energies, the final states tend to be plane-wave-like and most likely do not contribute to a structural spectrum. In this sense, Eq. (2) becomes valid. Furthermore, the final DOS may be omitted from consideration:

$$n(E_{kin}, \hbar\omega) = c \times N_i(E_{kin} - E_v - \hbar\omega)\,. \tag{3}$$

Therefore, *By a judicious choice of* $\hbar\omega$ *and via an analysis of* N_i, *a direct replica of the valence band density of states is almost obtained* [32].

XPS measures energy distribution curves (EDCs) and many features of EDCs are well understood. When $\hbar\omega \lesssim 15eV$, EDCs are highly structured, which arises from JDOS effects. Other "understood" features include matrix element effects and penetration depth changes. The matrix element effects are characteristic of the electronic structure of a semiconductor. Above the fundamental energy gap, dipole transitions occur between upper valence bands and lower conduction bands. The initial and final states near the band gap are usually well defined in terms of orbital character, so spectral features could be enhanced or suppressed depending upon the magnitude of the dipole matrix element between valence and conduction states. At higher energies, sum rules for the dipole matrix elements demand that the magnitude of the matrix element between initial and final states decrease. As a consequence, with higher energy photons, the spectral features begin to resemble a simple JDOS. The critical point behaviors in the spectral features are discussed thoroughly by Cohen and Chelikowsky [32] and Bassani and Parravicini [61].

Linear Optical Properties—Interband Transition Theory [61]

The optical behavior of a material is completely determined if its optical constants are known. The index of refraction, *n*, and the extinction coefficient, *k*, may thus be regarded as a summary of the experimental results of optical measurements made on the material. In general, they are related to the dielectric constants by

$$\begin{aligned} N^2 &= \varepsilon_1 + \imath\varepsilon_2 \,; \\ N &= n + ik \,, \end{aligned} \tag{4}$$

where N is the complex index of refraction, ε_1 and ε_2 are the real and imaginary parts of the complex dielectric constant ϵ. The normal-incidence reflectivity R is given by

$$R = \left| \frac{N-1}{N+1} \right|^2 = \frac{(n-1)^2 + k^2}{(n+1)^2 + k^2} \,. \tag{5}$$

In this part of the thesis, the complex dielectric constant ϵ is computed microscopically as a function of the energy of incident photon $\hbar\omega$ by random-phase approximation (RPA) as follows

$$\begin{aligned} \varepsilon\left(\vec{0},\omega\right) &= 1 + 4\pi\chi\left(\vec{0},\omega\right) \\ Im[\chi\left(\vec{0},\omega\right)] &= \frac{\pi}{\mathcal{N}} \sum_{cv} \int_{BZ} d\vec{k}\, F(\vec{k})\; \delta[\omega - \omega_{c,v}\left(\vec{k}\right)] \\ Re[\chi\left(\vec{0},\omega\right)] &= \frac{1}{\mathcal{N}} \sum_{cv} \int_{BZ} d\vec{k}\, \frac{F(\vec{k})}{\omega - \omega_{c,v}\left(\vec{k}\right)} \\ F(\vec{k}) &= \frac{2}{(2\pi)^3} |\langle c\vec{k}|\vec{e}\cdot \widehat{P}|v\vec{k}\rangle|^2 \ . \end{aligned} \tag{6}$$

where χ is the linear response function of the system to the transverse electric field of the incident photon with polarization $\vec{e}$, $\omega_{c,v}\left(\vec{k}\right)$ is the transition frequency between conduction and valence bands, and $\mathcal{N} = \left(\frac{m\omega}{e}\right)^2$. The bands are computed by the empirical 30×30 $\vec{k}\cdot\vec{p}$ method (see Appendix A and references within), and the integration over the full Brillouin zone (BZ) is implemented via the Gilat-Raubenheimer scheme as outlined in Appendix B (see references within).

Experimentally, the optical properties of solids may be determined by Kramers-Krönig analysis of normal-incidence reflectivity data or indirectly by ellipsometric measurements with polarized light. It is convenient to distinguish three spectral regions in the description of the optical properties of widegap semiconductor compounds. The first region, extending to about *8* to *10 eV*, is characterized by a sharp structure associated with valence- to conduction-band transitions. The second region, which extends to about *16 eV*, is marked by a rapid decrease of the reflectivity that is reminiscent of the behavior of certain metals in the ultraviolet. Sharp maxima in the function $-Im\,(\varepsilon^{-1})$, which describes the energy loss of fast electrons traversing the material, have been frequently associated with the existence of plasma oscillation in this region. A maximum of this type is seen in this "metallic" region. In the third region, the reflectivity again rises, indicating the onset of other optical absorption processes. This structure is associated with transitions between filled d bands lying below the filled valence bands and empty conduction bands.

CHAPTER 5
RESULTS AND DISCUSSION

The electronic structure of zincblende ZnS is obtained by application of the empirical 30×30 $\vec{k} \cdot \vec{p}$ method and the result is shown in Fig. 4. Parameters used in the method are adjusted to give the best overall fit to the known experimental data [29]. Tables 3 and 2 list the $\vec{k} \cdot \vec{p}$ input parameters and comparison of the theoretical result to well-established experimental data. Refer to Appendix A for an explanation of the meaning of all symbols. V_6^- and $E\left(\Gamma^l_{25'}\right)$ are set to zero, so the top of the valence band is taken as a reference point for the band energies.

Table 2: $\vec{k} \cdot \vec{p}$ Results for ZnS Compared with Experimental Values [29].

	E_g	$\Gamma^v_{15} - \Gamma^c_{15}$	Δ_0	$\Lambda_3 - \Lambda_1$	$L^v_3 - L^c_3$	$X^v_5 - X^c_5$
expt.	3.85	8.35	0.072	5.7	9.8	6.6
theory	3.84	8.76	0.069	5.95	9.4	6.88

The DOS of the zincblende ZnS is computed as well. The DOS is given by

$$N(E) = V \sum_n \int_{BZ} \frac{d^3k}{(2\pi)^3} \delta\Big(E - \epsilon_n\big(\vec{k}\big)\Big) \tag{7}$$

where n is the band index which takes into account of the spin degree of freedom as well. GR scheme is used when calculating the integral over the BZ. Then the above expression is reduced to

$$N(E) \approx 48 \times \frac{V}{(2\pi)^3} \sum_n \sum_{itetr=1}^{3} \sum_i \int_i d^3k \, \delta\Big(E - \epsilon_n\big(\vec{k}\big)\Big) \tag{8}$$

Table 3: 30×30 $\vec{k} \cdot \vec{p}$ Method Input Parameters for ZnS, ZnSe, and CdTe.

Parameter	ZnS	ZnSe	CdTe
$E(\Gamma_1^l)$	-0.842	-0.905	-0.728
$E(\Gamma_1^u)$	0.943	0.521	0.6263
$E(\Gamma_{2'}^l)$	0.032	0.0467	0.078
$E(\Gamma_{2'}^u)$	1.161	1.028	0.693
$E(\Gamma_{12'})$	0.755	0.578	0.6093
$E(\Gamma_{15})$	0.433	0.338	0.416
$E(\Gamma_{25'}^u)$	1.1	0.883	0.8764
P	1.371	1.056	1.072
Q	1.16	1.244	1.035
R	0.847	0.692	0.769
P''	-0.014	0.109	0.157
P'	0.093	0.232	0.236
Q'	-0.691	-0.508	-0.526
R'	1.23	1.355	0.947
P'''	1.31	1.496	1.021
T	1.379	1.324	1.034
T'	-0.361	-0.255	-0.348
Δ_{25}'	0.006	0.0179	0.0542
Δ_{15}	0.0013	0.0245	0.0409
Δ^-	0.0	-0.0141	-0.0351
V_1^-	0.269	0.3024	0.1002
V_2^-	-0.594	-0.364	-0.1503
V_3^-	0.76	0.474	0.260
V_4^-	0.19	0.3915	0.12
V_5^-	-0.196	-0.3043	-0.0303

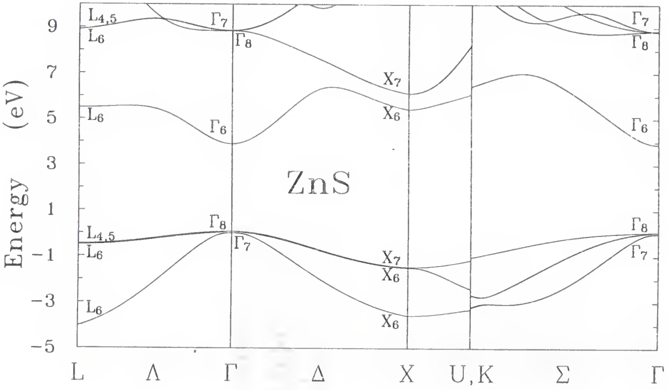

Figure 4: Bandstructure of zincblende ZnS by the empirical 30 × 30 $\vec{k} \cdot \vec{p}$ method.

where the notation follows Appendix B and the integral is carried out inside the *i*-th smaller tetrahedron. Figure 5 is computed using 12^3 smaller tetrahedra within each of these three main tetrahedra, ΓLKW, ΓLWU, and ΓUWX. The computation on a DEC alpha 3000/700 machine takes about *6* minutes. Actually the number of smaller tetrahedra above may be reduced to 6^3 without too much sacrifice of numerical accuracy. The total DOS for each band is obtained to check whether it agrees with unity, the expected number of electrons *per* unit cell that each band can take.

Shown in Fig. 6 is the XPS valence band data after removal of the background and shifting *1.1 eV* accordingly to fit the theoretical data. Two subpeaks (I_1 and I_2) are resolved within Peak I and one shoulder (S_1) is distinguished in the spectrum. In order to account for the instrumental broadening, the theoretical DOS data is convoluted with a Gaussian distribution with a full width at half maximum (FWHM) of *1.25 eV*, which is the FWHM of the Zn 3d core level in the XPS spectrum. The result is shown in Fig. 7. It is easy to see that: (1) the relative intensities of Peaks I and II fit better with the XPS data; (2) the tail at the high energy side of the convoluted curve extends to about *1 eV* above the original top of the valence band. Therefore, the theoretical DOS consistently explains the XPS spectrum.

The real and imaginary dielectric constants are calculated based upon the bandstructure derived by the empirical 30×30 $\vec{k} \cdot \vec{p}$ method before other optical properties can be obtained. The calculation is carried out with GR scheme and an approximation of constant optical transition probability within each smaller tetrahedron is used. To ascertain the accuracy of the calculated dielectric constants, comparison of the present theoretical calculation with well-established experimental data (see, for example, Landolt-Börnstein New

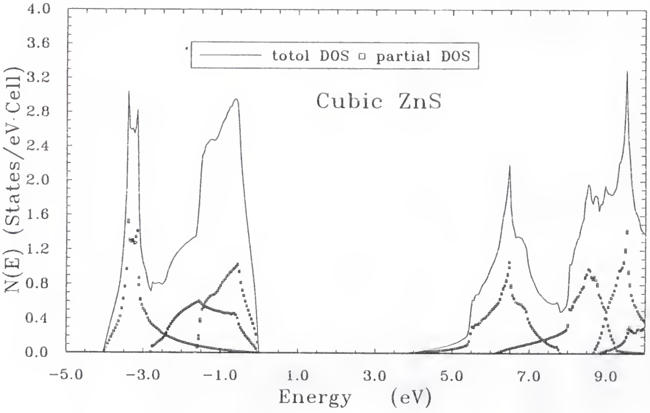

Figure 5: Density of states for zincblende ZnS, calculated by GR scheme.

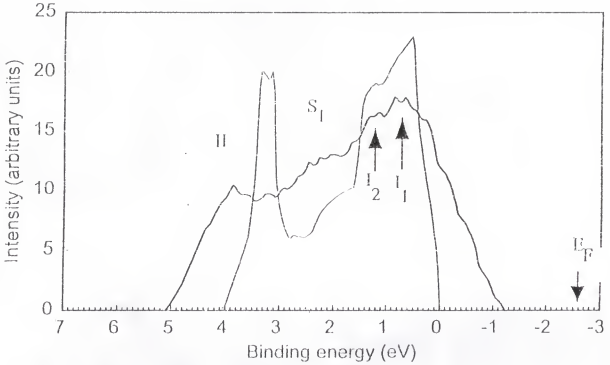

Figure 6: XPS spectrum (dark curve) and theoretical DOS calculation of ZnS [59].

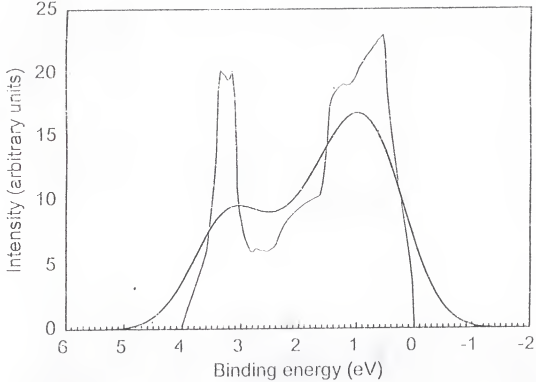

Figure 7: Convoluted theoretical DOS (dark curve) of ZnS with a Gaussian distribution of FWHM=1.25 eV [59].

Series [29], pages 61–126) is made. The static dielectric constant, $\varepsilon(0)$, for zincblende ZnS is measured to be from *8.0* to *8.9* at room temperature and this research finds *8.34* at *3 eV*; the optical dielectric constant, $\varepsilon(\infty)$, is measured to be *5.1* to *5.7* at room temperature and this research obtains *5.20* at *10.5 eV*. (Normally, for widegap semiconductors, the relative temperature coefficient, defined as $\frac{1}{\varepsilon_{11}}\frac{d\varepsilon_{11}}{dT}$, is about 3×10^{-4}. Therefore, an increase of *0.25* in dielectric constants at low temperature from room-temperature value is expected.) However, this comparison has to be taken cautiously because the optical dielectric constant does not originate from interband transition but rather from high-energy collective excitations (plasmons) of the material. Therefore, discrepancies of the optical constants from the linear interband transition contributions are expected.

As a note, this calculation can be easily extended to other linear response functions. In general, a linear response function may be expressed as

$$G(\omega) = \lim_{\epsilon \to 0^+} \frac{1}{\mathcal{N}} \sum_{\vec{k}} \frac{F\left(\vec{k}\right)}{\omega - \omega\left(\vec{k}\right) - i\epsilon}. \tag{9}$$

The complex dielectric function is a special case. The extension is straight forward given the knowledge of $F\left(\vec{k}\right)$.

·The comparison of the theoretical reflectivity is done with the experiments carried out in Dr. Holloway's group in the Department of Materials Science and Engineering at the University of Florida. This calculation assumes zero temperature but the experiments were done at room temperature. It is expected that details that are prominent at low temperature, such as critical points, tend to smear out at room temperature. In addition, energy shifts, as much as *200 meV*, can occur due to temperature effects. In Fig. 9, the low energy oscillation peak in experiment, below *3.7 eV*, is due to Fabry-Perot effect in the thin-film configuration and high energy data ends at *9.5 eV* due to shortage

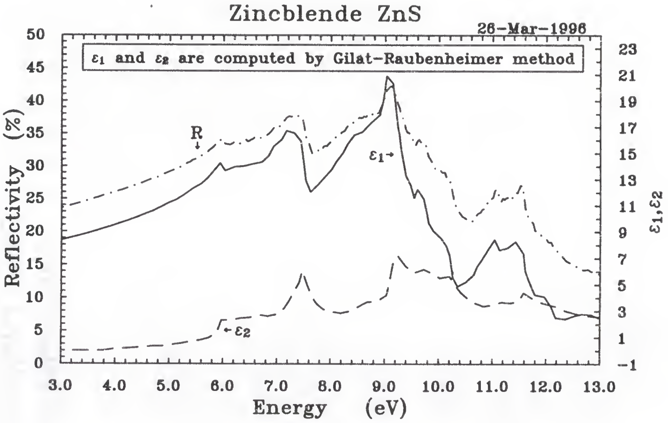

Figure 8: Dielectric constants and reflectivity for zincblende ZnS. Real part of the dielectric constant predominantly contributes to the reflectivity.

of tunable light source and lack of interest. The approximate *5%* difference between experiments and theory is not unusual. A possible explanation is that the surface of a thin film sample is contaminated. This reduces the effectiveness of the thin film to reflect incident light, and the well-established result (see Landolt-Börnstein New Series [29], page *380*) tends to support this possibility. Also, the approximation of constant optical transition probability within each of those smaller tetrahedra introduces further uncertainty though this uncertainty diminishes when the number of partitions for the irreducible BZ is increased. A check, however, showed that the theoretical reflectivity does not sensitively change with the number of partitions of the irreducible BZ.

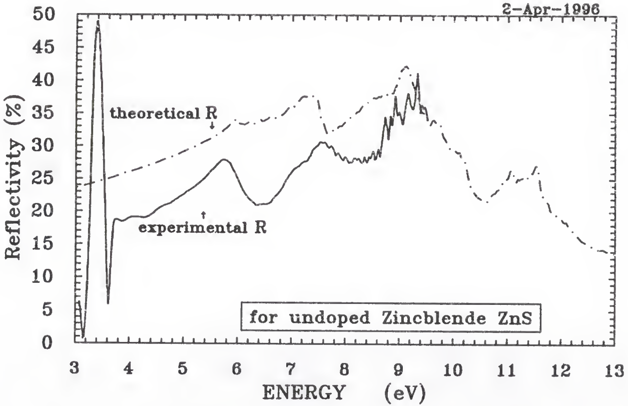

Figure 9: Theoretical reflectivity compared with experiment. The measurement covers up to *9.5 eV* and the peak at *3.4 eV* is due to Fabry-Perot effect.

CHAPTER 6
CONCLUSIONS

In this part of the research, the X-ray photoemission spectrum and the optical properties of zincblende ZnS are theoretically investigated. The empirical 30 × 30 $\vec{k} \cdot \vec{p}$ method has been employed to obtain the electronic structure in full BZ. A GR scheme was adopted for numerical integration over the BZ to find both DOS and dielectric constants of the material. Comparisons with well-established experimental data were made to establish the accuracy of the theoretical method and also allow the modeling of new experimental data by Dr. Holloway. As a result, the following conclusions are drawn:

- Bandstructure calculation is realistically accurate in the full Brillouin zone;
- Up to 10 compound semiconductors of zincblende structure have be computed;
- Gilat-Raubenheimer scheme is successfully utilized in the full BZ integration;
- Both experimental XPS and optical properties of zincblende ZnS are satisfactorily modeled.

PART III
QUANTUM CONFINEMENT EFFECTS IN CdTe

CHAPTER 7
INTRODUCTION

Quantum confinement effects (QCEs) have been shown to cause oscillatory behaviors in electronic, thermodynamic properties for metallic [62, 63], semimetallic, and semiconducting films [64-66]. In the last two decades, QCEs have been widely used to modify the optoelectronic properties of quantum semiconductor structures. Electronic properties which depend upon QCEs in semiconductors are electronic bandgap, density of states, and enhanced oscillator strengths of optical transitions. Different configurations, *i.e.*, dot, wire, film, and superlattice, are adopted to implement the corresponding design. The improved electronic structures allow better performances of the related quantum semiconductor devices. For instance, low threshold lasers have been implemented for GaAs/AlGaAs quantum well (QW) structures [8].

Theoretical efforts in the explanation of QCEs in semiconductors are not lacking[65, 67, 68]. On one hand, pseudopotential method and tight-binding method take into account of the full potential, which demands large-scale numerical calculations. On the other hand, among approximate methods, the envelop function approximation (EFA) [69, 70] is widely used, owing to its simplified factorization of the electronic wavefunction. However, the EFA method fails in strong confinement regime. In contrast, the truncated crystal approximation (TCA) [71] treats the enhanced QCEs in thin silicon quantum films successfully [68].

The TCA method predicts the electronic properties of the quantum semiconductor structures from those of the bulk materials, and *vice versa*. Quantum confinement effects in semiconductors are treated under the TCA method by applying semiclassical quantization conditions to the corresponding wavevector components of the carriers. To model QCEs on the absorption edge, a photo-excited electron-hole two-body system needs to be considered. In semiconductors with wide bandwidth, as manifested in the experiments (see Fig. 12 and Table 6), QCEs have a stronger $\frac{1}{L^2}$ blue-shift effect from the kinetic energy than the $\frac{1}{L}$ red-shift effect from the Coulomb interaction, where L is the confining size of the quantum structure. As a consequence, QCEs have a stronger contribution from bandstructure than that of the excitonic effect despite the fact that Coulomb correlation modifies the optical spectrum strongly, especially evident at low temperature. It is essential to take into consideration of the full zone bandstructure of the semiconductor when dealing with strong QCEs because approximate bandstructures, such as the Luttinger model and (non-)parabolic conduction band model, are far from accurate even at *5%* away from the high symmetry Γ point (refer to Figs. 10 and 11). This is the very reason why Efros-Efros theory [72] is deficient in treating strong QCEs, as exhibited in the experiments by Potter *et al.* [58]. Table 4 lists the calculated quantum dot sizes when *200 meV* discrepancy between the Γ transition points (refer to Eq. 29) as predicted by the TCA method occurs when using the full-zone bandstructure and approximate models for conduction and valence bands. Hence, the contribution from momentum quantization dominates QCEs for ordinary semiconductors though complications from the excitonic or surface effects may be expected in narrow bandwidth semiconductors.

Table 4: QD Sizes with *200 meV* Discrepancy between Calculated Absorption Edges by 30×30 $\vec{k} \cdot \vec{p}$ Model and Approximate Band Models.

Material	Effective Mass, m^*	α (1/eV) [a]	Size, L (Å)
GaAs	0.067	0.64	49.6
CdTe	0.11	0.45	34.8
ZnS	0.28	0.14	24.4
ZnSe	0.14	0.26	28.3

[a] α is used in the non-parabolic band model for the conduction band, as

$$E(1+\alpha E) = \frac{\hbar^2 k^2}{2m_e m^*}.$$

The experimental results on CdTe quantum dots in a transparent glass matrix by Potter *et al.* [58] indicate that QCE on the absorption edge deviates from both fully correlated and uncorrelated excitonic behaviors according to Efros-Efros theory after size distribution and finite barrier effect have been taken into account. The blue-shift effect on the absorption edge, about *1.0 eV* at the smallest particulate size, due to kinetic confinement is slightly offset by the red-shift effect due to Coulomb correlation, which can be estimated approximately using the binding energy of a free exciton in the bulk semiconductor, *i.e.*,

$$E_{ex} = -\frac{\mu e^4}{2\hbar^2 \epsilon^2 \epsilon_0^2} = -10.85\, meV \tag{10}$$

with $\mu = \frac{m_e m_h}{m_e + m_h}$ and value of parameters available in Table 1. Actually, the binding energy increases in lower dimensions and analytical result for 2D yields a fourfold increase. Therefore, the experimental data support the simple argument of kinetic

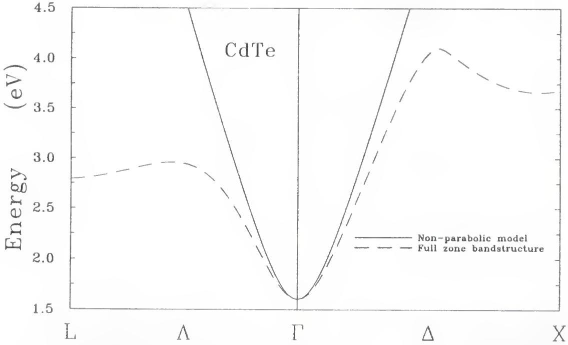

Figure 10: Comparison of non-parabolic model with 30 × 30 $\vec{k} \cdot \vec{p}$ model for conduction band. Clearly, previous model is unsuitable to describe carrier energies even at 5% off Γ point.

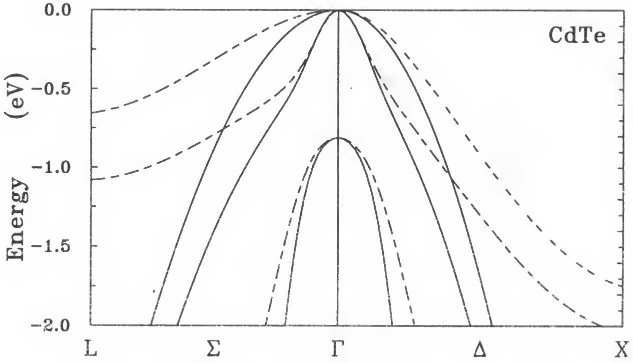

Figure 11: Comparison of Luttinger model with 30 × 30 $\vec{k} \cdot \vec{p}$ model. As shown, Luttinger model is deficient in predicting carrier energies off Γ point.

confinement effect predominating over Coulomb correlation effect. As a result, the TCA approach is applied to CdTe quantum dots system without the Coulomb effect to explain QCE on the absorption edge, and a satisfactory theoretical fit to the experiments is obtained for Γ point absorption energies and the fit for L point energy E_1 is within the theoretical error.

The EFA theory is applied to three typical multi-band Hamiltonian models in order to understand its applicability and to compare it directly with the TCA approach. The underlining issue is how to interpret the results of EFA when it is applicable to quantum confined systems. Concerning this, analytical solutions are sought for the two generic 2×2 models under the EFA theory so that ambiguity can be eliminated. The effort provides a satisfactory explanation of the failure of attempt to treat QCEs by applying the EFA theory with the empirical 30×30 $\vec{k} \cdot \vec{p}$ model by the author.

The present part is organized as follows: (1) in Chapter 8, the TCA method and the EFA theory are described, and then three models are discussed summarily; (2) in Chapter 10, theoretical results are presented for both theories and comparisons are made with experimental results; (3) in Chapter 10, discussions follow up to make the comparison of the two theories more transparent; and (4) finally, conclusions are given.

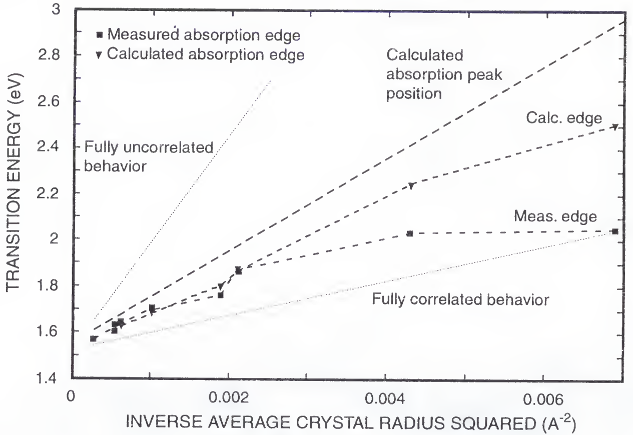

Figure 12: Measured absorption edge of CdTe quantum dots compared with calculated absorption edge [58]. The blue-shift effect, due to kinetic confinement, on the absorption edge is about *1.0 eV* at 24 Å and slightly offset by the red-shift effect due to Coulomb interaction.

CHAPTER 8
THEORIES

Low energy excitations in semiconductor materials are usually satisfactorily described by Maxwell-Boltzmann statistics, which results in successful application of independent electron quantum theory to quantum structures. As a note for mesoscopic metallic systems, new statistical model needs to be constructed because finite size and coherent nature of these systems invalidate ensemble averaging [62].

Truncated Crystal Approximation

For single electron in a uni-directionally (z) confining semiconductor structure, the following Schrödinger equation is solved

$$\widehat{H}\phi(\vec{r}_\perp, z) = E\phi(\vec{r}_\perp, z) \ , \tag{11}$$

where

$$\widehat{H} = \frac{\widehat{P}^2}{2m_e} + V(\vec{r}) + \frac{\hbar}{4m_e^2c^2}\left[\nabla V(\vec{r}) \times \widehat{P}\right] \cdot \vec{\sigma} \tag{12}$$

with confinement potential

$$V(\vec{r}) = \begin{cases} V_{mtl1}(\vec{r}) \ , & z < 0 \\ V_{mtl2}(\vec{r}) \ , & 0 < z < L \ . \\ V_{mtl3}(\vec{r}) \ , & z < L \end{cases} \tag{13}$$

Potentials $V_{mtli}(\vec{r})$, $i = 1, 2, 3$ are periodic in the perpendicular plane and assumed *not* to undergo structural change in the confining direction (z). *Under the TCA, the quantum structure with potential*

$$V(\vec{r}) = \begin{cases} \infty & , \quad 0 > z \geq L \\ V_{mtl}(\vec{r}) & , \quad 0 < z < L \end{cases} \tag{14}$$

is investigated, which represents impenetrable barriers.

To construct a complete TCA basis set, an observation is needed, which is, within the confinement region, the Schrödinger equation is still satisfied by the solutions for the bulk system. So *the solutions for the confined system are linear superposition of those degenerate solutions for the bulk system and the combination depend upon the broken symmetry from the bulk system to the confined system.* Therefore, for semiconductors with zincblende structure (cubic symmetry), the complete TCA basis set can be constructed, within a normalization factor for uni-directional confinement in the z direction, as

$$\varphi^{TCA}_{n\vec{k}_\perp j}(\vec{r}) = \begin{cases} \psi_{n\vec{k}_\perp+\vec{k}_z}(\vec{r}) - \psi_{n\vec{k}_\perp-\vec{k}_z}(\vec{r}) & ,0<z<L \\ 0 & ,0>z\geq L \end{cases} \tag{15}$$

where $\psi_{n\vec{k}}(\vec{r})$ is the Bloch wavefunctions and $\vec{k}_z = k_z\vec{z}$ is given by

$$k_z = \frac{\pi}{L}j \qquad ,j = 1,2,\ldots,j_L \tag{16}$$

with j_L as the maximum integer so that $\vec{k} = \vec{k}_\perp + \vec{k}_z$ is still inside the first Brillouin Zone (Brillouin Zone is used strictly in place of the first Brillouin Zone throughout the present thesis).

The TCA method, in the lowest-order approximation, assumes that solutions for the wavefunction $\phi(\vec{r}_\perp, z)$ are simply given by

$$\phi(\vec{r}_\perp, z) = \varphi^{TCA}_{n\vec{k}_\perp j}(\vec{r}_\perp, z) \tag{17}$$

so energy eigenvalues are given as

$$E = E_n\Big(\vec{k}_\perp + \frac{\pi}{L}j\hat{z}\Big), \qquad j = 1,2,\cdots,j_L. \tag{18}$$

Note that at $\vec{k}_\perp = \vec{0}$, owing to both quantization of the wavevector component $\vec{k}_z$ and nodal planes of the periodic part of a Bloch wavefunction at the confining barrier[68], the boundary conditions are satisfied. This basis set only *approximately* satisfies the boundary conditions away from $\vec{k}_\perp = \vec{0}$ because of the inequivalency of the two periodic parts of the Bloch wavefunctions, $u_{n\vec{k}_\perp+\vec{k}_z}$ and $u_{n\vec{k}_\perp-\vec{k}_z}$. This is one way in which errors are introduced into the TCA method. Using the complete basis set, Eq. (15), better approximations to solutions for the Schrödinger equation, Eq. (11), with confinement potential, Eq. (14), may be constructed. The lowest-order TCA method as outlined here can be conveniently extended to three dimensional quantum confinement cases for semiconductors with cubic symmetry. Therefore, *the TCA method obtains quantized energies simply by replacing the wavevectors in the confinement directions into the bulk bandstructures with their corresponding quantized values*, and then continuation needs to be considered to map out those subbands that were previously not fully inside the first BZ in 3D onto the new Brillouin Zone in lower dimensions in order to relate the total DOS of all subbands derived from each 3D band to the total number of unit cells in the confined system.

The TCA solutions, Eq. (17), may be used, when correlation effects are included, in calculations of interband and inter-subband optical transition, which are used for detailed comparison with optical measurements of quantum confined systems where excitonic effects strongly modify optical characteristics. Also, it is worth mentioning that a more detailed analysis is needed to study properties related to valence band mixing when crossover between subbands occur. In the case of multiply degenerate satellite valleys in indirect bandgap semiconductors, the TCA method can be constructed at local band minima but coupling between those accidentally degenerate states within each valley have to be taken account in the lowest order approximation.

Envelop Function Approximation

In dealing with physical systems that are characterized by two distinctively different length or time scales, adiabatic approximations can be used for analytical predictions. The Wenzel-Kramers-Brillouin (WKB) theory in quantum mechanics is a good example and the effective mass approximation (EMA), which is literally the EFA applied to the lowest conduction band of a semiconductor, is another. However, adiabatic approximations are not supposed to work for systems with comparable physical scales, such as for strong confinement systems in which unit cell scale and confinement scale are at the same order of magnitude, *i.e.*, ~ *10 Å*. This is precisely the reason why the envelop function approximation fails in strong confinement regime.

The envelop function approximation (EFA), or *the approximation of the wave envelop function* [70], in the literature mainly treats conduction and valence bands independently [14, 73] when dealing with semiconductor heterostructures and superlattices. However, as suggested in White and Sham's work [74], modeling conduction and valence bands on the same footing is essential for better matchup of boundary conditions, which, in return, means better results. Furthermore, with the increase of QCE, dipole matrix elements between highest occupied states and lowest unfilled states can *not* be predicted reliably by independent treatment of conduction and valence bands. Therefore, when formulating the EFA theory and selecting models in this research, conduction and valence bands are treated within the same model. Also, to a certain limit, numerical improvements are expected when more basis functions or bands are considered in the model.

Now consider an electron moving in a quantum semiconductor structure according to the Schrödinger equation, Eq. (11), under the potential given in Eq. (13). The first assumption in the EFA theory is that semiconductors involved have the same periodic basis wavefunctions $u_{n\vec{0}}(\vec{r})$ $\{n = 1, 2, \cdots, \infty\}$ at the Brillouin Zone center[1], and the second assumption is that they have the same crystal structure in the perpendicular plane. The first assumption is applicable only if no charge transfer occurs in the system, which then needs self-consistent treatment of a correlated electronic subsystem, while the second one usually is satisfied although strain effects may be introduced.

The basis wavefunctions $u_{n\vec{0}}(\vec{r})$ satisfy the following equation

$$[\hat{P}^2 + V^{sym}_{mtli}(\vec{r}) - \epsilon^{mtli}_m]u_{m\vec{0}}(\vec{r}) = 0, \qquad i = 1, 2, 3 \tag{19}$$

for all three materials in the whole real space, and

$$V_{mtli}(\vec{r}) = V^{sym}_{mtli}(\vec{r}) + V^{asym}_{mtli}(\vec{r}), \qquad i = 1, 2, 3 \tag{20}$$

where $V^{asym}_{mtli}(\vec{r})$ is the antisymmetric part of the lattice potential $V_{mtli}(\vec{r})$ with respect to exchange of anion and cation so it vanishes for semiconductors of Diamond structure.

Using a complete basis set of the Bloch wavefunctions

$$\{ \frac{e^{i\vec{k}\cdot\vec{r}}u_{n\vec{0}}(\vec{r})}{\sqrt{N\Omega}} \quad , \quad \vec{k} \in B.Z. \, , \; n = 1, 2, \ldots, \infty \} \, , \tag{21}$$

a single electron wavefunction can be expanded as

$$\phi(\vec{r}_\perp, z) = e^{i\vec{k}\cdot\vec{r}} \sum_n \chi_n(z) u_{n\vec{0}}(\vec{r}) \, , \tag{22}$$

where $\chi_n(z)$ is called *the envelop function*. Since the perpendicular wavevector is still a good quantum number, the Schrödinger equation can be reduced to its final form,

---

[1] As a new development in the EFA theory, Foreman [Phys. Rev. B54, 1909–21, 1996] formulated the theory "with material-dependent basis functions".

Eq. (24), after integrating out the fast-alternating periodic potential using the following approximation

$$\int d\vec{r} f(\vec{r})\alpha(\vec{r}) \approx \int d\vec{r} f(\vec{r}) \cdot \frac{1}{\Omega} \int_{unit\ cell} d\vec{r}\alpha(\vec{r}) \,, \tag{23}$$

where function $\alpha(\vec{r})$ has the periodicity of the potential, and function $f(\vec{r})$ is slowly varying on the length scale of function $\alpha(\vec{r})$. For semiconductor heterostructures, though abrupt changes in the potential at the interfaces occur, it is often assumed that the above approximation holds. The validity of the EFA is called into question with an increase of the degree of confinement. And the final form of the Schrödinger equation under the EFA is

$$\begin{aligned} &\left(\widehat{P}_z^2 + P_\perp^2 + \epsilon_m - E\right)\chi_m(z) + \sum_n \{\langle m|V^{asym}(\vec{r}) + \widehat{H}_{so}|n\rangle \\ &+ 2\langle m|\widehat{P}_\perp|n\rangle \cdot \vec{P}_\perp + 2\langle m|\widehat{P}_z|n\rangle \cdot \widehat{P}_z\}\chi_n(z) = 0 \,, \end{aligned} \tag{24}$$

where $\langle m|\widehat{O}|n\rangle = \int_{unit\ cell} d\vec{r} u^*_{m\vec{0}}(\vec{r})\widehat{O}u_{n\vec{0}}(\vec{r})$ for arbitrary operator, and $\widehat{H}_{so}$ is the spin-orbital coupling interaction. Note that Eq. (24) holds in different regions of the system with different material parameters and is applicable to all quantum structures that are *not* under strong confinement. Therefore, *the envelop function approximation means replacing the symmetry-broken quantum number with its corresponding operator in the model Hamiltonian of matrix form.*

Hamiltonian Models

Under the envelop function approximation, multiband models, which use a limited number of basis functions, may allow nontrivial results, in reference to the inverse square behavior as predicted with a non-parabolic model for conduction band and Luttinger model for valence bands. Multiband models that treat conduction and valence bands on the same footing are discussed here, as mentioned in the previous section.

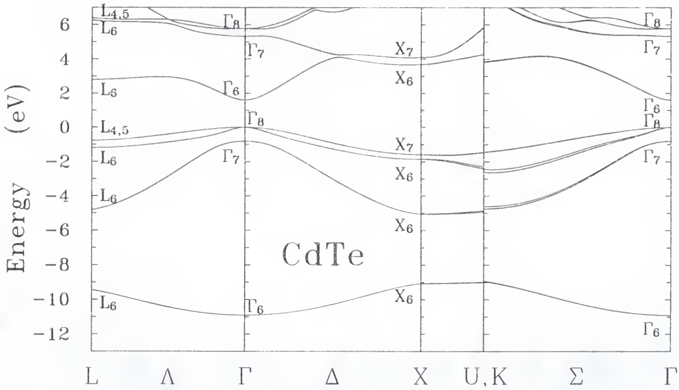

Figure 13: Bandstructure of zincblende CdTe computed by the empirical 30 × 30 $\vec{k} \cdot \vec{p}$ method.

Table 5: $\vec{k} \cdot \vec{p}$ Results for CdTe Compared with Reported Values in Literature.

Parameter	$\vec{k} \cdot \vec{p}$ Results	Literature [29]
E_g (eV)	1.603	1.59
Δ_0 (eV)	0.813	0.81
Δ_1 (eV)	0.42	0.6
$E_{\Gamma L}$ (eV)	1.189	
$E_{\Gamma X}$ (eV)	2.082	
m_e^*	0.141	0.11
$< 111 >^a$ m_{hh}^*	1.258	
$< 100 >^b$ m_{hh}^*	0.646	
$< 111 >^a$ m_{lh}^*	0.167	
$< 100 >^b$ m_{lh}^*	0.190	
$< 111 >^a$ m_{so}^*	0.317	
$< 100 >^b$ m_{so}^*	0.330	

[a] $\lim_{k \to 0} |\hbar^2 / \partial^2 E / \partial k^2|$, defined for k along Γ and L.
[b] $\lim_{k \to 0} |\hbar^2 / \partial^2 E / \partial k^2|$, defined for k along Γ and X.

3D 30 × 30 $\vec{k} \cdot \vec{p}$ Theory

Cardona's 15 × 15 $\vec{k} \cdot \vec{p}$ model [75-78] is extended to the current 30 × 30 one by incorporating the spin-orbital coupling interaction. Due to a lack of translational symmetry, all $\vec{k} \cdot \vec{p}$ models without modification are intrinsically incapable of dealing with QCEs under the EFA theory. Therefore, they are restricted in use to the TCA method. However, they work satisfactorily with the TCA method even when strong quantum confinement is in effect, as the results of this research will demonstrate. Reconstructed $\vec{k} \cdot \vec{p}$ models that are capable of dealing with quantum heterostructures are available [79, 80].

Listed in Tables 3 and 5 are the complete set of 30 × 30 $\vec{k} \cdot \vec{p}$ parameters and an incomplete list of bandstructure and material parameters obtained from the computation. Figure 13 shows the electronic structure of bulk zincblende CdTe as computed by the empirical 30 × 30 $\vec{k} \cdot \vec{p}$ method. It is necessary to stress that all computation is done at zero temperature, and this could causes deviation from room temperature values as much as *0.2 eV* as far as energy levels are concerned.

1D 2 × 2 $\vec{k} \cdot \vec{p}$ Model

A 2 × 2 $\vec{k} \cdot \vec{p}$ model is considered here. It is analytically tractable under the EFA theory. This model is used to provide insight into the failure of the 30 × 30 $\vec{k} \cdot \vec{p}$ model under the EFA theory. It elucidates features that are not transparent in the 30 × 30 model, such as the origin of the '*spurious states*' and model-independent properties. Furthermore these two models allow direct comparisons between the EFA theory and TCA method.

The Hamiltonian for 1D 2 × 2 $\vec{k} \cdot \vec{p}$ model reads, in atomic units, as

$$H = \begin{pmatrix} k^2 & Pk \\ Pk & E_g + k^2 \end{pmatrix} \quad , \tag{25}$$

with E_g and P as bandgap and $\vec{k} \cdot \vec{p}$ coupling constant, and given as in the 3D 30 × 30 $\vec{k} \cdot \vec{p}$ model. Eigenvalues for Eq. (25) are

$$\epsilon_\pm = \frac{E_g}{2} + k^2 \pm \sqrt{\left(\frac{E_g}{2}\right)^2 + P^2k^2} \quad . \tag{26}$$

1D White-Sham Model

White-Sham model was introduced for heterostructures in order to incorporate evanescent states [74], or '*wing states*' to better satisfy interfacial continuity conditions. Derived from the original three-band Kane's model [81, 82], the current model considers a two-band effective Hamiltonian for electron and heavy hole, and it is called the 'White-Sham model'. This model is complementary to the previous model, but differs from the previous one in modeling the valence band with a negative curvature (see the insets in Figs. 18 and 20 for details). The model reads, in atomic units, as

$$H = \begin{pmatrix} -k^2 & Pk \\ Pk & E_g + k^2 \end{pmatrix} \tag{27}$$

with parameters E_g and P of same meaning as in 2×2 $\vec{k} \cdot \vec{p}$ model. Eigenvalues for Eq. (27) are

$$\epsilon_\pm = \frac{E_g}{2} \pm \sqrt{\left(\frac{E_g}{2}\right)^2 + (E_g + P^2 + k^2)k^2} \quad . \tag{28}$$

CHAPTER 9
RESULTS

Our theoretical calculations include various quantum confinement structures, especially quantum dots. The results are shown in Fig. 14-17 with discussions followed in next chapter. For comparison, Table 6 lists the relevant experimental data as appeared in [58].

Table 6: Results of CdTe QDs and Calibrated Absorption Edges by Potter [58].

Average Diameter (Å)	Measured Γ-point Absorption Edge Energy (eV)	Calculated Γ-point Absorption Edge Energy (eV)	Measured L-point E_1 Energy (eV)	Measured L-point $E_1+\Delta_1$ Energy (eV)
24	2.05	2.50	3.55	4.14
30	2.03	2.24	3.52	4.16
43	1.87	1.88	3.43	4.03
46	1.76	1.79	3.39	4.00
66	1.68	1.66	3.34	3.92
79	1.65	1.63		
85	1.63	1.62	3.36	3.97
86	1.61	1.62	3.32	3.9
125	1.56	1.56	3.29	3.88

Truncated Crystal Approximation

As pointed out in the theory section, the TCA method for regular quantum structures means mapping 3D electronic structural cross sections into a lower dimensional BZ along the quantization direction(s). Results of 1D quantum confinement effects on the electronic energy levels for CdTe quantum film are shown in Fig. 14. As clearly seen, the warping nature of the valence bandstructure results in negative hole effective masses for certain subbands when the confinement effect is strong.

In order to model realistic (spherical) quantum dots which are confined in 3D, an equal volume scheme is adopted. Calculation of bandstructure quantization of a quantum dot is done for a quantum cube of the same volume of the spherical dot as measured in the experiments [58]. That is, the confinement width L_{cube} is scaled according to $L_{cube} = \sqrt[3]{\frac{\pi}{6}} D_{dot}$ with D_{dot} being the diameter of the quantum dot. This scheme works in the loose sense of interpolation. Then, for the sake of continuation because there is no Brillouin zone anymore, association of quantized wavevectors with high symmetrical points in the Brillouin Zone is made as follows,

$$\begin{aligned}
&(\frac{\pi}{L}, \frac{\pi}{L}, \frac{\pi}{L}) && \rightarrow \Gamma \\
&(\frac{\pi}{L}, \frac{\pi}{L}, j_L * \frac{\pi}{L}) && \rightarrow \mathrm{X} \\
&(\frac{\pi}{L}, j_L * \frac{\pi}{L}, j_L * \frac{\pi}{L}) && \rightarrow \mathrm{K} \\
&(j_L * \frac{\pi}{L}, j_L * \frac{\pi}{L}, j_L * \frac{\pi}{L}) && \rightarrow \mathrm{L}
\end{aligned} \tag{29}$$

where j_L is the maximum integer allowed so that the corresponding wavevector is within the Brillouin Zone. For different symmetric points, j_L differs.

Comparison of the theoretical results with the experimental optical transition energies of CdTe QDs in a transparent glass matrix [58] is shown in Fig. 17. Over the whole

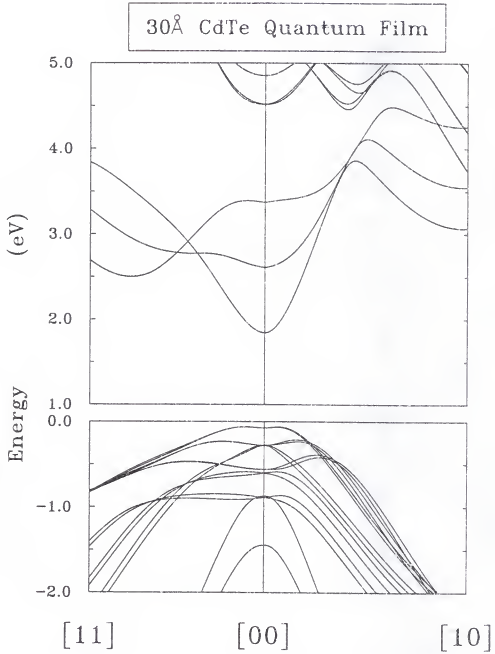

Figure 14: Truncated Crystal Approximation (TCA) result of 30 Å CdTe quantum film. The TCA method maps the quantized cross sections of the electronic structure onto the unaffected plane. Shown are the first three subbands from each band in the bulk. Reflected clearly are the warping nature of the valence bands and the lift of the double degeneracy at the top of the valence bands.

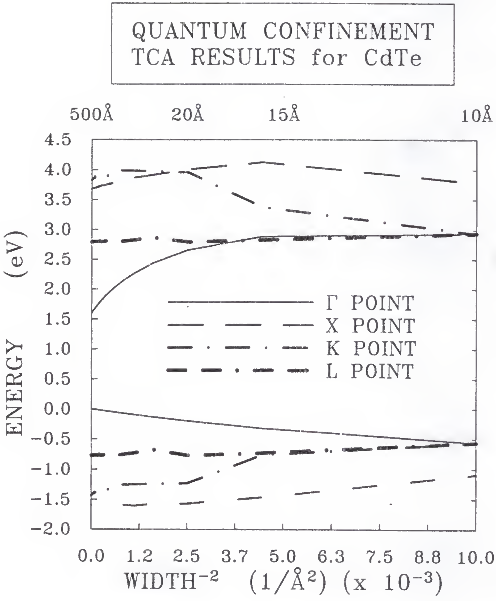

Figure 15: Predicted bandedges at symmetrical points of CdTe quantum cube by the TCA method. No inverse square behaviors are found and asymptotic saturation of quantum confinement effect on the bandedges is predicted.

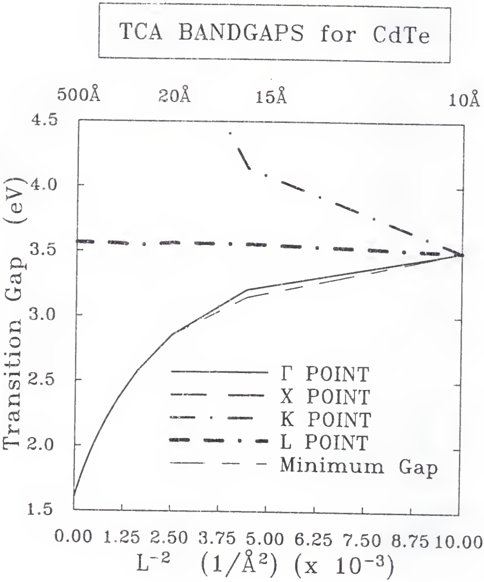

Figure 16: Predicted transition energies of CdTe quantum cube by the TCA method. Γ point is the absorption edge above 16 Å and then replaced by an unidentified point in some general direction.

range of measurement, the result is in excellent agreement with the experiment. The experimental data has been corrected for effects of size distribution and quantum tunneling into glass barriers.

Despite the fact that the TCA method is satisfactorily applied to the CdTe quantum confinement problem, the application of the EFA method with 30×30 $\vec{k} \cdot \vec{p}$ model to the problem turns out to yield un-physical results. To understand this paradox, two 2×2 analytical Hamiltonian models are used with both methods for comparison. The results are shown in the next section together with those of the EFA method.

The TCA solutions for 1D 2×2 $\vec{k} \cdot \vec{p}$ model are

$$\epsilon_{\pm}^{(n)} = \frac{E_g}{2} + \left(\frac{n\pi}{L}\right)^2 \pm \sqrt{\left(\frac{E_g}{2}\right)^2 + P^2\left(\frac{n\pi}{L}\right)^2} \quad . \tag{30}$$

As shown in Figs. 18 and 19, no agreement of any kind is produced between the EFA method and TCA approach. However, for the White-Sham model, whose TCA solutions are

$$\epsilon_{\pm}^{(n)} = \frac{E_g}{2} \pm \sqrt{\left(\frac{E_g}{2}\right)^2 + [E_g + P^2 + \left(\frac{n\pi}{L}\right)^2]\left(\frac{n\pi}{L}\right)^2} \quad . \tag{31}$$

Excellent agreement, as shown in Fig. 20, is found among analytical, numerical, and TCA results.

Envelop Function Approximation

The EFA method is applied to both 2×2 models and the results are compared between the two models in addition to being compared with the TCA results in order to elucidate the failure of the application of the EFA method with 30×30 $\vec{k} \cdot \vec{p}$ model. The EMA theory, the simplest form of the EFA theory, predicts the well-known inverse square dependence of quantization of energy levels upon confinement width. The same

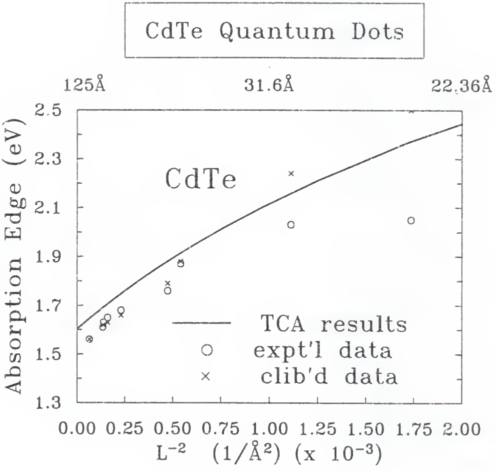

Figure 17: Experimental data compared with TCA predictions for CdTe quantum dots. The experimental data are corrected by considering size distribution and tunneling into finite glass barriers. Discrepancy at large L limit is because the TCA predictions are for QDs at zero temperature.

inverse square behavior is found for the White-Sham model, as shown below. Though improved in agreement through more accurate bandstructures, the 2×2 $\vec{k} \cdot \vec{p}$ model does not yield converging results.

Parameters for the 2×2 models are fit to zincblende ZnS instead of CdTe but conclusions are not affected. Finite difference scheme is adopted to solve the corresponding differential equations for the 2×2 models. Numerical and analytical results are obtained simultaneously for assurance.

The analytical results for 2×2 $\vec{k} \cdot \vec{p}$ model are obtained by solving Eq. (32) numerically for the quantized wavevectors k_1, k_2, and the quantized energies ϵ. The algebraic equations

$$\begin{cases} k_{1,2}^2 = \epsilon - \frac{E_g}{2} + \frac{P^2}{2} \pm \sqrt{\left(\frac{E_g}{2}\right)^2 + \frac{1}{2}\left(\epsilon - \frac{E_g}{2}\right) P^2 + \frac{1}{4} P^4} \\ \sin k_1 L \sin k_2 L = (1 - \cos k_1 L \cos k_2 L) * \\ \qquad \frac{2\Delta_1(k_1)\Delta_1(k_2)\Delta_2(k_1)\Delta_2(k_2)}{\Delta_1^2(k_1)\Delta_2^2(k_2) + \Delta_1^2(k_2)\Delta_2^2(k_1)} \end{cases} \tag{32}$$

where $\Delta_1(k) = E_g + k^2 - \epsilon$, $\Delta_2(k) = -Pk$, for quantized energies ϵ at k_1 and k_2 are derived when solving an eigenvalue problem under zero boundary conditions [63]. The analytical results are compared with TCA results in Figs. 18 and 19, and no agreement between the two methods is obtained. Also diverging behavior is found for this model when numerical solutions are sought. This behavior will be addressed in the discussion, though it is worth pointing out that the valence band, in the whole real plane, introduces '*spurious states*', *i.e.*, those larger k solutions in Eq. (32) when $\epsilon > E_g$, which are unphysical and due to the faulty model. Because of the lack of numerical convergence in 2×2 $\vec{k} \cdot \vec{p}$ model, the effort to extend the Envelop Function Approximation to 30×30 $\vec{k} \cdot \vec{p}$ model was abandoned. In retrospective, the study of the 2×2 $\vec{k} \cdot \vec{p}$ model was to shed light on the cause for the numerically diverging behavior.

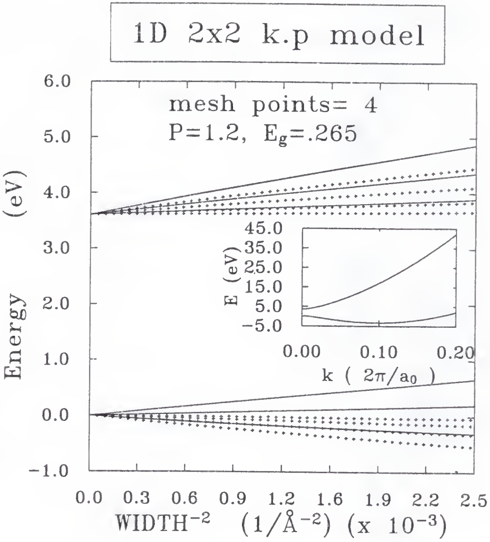

Figure 18: Comparison between numerical EFA and TCA results. Solid lines are EFA calculations with 4 mesh points in finite difference scheme. Inset shows 1D 2×2 $\vec{k} \cdot \vec{p}$ model, which is asymptotically parabolic for both bands.

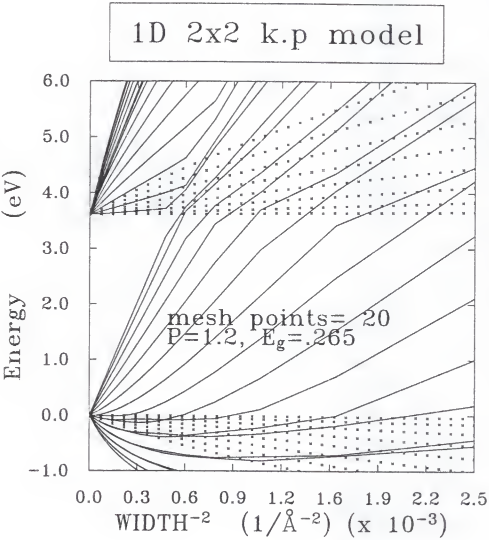

Figure 19: Comparison between numerical EFA and TCA results. Solid lines are for EFA calculations with 20 mesh points. Compared to EFA results with 4 mesh points (Fig. 18) and TCA results, no agreements between EFA results with different mesh points and between EFA and TCA results have been achieved.

The White-Sham model is studied in comparison with the same parameters for 2×2 $\vec{k} \cdot \vec{p}$ model in order to understand the differences among various models. The quantized energy and the wavevectors k_1, k_2 are obtained by solving the following algebraic equations

$$\begin{cases} k_{1,2}^2 = -\frac{E_g+P^2}{2} \pm \sqrt{\left(\frac{E_g+P^2}{2}\right)^2 + \epsilon(\epsilon - E_g)} \\ \sin k_1 L \sin k_2 L = (1 - \cos k_1 L \cos k_2 L) * \\ \qquad \frac{2\Delta_1(k_1)\Delta_1(k_2)\Delta_2(k_1)\Delta_2(k_2)}{\Delta_1^2(k_1)\Delta_2^2(k_2)+\Delta_1^2(k_2)\Delta_2^2(k_1)} \end{cases} \tag{33}$$

where $\Delta_1(k) = E_g + k^2 - \epsilon$, $\Delta_2(k) = -Pk$. The difference between 2×2 $\vec{k} \cdot \vec{p}$ model and the White-Sham model is the way in which the valence band is modeled: in the former model, the valence band is an asymptotical positive parabolic which allows real solutions to the other pair of k's in Eq. (32) when $\epsilon > E_g$; while in the White-Sham model, the the valence band is an asymptotical negative parabolic which allows only imaginary solutions to the other pair of k's in Eq. (33) when $\epsilon > E_g$. This distinctive difference is obvious in the two insets of Fig. 18 and Fig. 20. As shown in Fig. 20, excellent agreement is achieved between the EFA and TCA method.

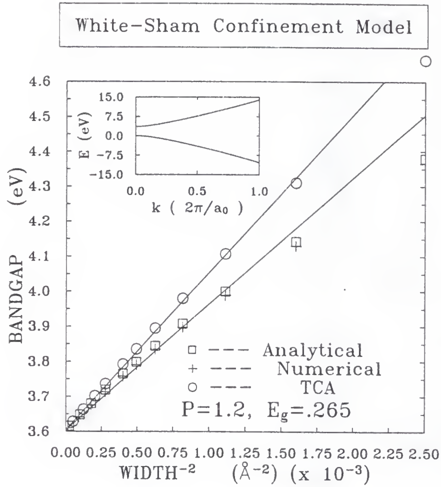

Figure 20: Analytical, numerical and TCA results of the White-Sham model. Straight solid lines are for viewing guide. The inset shows the bands as predicted by the White-Sham model. Excellent agreements have been achieved among all results.

CHAPTER 10
DISCUSSION

Multiband models using the EFA theory simply mix degenerate states from the bulk material when dealing with QCEs, and a mixture state in quantum structure is far from similar to an envelop function on top of the original Bloch wavefunction. Hence it is reasonable to believe that the EFA theory is at fault in dealing with QCE because of this lack of self-consistency. But every evidence shows that this belief is far from the truth. This is an example of a non-self-consistent theory that works. This, in another way, suggests why the TCA method succeeds when applied to QCE problems because those basis functions, Eq. (15), constructed based upon the notion of destructive interference, approximately take into consideration both degenerate states mixing and boundary conditions.

Truncated Crystal Approximation

When dealing with quantum confinement systems, because of the abrupt changes in the potential profiles, the EFA theory will not only couple degenerate states but also discretize the electronic energy levels in order for the wavefunctions to satisfy the boundary conditions. In order to handle the ever-decreasing-in-size nanosystems empirically, more and more basis functions are needed to construct an accurate multiband Hamiltonian. It means more difficulty, if not impossible, to solve the coupled differential equations either analytically or numerically under the EFA method.

On the other hand, though unfit for treating quantum confinement problems under the EFA theory because of '*spurious states*', 30×30 $\vec{k} \cdot \vec{p}$ model under the TCA approach has been successfully applied to treat quantum confinement problems. Surprisingly as it seems, the reason for this paradox is as follows. All models that have been discussed in this research are approximate ones since all of them fail to include the fundamental symmetry of spatial periodicity in solids. The Hamiltonians would have been periodic in k space if translational symmetry were considered. This very defect in the $\vec{k} \cdot \vec{p}$ models introduces '*spurious states*', which are unphysical solutions and beyond the Brillouin Zone, when QCEs are treated under the EFA theory. It is this artificial deficiency in the $\vec{k} \cdot \vec{p}$ model that spells failure for application of the EFA theory to QCE. For the TCA approach, it is the very approximation that was made when constructing the basis functions to decouple states in the Brillouin Zone from those degenerate states beyond the Brillouin Zone fundamentally guarantees the success of the approach. The physical reason for the success is because, as pointed out in discussion above, the TCA basis functions, Eq. (15), constructed upon notion of destructive interference, take both degenerate state mixing and boundary conditions into consideration [68]. However, when sizes of quantum structures are reduced further, their physical properties deviates more and more from those of bulk materials and approach those of molecules. This extreme limit invalidates the TCA method, which predicts the properties of a cluster from those of bulk material.

Improvement of the 30×30 $\vec{k} \cdot \vec{p}$ model under the TCA method calculation is possible if more TCA basis functions are used in a higher order approximation. Furthermore, as suggested in Fig. 17, inclusion of excitonic effect, which should reduce transition energies, should improve the agreement between the theory and the experiments as well. It is beyond this crude approximation of the TCA method to study quantum confined systems which change drastically and qualitatively with the size and dimension of the systems. Then, higher order approximations are required, such as in the case of Si quantum wires and thin films, which involves multiple degeneracy.

Envelop Function Approximation

The experiments [58] show deviation from the $\frac{1}{L^2}$ inverse square behavior, *i.e.*, energy levels quantize in proportion to the inverse square of the confinement size of the structure. As calculation indicates, the rather general models that are discussed under the EFA theory either reproduce trivial inverse square behavior or fail to yield physically meaningful results over the whole confinement range. Beyond the weak quantum confinement range, first the theory becomes incapable, then the theory turns invalid when the confinement size is comparable to the unit cell. Therefore, *the envelop function approximation may be applicable to weak quantum confinement problems, but care in selecting Hamiltonian models should be exercised.* Also, the Efros-Efros theory predicts the same trivial inverse square behavior even though it considers Coulomb correlation, which indicates the inadequacy of this theory in dealing with QCE and the less importance of the excitonic effect.

Defect in the models, which means lack of consideration of the spatial periodicity, and the approximate nature of the EFA theory are the reasons for the inadequacy of the theory to treat quantum confinement effect. For the 1D 2×2 $\vec{k} \cdot \vec{p}$ model, analytically there are always two positive solutions for k^2 according to Eq. (32) when $\epsilon > E_g$, so a pair of real solutions for k exist from the larger solution of k^2. This pair of real solutions for k are called '*spurious states*' [70] because they are outside the Brillouin Zone and unphysical since they would be nonexistent if spatial periodicity of the system were considered. Numerically, these '*spurious states*' are mapped as energy eigenstates from outside the Brillouin Zone, thus cause numerical instability and convergence problem.

Different from 1D 2×2 $\vec{k} \cdot \vec{p}$ model, for 1D White-Sham model, there are always one positive and one negative solution for k^2 according to Eq. (33) when $\epsilon > E_g$. Then the negative solution for k^2 yields a pair of imaginary solutions for k which are called '*wing states*' [74] because they have larger amplitudes than the real solutions of k. These '*wing states*' are evanescent states, so they cause no numerical problems. The two bands in the White-Sham model asymptotically decouple into two independent bands except for introducing the '*wing states*', which is equivalent to two independent bands under the effective mass approximation. It is no wonder that this model reproduces the trivial inverse square behavior. Therefore, the White-Sham model under the EFA theory is applicable to QCEs but reproduces trivial results in strong confinement regime, and 2×2 $\vec{k} \cdot \vec{p}$ model *can not* be used under the EFA theory due to the defect in the model.

As a note, the Luttinger model for valence bands [83] is also investigated and the same trivial inverse square behavior for small quantum systems is found though better quantitative agreement is achieved beyond intermediate quantum confinement range between the EFA theory and the TCA method, though no results are given here. Conclusion can be drawn that *multiband Hamiltonian model that does not produce 'spurious states' is applicable for study of QCEs under the EFA theory and quantitatively improves the agreement as the number of basis functions increases, though trivial results are produced in strong confinement regime.*

CHAPTER 11
CONCLUSIONS

Quantum confinement effects on the absorption edge in CdTe quantum dots have been satisfactorily modeled by using an empirical full zone 30×30 $\vec{k} \cdot \vec{p}$ model with the TCA method The theoretical results are in agreement with experimental data for zincblende CdTe clusters in a transparent glass matrix. However, the application of this model within the EFA theory framework fails to produce converging numerical results.

Study on $\vec{k} \cdot \vec{p}$ models and White-Sham model with both the EFA theory and the TCA approach allows exploration of detailed aspects of these models and comparison between the two theories. The $\vec{k} \cdot \vec{p}$ models with the TCA method are applicable to make reliable predictions for quantum confinement effects until the molecular aspects of the quantum systems dominate. Furthermore, increasing the number of basis functions improves the accuracy of the modeling.

On the contrary, under the EFA theory, owing to the lack of consideration of the translational symmetry, $\vec{k} \cdot \vec{p}$ models are inapplicable for modeling QCE. On the other hand, the White-Sham model, though suitable for describing QCE, predicts the trivial inverse square behavior in strong quantum confinement regime, which is a manifestation of the asymptotically parabolic dispersions for large wavevectors in White-Sham model.

PART IV
STATIC SCREENING AND MOBILITY IN n-ZnSe

CHAPTER 12
INTRODUCTION

Zinc selenide is a commercial blue/green light-emitting diode (LED) material, and has been intensively studied in recent years. In quantum-well (QW) LED and laser devices, ohmic contacts need to be made, as electrodes, to the active region where carriers can be injected, recombine, and thus emit light. Heavily doped ZnSe is commonly used in the bandgap grading scheme [12] to make ohmic contact, and the carrier mobility of intermediately to heavily doped semiconductor is an important reliability parameter. Among all major mechanisms that determine the mobility, ionized impurity scattering becomes predominant at low temperature (usually < *25 K*), and gets enhanced under heavy doping. Furthermore, heavy doping can induce metal-insulator transitions in semiconductors.

Heavily doped semiconductors have been extensively studied for possible applications in solar cells, tunneling devices and metallization. In a heavily doped semiconductor, impurity band may be formed due to spatial overlap between the electronic wavefunctions of neighboring impurities. Disorder in the system leads to the existence of a *mobility edge* in the impurity band. Above the edge, conduction is free-electron-like, and below the edge, conduction is possible by variable-range hoppings. A semiconductor becomes metallic when the chemical potential of the system passes through the *mobility edge* with increasing doping level. This transition is well-known as the Anderson transition [84-86]. In comparison, intermediately doped semiconductors are not well understood, especially near the transition. This research is motivated by this fact and attempts, qualitatively, to explain the experiments by Park and Simmons [87].

In order to understand a system with wide range of doping, a self-consistent theory was proposed for determination of the chemical potential, static screening effects and ionization of impurities. For simplicity, only single-level hydrogen-like donors and acceptors are considered for impurities. Static screening is treated by a generalized Debye theory[1]. Mobility due to ionized impurity scattering is obtained by application of the *relaxation time approximation* to the Boltzmann kinetic equation (BKE)[2]. The theory is applicable to other widegap semiconductors, though *formation of impurity bands at high doping concentration has not been taken into account because (1) the intermediate doping regime is of major interest for this research; (2) the impurity bands may disappear as a result of screening; (3) the mobility is mainly determined by free carriers in the bulk conduction band.* Also, we neglect the bandgap narrowing due to doping, which is assumed to be far smaller than the wide bandgap of the system [7]. No consideration of fluctuations in impurity potentials and impurity conduction has been taken. Only a uniformly doped semiconductor is under consideration.

It is found that (1) static screening, as predicted by the generalized Debye theory, can induce an abrupt metal-insulator (MI) transition, with a *critical temperature* found at *26.5 K*, for uncompensated systems with donor concentration above $10^{17} cm^{-3}$ inclusive and no such transition for a highly compensated system (see Figs. 26 and 33); (2) static screening, as predicted by the generalized Debye theory, induce a smooth MI transition for highly compensated systems and the *critical donor concentration* is found at $10^{17} cm^{-3}$; (3) static screening drastically affects the system when donor concentration is well below the critical concentration of metal-insulator transition, given by Eq. (34); (4) donor level[3] is reduced due to static screening; (5) free carriers can be reduced by an order of magnitude for compensated systems at high donor concentration (see Fig. 34); (6) the generalized Debye theory over-estimates the static screening effect. The present theory was compared with the experiments of Park and Simmons, and a partial and qualitative agreement is achieved.

---

[1] Sometimes called the Debye-Huckel theory.

[2] Interchangeably used for the Boltzmann transport equation in the present thesis

---

[3] or donor binding energy, as used throughout the present part.

CHAPTER 13
BACKGROUND

Carrier mobility in a semiconductor device is an important parameter which essentially determines how fast the device can operate. One of the technological aspirations of semiconductor community is to increase the carrier mobility. Higher mobility means speedier devices and improvements in performance. Mobility of free carriers is determined by how often and how intense they scatter off irregularities in a semiconductor, such as defects, impurities, interfacial discontinuities and dynamical excitations. Among those important scattering mechanisms that limit the carrier mobility in widegap semiconductors near equilibrium are polar LO-phonon and ionized impurity scatterings. Carrier-carrier and plasmon scatterings become prominent for poorly screened systems with high carrier concentration. Doping not only introduces impurities but also increases carrier concentration, therefore it affects carrier dynamics. Overdoped semiconductors may undergo Anderson transition and become metallic, but with lower carrier mobility. The critical donor concentration N_d^{cr} for uncompensated n-type semiconductors is predicted by

$$N_d^{cr\,\frac{1}{3}} a_H^d \approx 0.27 \tag{34}$$

with a_H^d being the hydrogen radius $\hbar^2 \epsilon_0 \kappa / m_e^* m_e e^2$ for electrons, κ being the relative dielectric constant[1], ϵ_0 being the dielectric constant in vacuum, m_e^* being the relative electron effective mass, and m_e being free electron mass. Using parameters in Table 7, it is found, for uncompensated n-ZnSe, that

---

[1] In Table 1, it is denoted as ϵ_0.

$$N_d^{cr} = 8.389 \times 10^{17} cm^{-3} . \tag{34'}$$

The overall performance of semiconductor devices is enhanced if operated at low temperature because of reduction of the number of scattering events due to thermal excitations. The influence of different kinds of scatterings on carrier mobility depends upon temperature and carrier concentration differently. Conventionally speaking, ionized impurity scatterings have a weaker temperature dependence than other mechanisms but a stronger carrier concentration dependence. Hence at low temperature (for example, *4.2 K*) or high impurity concentration (over $10^{18} cm^{-3}$), ionized impurity scattering determines the carrier mobility of a semiconductor, while polar LO-phonon scatterings compete with ionized impurity scatterings as the temperature rises or impurity concentration decreases. For elastic scatterings, which ionized impurity scatterings are, *relaxation time approximation* can be applied to predict the carrier mobility which is directly proportional to the *relaxation time*. The *relaxation time* is defined with respect to energy, which measures the intensity of scatterings at a given energy. However, optical phonon scattering at medium temperature can not be treated as an elastic process, and therefore a *relaxation time approximation* is invalid.

Owing to its strong dependence upon carrier concentration, the *conventional* weak temperature dependence of ionized impurity scatterings can be drastically changed in and above intermediate temperature range, given the approximately exponential relationship between carrier concentration and temperature. First of all, temperature and impurity concentrations are independent variables, while carrier concentrations depend upon temperature and impurity concentrations. Then, the chemical potential varies according to charge neutrality at different temperatures Thirdly, the carrier statistics may change from Maxwell-Boltzmann (MB) to Fermi-Dirac (FD) for degenerate carriers, and this transition completely changes the screening characteristics. The critical electron concentration n_{cr} depends upon temperature and is given by $n_{cr} = N_c\mathcal{F}_{\frac{1}{2}}(0)$, where N_c and $\mathcal{F}_{\frac{1}{1}}(\eta)$ are defined in Eq. (42). Finally and most importantly, impurity states are modified as carrier concentrations increases, mainly due to the static screening effect. This complexity alters the *conventional* characterization of ionized impurity scatterings and affects the modeling of mobility in doped semiconductors. In this research, only the contribution from ionized impurity scatterings is considered.

This research treats carrier scatterings due to ionized impurities by taking into full account both the FD statistics and self-consistent determination of the chemical potential which, in return, determines carrier concentrations and their derivatives with respect to the chemical potential. The ionized impurity scatterings are treated with the *relaxation time approximation*, but without using either the Brooks-Herring [88] or the Conwell-Weisskopf [89] approximation. The present theory ignores the formation of impurity bands, as stated in the previous chapter, and its influence on the static screening may be estimated as follows. First of all, the density of states (DOS) due to impurities does not change after metal-insulator transition. Instead, there is a gradual spread of DOS with energy centered around the single impurity value, which is equivalent to a system of distributed impurity levels. At low temperature, the screening increases appreciably and modifies the present results. Secondly, conduction by impurity states is negligible at high enough temperature compared to conduction by the bulk states because of their hopping nature. Finally, a large fraction of the impurity states are excited into the bulk states resulting from the reduction of donor levels due to increased static screening at high temperatures.

The present part of the research is organized as follows: First of all, the set of equations for determination of chemical potential in a homogeneous semiconductor are summarized. Then, the expression for mobility due to ionized impurity scatterings is deduced. Furthermore, the results from applying the theory to *n*-ZnSe are presented and compared to the experimental data [87]. Discussion follows up and finally conclusions are drawn. (In Appendix C, exposition of the generalized Debye theory and its applications are given.)

CHAPTER 14
THEORIES

Chemical Potential

Chemical potential is determined by thermodynamical equilibrium of a system. For homogeneous semiconductors, the condition for the equilibrium is reduced to charge neutrality among ionized impurities and charged carriers. A change in the chemical potential, in turn, affects carrier concentrations, dynamical parameters, such as scattering rates, and static parameters, such as dielectric constant. Table 7 lists the material parameters used in the present calculation for n-ZnSe. The bottom of the conduction band is used as the reference for the chemical potential, or $E_c(\Gamma) = 0$. Also, all other material parameters are positive and in their absolute values so that the bandgap E_g directly appears in the following formulas.

First of all, listed below are the three equations governing charge equilibriums, which hold for acceptors, donors, and total charge neutrality.

$$N_a = N_a^- + N_a^x \,, \tag{35}$$

$$N_d = N_d^+ + N_d^x \,, \tag{36}$$

$$N_a^- + n = N_d^+ + p \,, \tag{37}$$

where N_a, N_a^-, N_a^x, N_d, N_d^+, N_d^x, n, p are concentrations of acceptors, ionized acceptors, neutral acceptors, donors, ionized donors, neutral donors, electrons, and holes. Equilibrium equations (35–37) are self-evident. In this research, compensation ratio θ is defined as $\theta = N_a^- / N_d^+$.

Table 7: ZnSe Material Parameters Used in the Calculations of Part IV.

Parameter	Notation	Value	Reference
electron effective mass	m_e^*	0.17	[90]
hole effective mass	m_h^*	0.60	[91]
energy gap	E_g (eV)	2.70	[92]
relative dielectric constant	κ	9.20	[93]
donor level	E_d^0 (meV)	27.3[a]	
acceptor level	E_a^0 (meV)	96.4[b]	
acceptor hydrogenic radius	a_H^a (Å)	8.11[c]	
donor hydrogenic radius	a_H^d (Å)	28.6[d]	

[a] $E_d^0 = 13.6 m_e^* \kappa^{-2}$.
[b] $E_a^0 = 13.6 m_h^* \kappa^{-2}$.
[c] $a_H^a = .529\kappa/m_h^*$.
[d] $a_H^d = .529\kappa/m_e^*$.

Then, statistics for all the thermodynamically active parties in the system are considered. FD statistics for carriers are used in all parametric ranges. The expressions are listed below and are available in most solid state physics textbooks, such as Ashcroft and Mermin [94],

$$n = N_c \mathcal{F}_{\frac{1}{2}}(\eta)\,, \tag{38}$$

$$p = N_v \mathcal{F}_{\frac{1}{2}}(-\varepsilon_i - \eta)\,, \tag{39}$$

$$N_a^x = \frac{N_a}{1 + \frac{1}{2} e^{-\beta(E_a - E_g - E_f)}}\,, \tag{40}$$

$$N_d^x = \frac{N_d}{1 + \frac{1}{2} e^{-\beta(E_d + E_f)}}\,, \tag{41}$$

where

$$
\begin{aligned}
N_c &= 2\left(\frac{m_e^* m_e k_B T}{2\pi\hbar^2}\right)^{\frac{3}{2}} = 4.829 \times 10^{15} (T m_e^*)^{\frac{3}{2}} cm^{-3}\,, \\
N_v &= 2\left(\frac{m_h^* m_e k_B T}{2\pi\hbar^2}\right)^{\frac{3}{2}}\,, \\
\beta &= (k_B T)^{-1}, \qquad \eta = \beta E_f, \qquad \varepsilon_i = \beta E_g\,, \\
\mathcal{F}_{\frac{1}{2}}(\eta) &= \frac{2}{\sqrt{\pi}} \int_0^\infty d\varepsilon \, \frac{\varepsilon^{\frac{1}{2}}}{1 + \exp{(\varepsilon - \eta)}}\,,
\end{aligned}
\tag{42}
$$

T being the temperature and E_f being the Fermi energy.

In combination with Eqs. (35-41), the binding energy of a Hydrogen-like impurity is treated by including static screening using the generalized Debye theory, which is derived in Appendix C. To self-consistently solve the equations, the following procedure is performed. First of all, the Fermi energy E_f is determined by solving Eqs. (35-41) with the material parameters given in Table 7 and variables, *i.e.*, temperature T, donor concentration N_d, and acceptor concentration N_a, given. Then, the Debye screening length λ_D is determined from

$$
\lambda_D^{-2} = \frac{e^2}{\epsilon}\left(\left|\frac{\partial n}{\partial E_f}\right| + \left|\frac{\partial p}{\partial E_f}\right| + \left|\frac{\partial N_a^-}{\partial E_f}\right| + \left|\frac{\partial N_d^+}{\partial E_f}\right|\right). \tag{43}
$$

The new binding energies, E_d for donors and E_a for acceptors, are updated with the following relations [95]

$$
E_d = \begin{cases} E_d^0\left(1 - \frac{a_H^d}{2\lambda_D}\right)^2, & \lambda_D > \frac{a_H^d}{2} \\ 0, & otherwise \end{cases} \tag{44}
$$

$$
E_a = \begin{cases} E_a^0\left(1 - \frac{a_H^a}{2\lambda_D}\right)^2, & \lambda_D > \frac{a_H^a}{2} \\ 0, & otherwise \end{cases} \tag{45}
$$

where a_H^d and a_H^a are the Hydrogen radii for donors and acceptors, respectively. Equations (44–45) are the analytical solution for the binding energies of donor and acceptor states under the Hulthén potential, which is an excellent approximation to the screened Coulomb potential. So, the Eqs. (35-41) are solved self-consistently with static screening included until the binding energies converge.

Electronic Mobility due to Ionized Impurity Scatterings [96]

After the chemical potential is determined self-consistently, the screening length under the generalized Debye theory is given by Eq. (43). The mobility due to ionized impurity scatterings is then computed as described below, including the static screening effect on the scattering potential of the ionized impurities from other charged entities.

In order to obtain the electronic mobility due to ionized impurity scatterings, the BKE is solved under the *relaxation time approximation*. As generally known, rare analytical solutions are found for BKE [37]. It is worth mentioning that when dealing with polar LO phonon scatterings at low temperature, which are inelastic, the *relaxation time approximation* is invalid. A variational method may be applied to compute transport properties [49]. For materials where elastic scatterings dominates, the *relaxation time approximation* can be used for calculations of transport parameters. As for ionized impurity scatterings, the scattering events are elastic, so use of the *relaxation time approximation* is allowed. In order to compute transport coefficients, it is needed to find the *relaxation time*, which is directly related to the scattering rates for different elastic mechanisms.

For *n*-type ZnSe, only electronic scatterings within the conduction band need to be considered, which means both minority carrier and impurity conductions are ignored. The scattering rate, $W\left(\vec{k}, \vec{k'}\right)$, of an electron being scattered from initial state $|c\vec{k}>$ to final state $|c\vec{k}'>$ induced by interaction $U_{int}(\vec{r})$ can be obtained using the Fermi's golden rule,

$$\begin{aligned} W\left(\vec{k},\vec{k}'\right) &= \frac{2\pi}{\hbar}\left|H_{\vec{k}\vec{k}'}\right|^2\delta\left(E_{\vec{k}}-E_{\vec{k}'}\right), \\ H_{\vec{k}\vec{k}'} &= \int d^3r\,\psi^*_{c\vec{k}'}(\vec{r})U_{int}(\vec{r})\psi_{c\vec{k}}(\vec{r}), \end{aligned} \tag{46}$$

where $\psi_{c\vec{k}}(\vec{r})$ is the Bloch wavefunction for a conduction electron in $\vec{k}$ state,

$$\begin{aligned} \psi_{c\vec{k}}(\vec{r}) &= <\vec{r}|c\vec{k}> \\ &= \frac{1}{\sqrt{V}}e^{i\vec{k}\cdot\vec{r}}u_{c\vec{k}}(\vec{r}), \end{aligned} \tag{47}$$

V is the crystal volume. Parabolicity is assumed for $E_{\vec{k}}$, and intervalley scatterings are not considered. This is reasonable owing to large energy separation and weak interaction at large wavevectors. Also neglected is the periodic part of the Bloch wavefunctions, which is equivalent to the assumption that the overlap integral between the periodic parts of the initial and final states is unity. For ionized impurity scatterings, the interaction $U_{int}(\vec{r}) = eV(\vec{r})$, where $V(\vec{r})$ is given as in Eq. (81) with $Z_i\bar{e}_i$ being the amount of charge on an ionized impurity, and the interaction matrix element is computed to be

$$H_{\vec{k}\vec{k}'} = \frac{A}{\sin^2\left(\frac{\theta}{2}\right)+\alpha^{-2}}, \tag{48}$$

where $\theta = \cos^{-1}\left(\hat{k}\cdot\hat{k}'\right)$ is the angle between wavevectors $\vec{k}$ and $\vec{k}'$, and

$$A = \frac{Z_i\bar{e}_i e}{4\epsilon V k^2}, \qquad \alpha = 2k\lambda_D. \tag{49}$$

Then, the *relaxation time*, or the linear momentum *relaxation time*, which is favored by large angle scatterings, is computed as

$$\frac{1}{\tau} = \frac{V}{(2\pi)^3}\int d^3k'\,W\left(\vec{k},\vec{k}'\right)(1-\cos\theta). \tag{50}$$

Since electrons follow FD statistics and may have a broad energy distribution, the above *relaxation time* normally depends upon the energy of the scattered electron. A proper averaging procedure[1] is therefore needed for τ [97]. It is shown that the appropriate procedure is to average over τ weighted with the energy of the scattered electron,

$$<<\tau>>=\frac{<E\tau>}{<E>}\,, \tag{51}$$

where

$$\begin{aligned} <E\tau> &= \int dE\, g(E) f_{FD}(E)\, E\tau\,, \\ <E> &= \int dE\, g(E) f_{FD}(E)\, E\,, \\ f_{FD}(E) &= \frac{1}{\exp\left(\frac{E-E_f}{k_B T}\right)+1} \end{aligned} \tag{52}$$

where $g(E)$ is the density of states and proportional to $\sqrt{E}$ for a parabolic band.

For screened Coulomb potential of ionized impurities of type i with density n_i, an analytical solution can be found for $\frac{1}{\tau_i}$, assuming independent scatterings from different ionized impurities, and the result is

$$\frac{1}{\tau_i}=n_i\left(\frac{Z_i e_{\bar{i}} e}{\epsilon}\right)^2 \frac{1}{16\pi\sqrt{2m_e^* m_e}} \frac{\ln\left(1+\alpha^2\right)-\frac{\alpha^2}{1+\alpha^2}}{E^{\frac{3}{2}}}\,, \tag{53}$$

which is exactly the same as derived by classical treatment. Adopting the $\sum\limits_i \frac{1}{\tau_i}$ additive scheme for the effective $\frac{1}{\tau}$, the *relaxation time* is found to be

$$\tau=16\pi\sqrt{2m_e^* m_e}\,\frac{\epsilon^2}{e^4\sum\limits_i n_i Z_i^2}\,\frac{E^{\frac{3}{2}}}{\ln\left(1+\alpha^2\right)-\frac{\alpha^2}{1+\alpha^2}} \tag{54}$$

where the summation over i accounts for different types of ionized impurities and it is assumed that all Z_i equals unity. Finally the averaged *relaxation time* is found by using Eq. (51) and the associated drift mobility is given by

$$\mu_d=\frac{e}{m_e^* m_e}<<\tau>>\,. \tag{55}$$

---

[1] It is assumed that the averaging procedure can be extended to quantum systems under low electric field.

The difference between the drift and Hall mobility is studied so as to understand the effect of statistics on the two mobilities. For the known $E^{\frac{3}{2}}$ dependence of τ, the two mobilities, in MB distribution, differ by a constant ratio of *1.93* [97]. The Hall mobility is derived, assuming that electric and magnetic fields perturb the distribution function independently so that their contributions are additive to the unperturbed distribution function, as follows

$$\mu_H = \frac{<<\tau^2>>}{<<\tau>>^2}\mu_d \,. \tag{56}$$

For FD distribution, the ratio of *1.93* is changed because of the statistical degeneracy of the system. In most cases this ratio tends to be close to unity, which is verified in this research.

CHAPTER 15
RESULTS AND ANALYSIS

Three parametric series have been investigated: (A) fixing the donor concentration N_d and increasing the acceptor N_a till $0.5N_d$ to study the effect of compensation; (B) increasing N_d with N_a set to zero; (C) increasing both concentrations with $N_d = 2N_a$. The temperature range is the same for all series but impurity concentrations vary as above. Series A is studied so as to understand the transition from Series B to Series C. Series C is for compensated systems and Series B is for uncompensated systems. In order to avoid the impurity band issue, N_d is chosen to be $10^{17} cm^{-3}$ for Series A, as compared to the critical value given in Eq. (34'). The experimental variable range is qualitatively covered by Series C. The *parametric space* is defined in this study as the parameter ranges covered by the three series. Theoretical results are compared with the experiments [87] in this chapter following their own exposition. Table 8 lists the parameters used in this study.

There are two major physical processes which are instrumental in understanding all the results in this research: (1) compensation by acceptors and (2) thermal ionization[1] of donors. The first process dominates at low temperature and the second one becomes important and dominant when the donor level is reduced small enough to generate enough free electrons in the conduction band even at low temperature. Static screening is enhanced due to compensation and strongly affects the second process. In n-ZnSe, acceptors play no direct role in static screening except compensation and scattering. Because it is assumed that acceptors are fully ionized, there is negligible hole concentration in the system as well. Therefore, donors and electrons are the focuses of discussion as follows

---

[1] Thermal excitation is used when referring to electrons.

Table 8: Input Parameters Used in the Calculations of Part IV.

Series Parameter		Values							
T (K)		5	8	15	17.5	20	22.5	25	28
		32.5	38	43	50	63.5	70	85	100
		125	150	200	250	300			
A	N_d (cm^{-3})	10^{17}							
	N_a (cm^{-3})	10^{0}	10^{1}	10^{2}	10^{3}	10^{4}	10^{5}	10^{6}	10^{7}
		10^{8}	10^{9}	10^{10}	10^{11}	10^{12}	2.5×10^{12}	5×10^{12}	10^{13}
		2.5×10^{13}	5×10^{13}	10^{14}	2.5×10^{14}	5×10^{14}	10^{15}	2.5×10^{15}	5×10^{15}
		10^{16}	2.5×10^{16}	5×10^{16}					
B	N_d (cm^{-3})	10^{13}	10^{14}	10^{15}	10^{16}	10^{17}	10^{18}	10^{19}	3×10^{19}
	N_a (cm^{-3})	0.0							
C	N_d (cm^{-3})	10^{13}	10^{14}	10^{15}	10^{16}	10^{17}	10^{18}	10^{19}	3×10^{19}
	N_a (cm^{-3})	5×10^{12}	5×10^{13}	5×10^{14}	5×10^{15}	5×10^{16}	5×10^{17}	5×10^{18}	1.5×10^{19}

Series A

Series A is designed to understand the interplay of both major processes and the interplay of screenings by ionized donors and electrons. It is interesting to find that the static screening effect induces a first-order phase transition with temperature for uncompensated systems when the donor concentration is higher than $10^{17} cm^{-3}$ and the transition disappears at high compensation.

Shown in Fig. 21 is the derivative of the ionized donor concentration with respect to the chemical potential versus temperature. The derivative quantitatively indicates the screening capability of donors, as exhibited in Eq. (43). It is helpful to understand the result by looking at the uncompensated system at low temperature. Firstly, $N_d^+ = n$ holds approximately. Also, it is found from Eq. (92) that $|\frac{\partial N_d^+}{\partial E_f}| \approx \beta n$ since ionization ratio $\frac{N_d^+}{N_d}$ is low. Furthermore, the electron concentration is given by

$$n = N_c e^{\beta E_f} , \tag{57}$$

where all the quantities are defined in Eq. (38–41), and E_f, the Fermi energy, can be assumed to be $-13\,meV$ because it is usually pinned at the middle between the donor level and the bottom of the conduction band. So, it is possible to estimate the Debye length at *25 K* and the reduction of the donor level as a first-order approximation. The Debye length is about *300 Å* and the reduction of the donor level is about *10* percent. Therefore, static screening due to thermal excitation influences the system critically, given the highly nonlinear, self-consistent description of the system. The transition at *26.5 K* is a near-metal-insulator transition, as checked with the following results of the chemical potential (see Fig. 26) and electron concentration (see Fig. 27), and it is because of the static screening effect due to thermal excitation. Discussion of the nature of the transition at *26.5 K* will be attempted in the following chapter. For a compensated system, as acceptors are added to the system, electrons in donor states will transfer to the lower energy states, or acceptor states. As a result, the acceptors are fully ionized presumably and donor states are partially filled so that they will participate in the screening process. At zero temperature, $N_d^+ = N_a$ so that $|\frac{\partial N_d^+}{\partial E_f}| = \beta\frac{N_a(N_d - N_a)}{N_d}$, according to Eq. (92), is finite, which means finite screening capability. Compensation has the best effect on screening when half of the donors are ionized according to Eq. (92). The effect of the temperature on screening is twofold: thermally generating electrons in the conduction band and reducing screening through the β factor, as appeared in Eqs. (88) and (92). At low temperature and low compensation, thermal excitation is more important than the β factor effect, as analyzed above. When temperature rises, the static screening effect is gradually reduced due to the β factor.

The result for the derivative of the free electron concentration with respect to the chemical potential, as shown in Fig. 22, can be understood along the same line. A twist, however, is the generation of electrons in the conduction band at low temperature. Due to the fact that the donor concentration, N_d, is high enough, $10^{17}cm^{-3}$, a MI transition is possible for a highly compensated system. By MI transition it is meant that the chemical potential falls into the conduction band since the bottom of the conduction band defines the mobility edge in the present theory. When a MI transition occurs, donor impurities are ionized thermally and part of their electrons become free carriers in the conduction band. Further discussion about this simple picture of MI transition follows in the next chapter. So, due to the MI transition in a highly compensated system, electrons appear in the conduction band at low temperature. And, the system exhibits the behavior of degenerate electrons, which means finite screening capability at low temperature, according to $|\frac{\partial n}{\partial E_f}| = \beta n$ and a constant n, and the β factor dominates. However, for systems of low compensation at low temperature, free electrons are thermally generated so that n follows Eq. (57) and the screening capability grows exponentially before the MI phase transition.

It is straight-forward to deduce, from the generalized Debye theory, that under first-

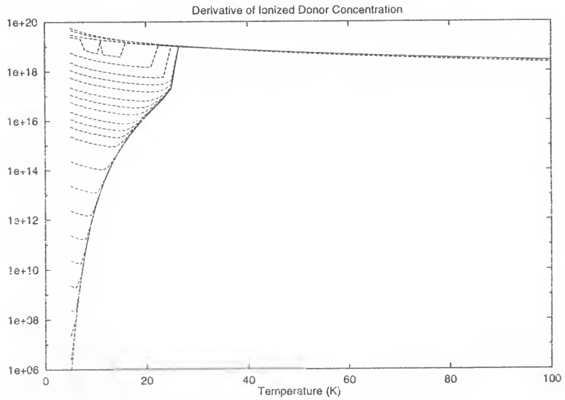

Figure 21: Derivative of the ionized donor concentration with respect to the chemical potential for Series A. It indicates the screening capability of the ionized donors. At low temperature, compensation increases the capability as the filled states become partially occupied. Sharp transition occurs at *26.5 K*. At high temperature, the β factor kicks in and reduces the capability

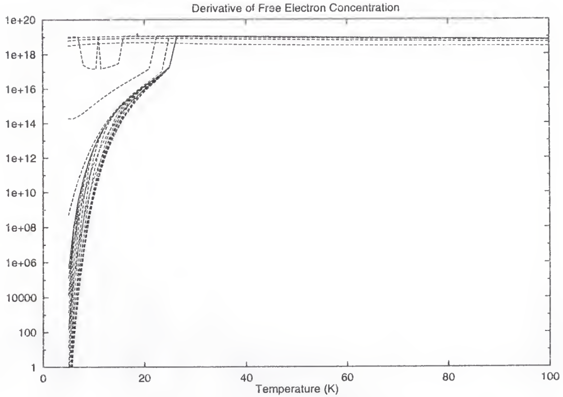

Figure 22: Derivative of the free electron concentration with respect to the chemical potential for Series A. At low temperature, thermal excitation increases the screening capability of electrons for systems of low compensation. For highly compensated systems, due to MI transition, they show the behavior of degenerate electrons. The β factor affects the screening in all temperature range but dominates at high temperature.

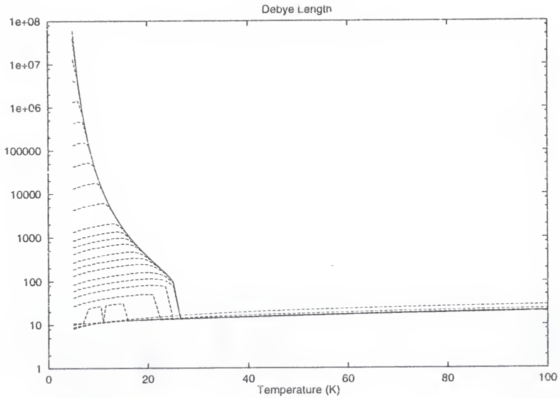

Figure 23: Debye Length (in Å) versus temperature for Series A. At the *critical temperature* of *26.5 K*, MI transition due to static screening occurs at low compensation. The transition temperature decreases with the acceptor concentration and vanishes above the *critical acceptor concentration* where the system becomes metallic. Below the *critical temperature*, screening effect is predominated by compensation. The β factor effect weakly increases the Debye length in non-transitional regime.

order approximation fully occupied or unoccupied bands does not screen statically. The Debye length of a n-ZnSe system indicates, inversely, its screening capability. As clearly shown in Fig. 23, when the system has no acceptors, the Debye length goes to infinity at low temperature. When acceptors are added to the uncompensated n-ZnSe bulk material, according to the present theory, all of them compensate donors so that donor states become susceptible to perturbation of external potential. As a result, the Debye length begins to decrease and reaches minimum at $5 \times 10^{15} cm^{-3}$ of the acceptor concentration. Above this acceptor concentration, the system is metallic and the screening is weakly temperature-dependent thanks to the β factor effect. This critical concentration is defined as the *critical acceptor concentration* for the convenience of later discussion. As temperature increases for uncompensated systems, the Debye length decreases and makes a transition at *26.5 K* when thermal ionization of the donor impurities critically enhances the screening capability of donor impurities and electrons. This transition temperature is defined as the *critical temperature* for later discussion although it is not well-defined at high acceptor concentration. Above the *critical temperature*, the Debye length increases slightly because of the β factor effect. Over-doping with acceptors beyond the critical acceptor concentration only affect the screening capability of the system barely, which is reasonable because of the maximum in the screening capability approximately at half compensation.

The ionized donor concentration is important in determining the mobilities of free carriers at low temperature and it is affected by compensation and thermal excitation. In the present theory, all acceptors are compensated, or ionized. As a consequence, addition of acceptors enhances the screening capability of donors, which in return reduces

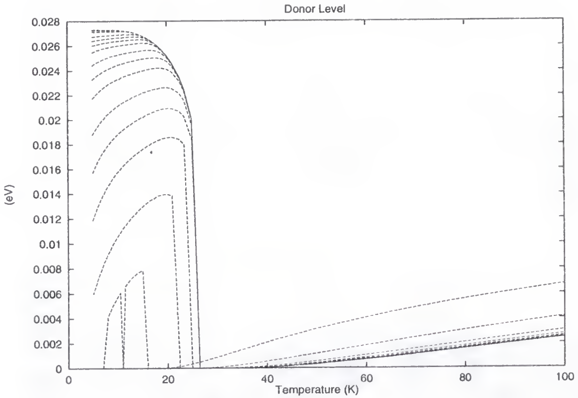

Figure 24: Binding energy of donors versus temperature for Series A. Below the *critical temperature*, donor level is reduced as acceptor concentration increases. Away from the transition region, it increases due to the β factor effect.

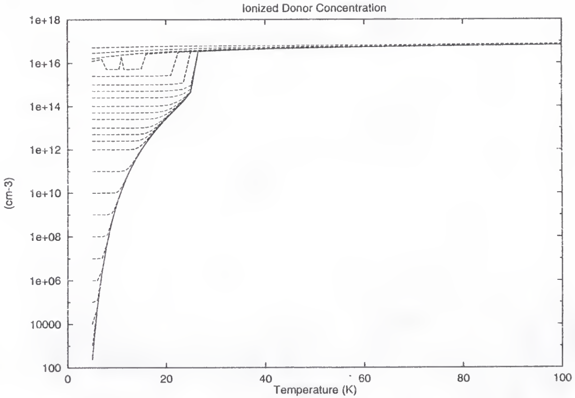

Figure 25: Ionized donor concentration versus temperature for Series A. At low compensation, thermal ionization of donors increases the ionized population exponentially. Increase in acceptor concentration accordingly creates the same amount of ionized donors at low temperature. Above the *critical acceptor concentration*, ionized donor concentration increases weakly with temperature. There is slight change in the ionized donor concentration above the *critical temperature*.

the binding energy of donors. As clearly indicated in Fig. 24, increase of acceptor concentration reduces the binding energy of donors appreciably from their initial value $E_d^0 = 27.3\,meV$, as given in Table 7. The result in Fig. 24 can be characterized by two values as before: the *critical acceptor concentration* and the *critical temperature*. Below the *critical temperature*, donor level is reduced with acceptor concentration because of the compensation effect. The β factor effect allows the donor level to recover appreciably due to weakening in the screening capability of the system. Interestingly, the donor level can recover somewhat from the near-MI transition above the *critical temperature*. More surprisingly, the data show re-entrant behavior with temperature at the acceptor concentration of $5 \times 10^{15} cm^{-3}$. On the other hand, the ionized donor concentration basically follows the Debye length in behavior. Above the *critical acceptor concentration*, it increases slightly with temperature due to thermal ionization. There is a drastic increase in the ionized donor concentration in the transition region.

Due to the reduction of donor levels by screening effect, the chemical potential shows a sign of a metal-insulator phase transition at a *critical temperature* of *26.5 K* for uncompensated systems ($E_f = -0.094\,meV$ at *26.5 K*), but retreats gradually because of lack of screening capability to sustain the transition at the donor concentration of $10^{17} cm^{-3}$ for Series A. Above the *critical temperature*, the chemical potential begins to exhibit intrinsic behavior of the bulk material and decreases towards the middle of the bandgap. Thermodynamically, it is easy to see that below the *critical temperature* donor level is the dominant energy scale but static screening effect strongly modifies it so as to cause the system to show sign of phase transition. Above the *critical temperature*, the bandgap of the host material kicks in as the smaller energy scale, *i.e.*, the donor

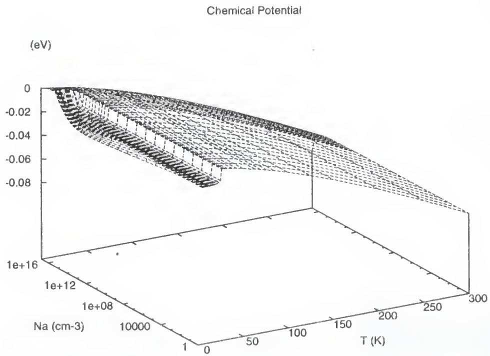

Figure 26: Chemical potential as a function of temperature for Series A. MI transition occurs at a *critical acceptor concentration* of $5 \times 10^{15} cm^{-3}$ for compensated systems or at a *critical temperature* of *26.5 K* for uncompensated systems. Below the *critical temperature* and the *critical acceptor concentration*, chemical potential is frozen around *-13 meV*. At high temperature, the chemical potential decreases towards the middle of the bandgap.

level, is submerged by thermal fluctuations. Along the same line as before, the *critical acceptor concentration* distinctively classifies the result in Fig. 26 into two regions: above the critical concentration, the system is metallic ($E_f = 0.6\, meV$ at *6 K* at the critical concentration) and thermal excitation drives the chemical potential towards the middle of the bandgap; below the critical concentration, the chemical potential is pinned around half of the donor level at low temperature and then the chemical potential experiences a near-MI transition because of the decrease of the donor energy due to screening effect.

Free electrons in the conduction band are generated by thermally ionizing donors. So, the free electron population reflects the thermodynamical activity of donor impurities. At low acceptor concentration, as shown in Fig. 27, there is an abrupt change in the free electron density at *26.5 K* and the electron density is altered by about three orders of magnitude. This is a clear manifestation of the near-MI transition due to the static screening effect. Below the *critical temperature*, the density follows the behavior of thermal excitation over a single energy gap, which shows a linear dependence in the $\log n$-$\frac{1}{T}$ plot. This behavior is known as the freeze-out behavior. Saturation is nearly reached above the critical temperature where the electron density is almost independent of temperature. As acceptor density increases, the critical temperature is reduced gradually until a MI transition is reached. Around this transition, re-entrant behavior has been found, which presumably has to do with the highly nonlinearity near the transition region. In the metallic regime, the electron density increases gradually with temperature though it can become twice as much from *77 K* to *300 K*.

Drift mobility and Hall mobility limits how fast a semiconductor can operate. When semiconductors are doped, it is desired to have as high a mobility as possible. At low

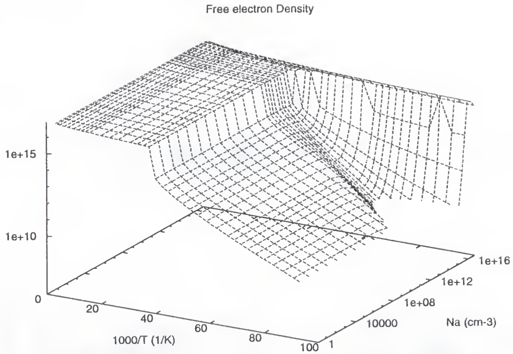

Figure 27: Free electron concentration as a function of temperature and acceptor concentration for Series A. The concentration tends to saturation above the *critical temperature* and *critical acceptor concentration*. Freeze-out occurs at low acceptor concentration, but the slope varies with acceptor concentration.

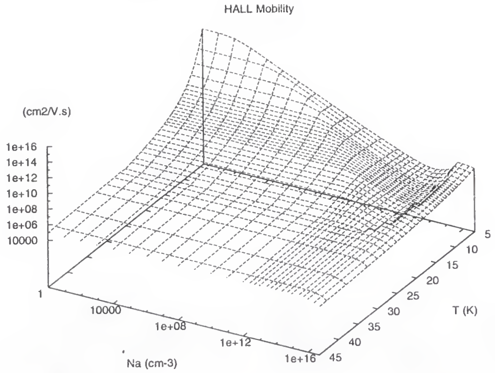

Figure 28: Dependence of Hall mobility on temperature and acceptor concentration for Series A. The mobility decreases drastically with temperature in correlation with the ionized impurity concentration below the *critical temperature* and the *critical acceptor concentration* and changes weakly in other regions.

temperature, carrier scatterings with charged impurities essentially determine the mobilities, though scatterings with phonons dominate at room temperature. Therefore, result for mobilities below *50 K* is reported. Figure 28 shows the Hall mobility as a function of temperature and acceptor concentration and the drift mobility is characteristically similar. Below the *critical acceptor concentration* and the *critical temperature*, the Hall mobility drops about ten orders of magnitude, but changes barely in other regions. This result is in sharp contrast with predictions by the well-known CW [89, 96] and BH [88, 96] theories. Both theories predict no drastic change in the mobilities. The difference results, obviously, from whether the static screening effect and the chemical potential are treated self-consistently. According to Eq. (54-55), drift mobility depends upon ionized impurity concentrations inversely and screening weakly. Thus, in regions where ionized impurity concentrations vary rapidly, the mobility is controlled mainly by ionized impurity concentrations, which is supported by Fig. 25 in the low temperature and low acceptor concentration region. In other regions where ionized impurity concentrations vary inappreciably, screening effect will play a major role, though it does not affect the mobilities strongly.

As a note, conductivity or resistivity of the doped material, in case of doping a semiconductor to make ohmic contact, is the critical parameter and the conductivity by electrons depends upon the product of the electron concentration and the drift mobility.

Series B and C

As clearly exhibited in Figs. 29-37, highly compensated and uncompensated semiconductors show characteristically different behaviors owing to enhanced screening effect in the compensated materials (Series C) by compensation. As suggested in Eq. (77), any deviation from full or zero occupation of an energy state will enhance its screening capability until half occupancy. For n-type semiconductors, the addition of acceptors is instrumental to this screening-capability-enhancing process for donors. This process makes a fundamental difference in the two series at low temperature. However, as temperature goes up, thermal ionization of donor states will smear out this difference, as already exhibited in the results for Series A and shown in the following results.

At low temperature, donor ionization is determined by compensation in Series C but by thermal ionization in Series B. The ionized donor concentration equals the acceptor concentration at zero temperature for Series C when the donor concentration is low. However, when the donor concentration is over $10^{17} cm^{-3}$, the system becomes metallic and the ionized donor concentration saturates at all temperature. The ionized donor concentration does not change much in magnitude in Series C since half of the donors have already been ionized, due to compensation, even at low donor concentration. As temperature increases, the transitional behavior in donor ionization in Series B sets in thanks to thermal ionization and the *critical temperature* decreases with donor concentration because screening capability gets stronger since the capability is proportional to the donor concentration, as exhibited in Fig. 30. The MI transition with temperature in Series B is well-defined above $10^{17} cm^{-3}$ of donor concentration, but in Series C no such abrupt transitions are exhibited with temperature since compensation dominates similar to Series A in the previous section. Above the *critical temperature*, as shown in Fig. 29, ionized donor concentration is almost the same for the two series and increases with donor concentration. For both series, donor ionization by thermal excitation tends to saturate towards high temperature for non-metallic systems, as expected.

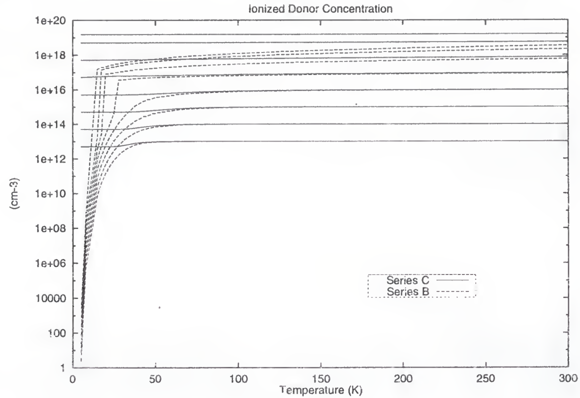

Figure 29: Ionized donor concentration versus temperature for Series B and C. The two series differ around and below the *critical temperature*. At high temperature, the ionized population tends to saturate for the two series. Thermal ionization dominates at low temperature in Series B and compensation dominates in Series C. Metallic systems saturates at all temperature.

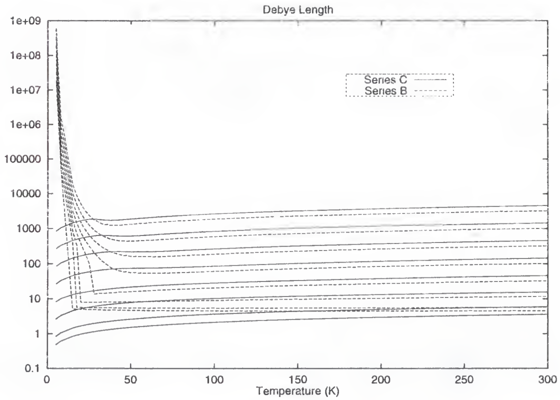

Figure 30: Debye length versus temperature for Series B and C. The length decreases with donor concentration for both series. For Series C, the Debye length increases with temperature. For Series B, it decreases below the *critical temperature* and increases above the temperature.

As shown in Fig. 30, at low donor concentration, for both series, the screening effect is weak as the Debye length is over *1,000 Å*. As donor concentration increases, the screening capability increases roughly according to $N_d^{-\frac{1}{2}}$ for Series C, and this behavior holds for Series B above the *critical temperature*. This behavior can be seen from Eq. 89 and the fact that $n \propto N_d$ when N_d^+ varies slowly. In all temperature ranges, for Series C, the temperature dependence is roughly $\sqrt{T}$, as predicted by the β factor effect. For Series B, the temperature dependence features a critical behavior at the transition and weak dependence above it at high donor concentrations.

As shown in Fig. 31, the dependence of the Debye length on carrier concentration for Series B does go roughly as the inverse-square-root prediction for classical electron gas below $10^{18} cm^{-3}$ of the electron density. The reason is because that ionized donors contribute to screening, according to Figs. 21 and 22, with the same dependence. Therefore, the dependence follows the prediction for classical electron gas at low electron density. The deviation at high electron density in Series B is due to the β factor effect above the transition region. The Debye length for Series C is weakly dependent on the electron concentration for systems with low donor concentration and the reason is because compensation dominates over thermal excitation of electrons in contributing to the screening capability. The deviation at high electron density in this series is due to the same reason as in Series B. However, positive dependence of a power of .33 at high concentration is shown and explanation is the β factor effect because the Debye length is reduced by the effect while the electron concentration does not change noticeably in these metallic systems, as shown in Fig. 34.

Donor level directly relates to the screening capability of the system according to

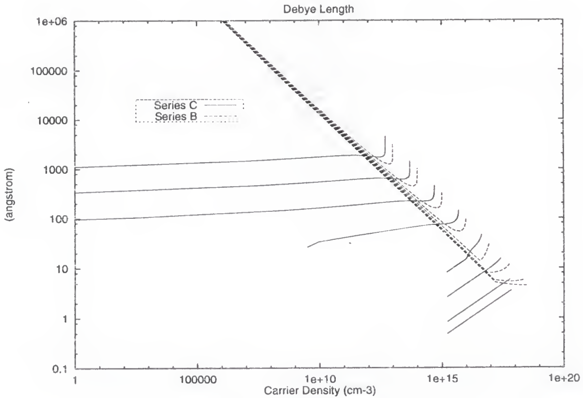

Figure 31: Debye length versus electron density for Series B and C. Series B follows power law dependence on density with a power of $-.42$ while Series C shows diverse dependence from weak at low donor concentration to power law dependence with a power of .33 at high concentration.

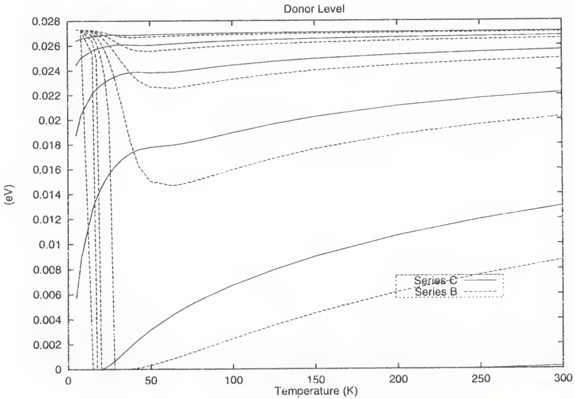

Figure 32: Donor level versus temperature for Series B and C. Donor level is reduced by screening effect. In both series, donor level decreases with donor concentration. In Series B, donor level is drastically shrinked below *26.5 K* and becomes zero above $10^{17} cm^{-3}$ of donor concentration. It increases above the transition region. For Series C, donor level reduces with temperature.

Eq. (44–45), as reiterated below,

$$E_d = \begin{cases} E_d^{\mathrm{C}}\left(1 - \frac{a_H^d}{2\lambda_D}\right)^2, & \lambda_D > \frac{a_H^d}{2} \\ 0, & otherwise\,. \end{cases} \tag{58}$$

As estimated in Table 7, the hydrogenic radius, a_H^d, of a donor in ZnSe is *28.6* Å. The present theory assumes that E_d is reduced to zero if the Debye length is shorter than half of the donor hydrogenic radius. As shown in Fig. 32, donor level shrinks in Series B at low temperature and reaches zero when donor concentration exceeds $10^{17} cm^{-3}$. Around this donor concentration, the donor level tends to recover as the temperature increases, which is because the β factor effect decreases the screening capability of the system. The donor level for Series C increases smoothly with temperature and decreases with donor concentration. It follows the behavior of the Debye length: (1) the screening increases with donor concentration; (2) at low donor concentration the thermal excitation contributes more appreciably to screening than at high donor concentration, due to compensation; (3) the donor level shrinks to zero above $10^{18} cm^{-3}$ of donor concentration; (4) the β factor effect reduces screening with temperature.

The chemical potential defines the state of the system: at low temperature, it becomes positive at MI transition; at high temperature, because the intrinsic behavior sets in, it reduces towards the middle of the bandgap even though the system is still metallic, as indicated by the free electron density! The chemical potential behaves quite differently for Series B and C as shown in Fig. 33 The main difference exists in the donor concentration dependence, which is a reflection of the acceptor concentration in the series, as given in Table 8. Series B displays MI transitional behavior above donor concentration of $10^{17} cm^{-3}$ with temperature, induced by the screening effect due to thermal excitation, and the *critical temperature* decreases with donor concentration because of increase in

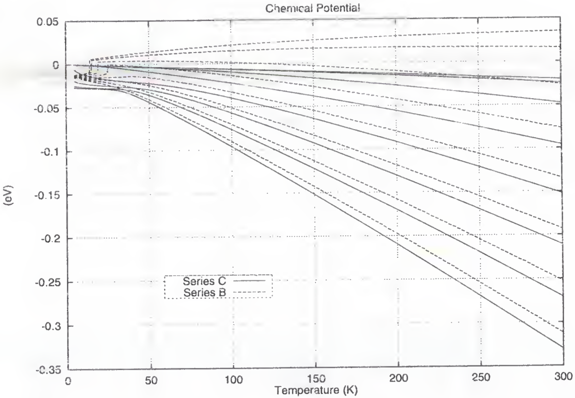

Figure 33: Chemical potential versus temperature for Series B and C. Series B shows MI transition above $10^{17}cm^{-3}$ of donor concentration and the *critical temperature* reduces with donor concentration. Series C features gradual increase of chemical potential and MI transition occurs above $10^{17}cm^{-3}$ of donor concentration.

the screening capability of the system. On the other hand, the chemical potential in Series C gradually increases and finally merges into the conduction band at low temperature. This leads to a MI transition. The *critical donor concentration* is about $10^{17} cm^{-3}$, roughly comparable with the critical donor concentration as predicted in Eq. (34) for the Anderson MI transition. The implication of this coincidence will be discussed in the following chapter. In comparison, Series C has a weaker temperature dependence than Series B because of compensation (recall that the acceptor concentration is zero in Series B and half of the donor concentration in Series C). At high temperature, the intrinsic behavior of the bulk semiconductor dominates, as the valence bands pull the chemical potential down. Generally, the chemical potential is lower in Series C than in Series B, as acceptors pull the chemical potential down.

The electron concentration measures the doping efficiency of a doped semiconductor and affects the conductivity of the material. For donor-only semiconductors of low donor concentration, the well-understood behavior of the electron concentration features three regimes in temperature: (1) thermal excitation over donor level at low temperature, (2) saturation of electron concentration at temperature comparable to the donor level and (3) thermal excitation over bandgap at temperature comparable to the bandgap. The result for Series B exhibits this typical behavior at low donor concentration. Obviously, room temperature, *25.9 meV*, is far too low, compared to *2.7 eV*, the bandgap of ZnSe, to see the high temperature regime. The slope in the $\log n$-$\frac{1}{T}$ plot for the freeze-out regime is measured at *-0.1462 K*, which yield a value of *25.2 meV* for E_d according to $n \propto \exp\left(-\frac{E_d}{2k_BT}\right)$. The MI transition with temperature takes place above a donor concentration of $10^{17} cm^{-3}$. On the other hand, Series C shows a transitional behavior

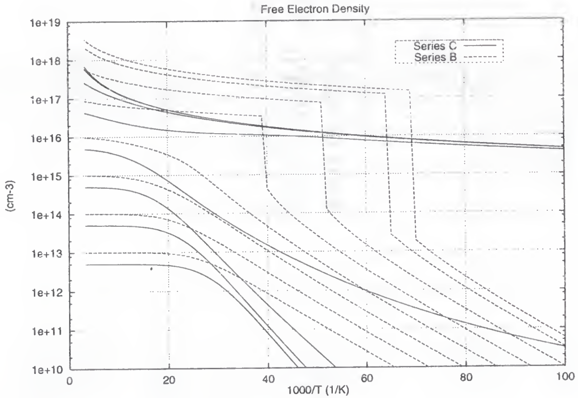

Figure 34: Electron concentration versus temperature for Series B and C. Generally, electron density in Series C is an order of magnitude lower than in Series B except for metallic systems below the *critical temperature*. Non-metallic systems show freeze-out and saturation regimes as normal, while temperature dependence differs in the freeze-out regime between the two series. Series C begins deviating from normal at a donor concentration of $10^{16} cm^{-3}$. Electron density increases after MI transition for both series.

at a donor concentration of $10^{17} cm^{-3}$. In addition, Series B always generates an order of magnitude more free carriers with the same donor concentration than Series C in the metallic region. Therefore the doping efficiency for Series B is higher than for Series C.

The Hall mobility is another important property, other than free electron concentration, that affects the conductivity of a doped semiconductor. Figure 35 shows that Hall mobility for Series B and C differs drastically below the *critical temperature*. The ionized impurity population increases from zero in Series B and ionized donors and acceptors exist in Series C even at zero temperature, thanks to compensation. In Series B, below the *critical temperature*, mobility drops exponentially with temperature, due to exponential increase in ionized donor concentration. This decrease slows down above the *critical temperature* in the metallic phase because of the strong screening. In Series C, the mobility increases at low donor concentration but decreases at high donor concentration. A reversal occurs at $10^{16} cm^{-3}$. Equations (54-55) tell that mobility depends inversely upon ionized impurity concentration and weakly upon the screening, if the screening effect behaves smoothly, as in Series C. In order to analyze the temperature dependence of the mobility, it is necessary to look at Eq. (54-55) carefully. The screening effect is weak when donor concentration is low. Owing to compensation, the ionized impurity concentration does not change much, as shown in Fig. 29, so that screening effect directly influences mobility. At low temperature the *relaxation time*, according to Eq. (54), is proportional to $E^{\frac{3}{2}}$. Since the screening effect is weak, the mobility increases with temperature, as the classical electron gas has $< E >= \frac{3}{2} k_B T$. On the contrary, at high donor concentration and low temperature, the screening effect is strong and the α factor in Eq. (54) gets small ($\alpha = 0.33$ if $\lambda_D = \frac{a_H^d}{2}$ and k is estimated from classical electron

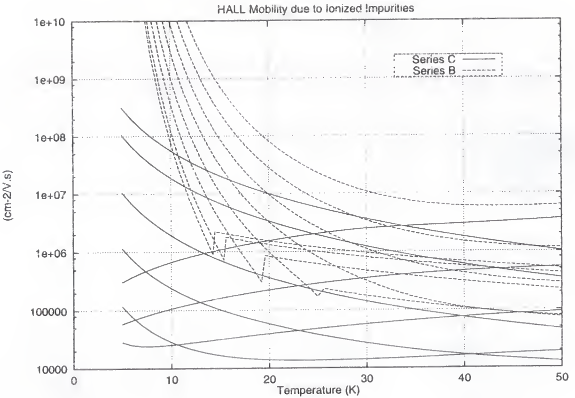

Figure 35: Hall mobility versus temperature for Series B and C. In Series C, mobility decreases with temperature above donor concentration of $10^{16} cm^{-3}$ and increases below that concentration. In Series B, mobility reduces with temperature faster than in Series C and MI transition slows the reduction.

gas with $T = 25\,K$) so the energy dependence of the *relaxation time* changes to $E^{-\frac{1}{2}}$ (an expansion in α produces an E^2 term in the denominator in Eq. (54).), which means that mobility decreases with temperature instead.

The Hall mobility is not an explicit function of the electron density in the present theory (since carrier-carrier scattering is not included) and is shown in Fig. 36. Two regimes can be classified for both series: (1) the low electron density regime and (2) the high electron density regime. At low electron density, Series B can be characterized by a well-defined power law behavior with a power of $-.89$, and above the MI transition, a different power of approximate -1.6 can be used to describe the relation. Series C varies insensitively with carrier concentration at low electron density but converges to a power law behavior after the MI transition.

The ratio of the Hall mobility to the drift mobility indicates the statistics of free carriers. For a MB distribution, various theories [96] predict approximately *1.9* for the ratio, and for FD distribution, it is predicted to be about unity. As shown in Fig. 37, the ratio is bounded between roughly *1.0* and *1.9*. It basically follows the variation of the donor level shown in Fig. 32. At low donor concentration, the two series converges to the MB value, and to the FD value at high donor concentration except for Series B at low temperature. At low temperature, the ratio approaches the classical limit of 1.9 in Series B, but there is no convergence in Series C and the ratio depends upon details of the static screening effect. A donor concentration of $10^{17}cm^{-3}$ is the critical value where systems begin to fall into different statistical limit. For n-ZnSe, the degree of degeneracy of a system must be considered, following Ruda [49]. A critical electron

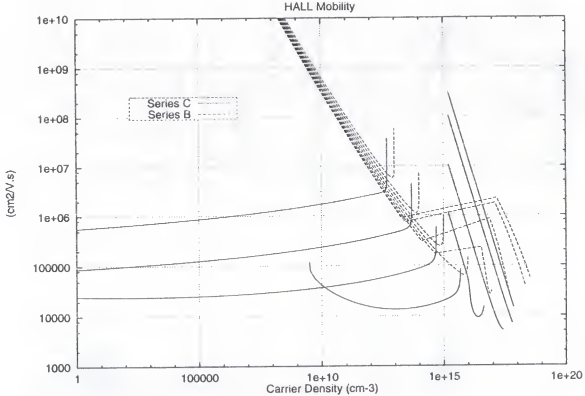

Figure 36: Hall mobility versus electron density for Series B and C. At high density, two series follow nearly the same power law with a power of about −1.6 for Series C. At low density, Series B follows power law with a power of −.89 while Series C changes insensitively with electron density.

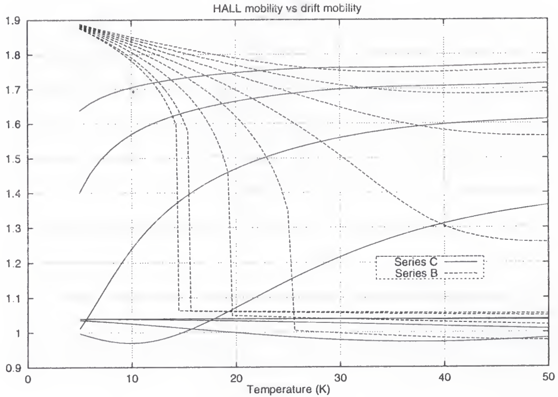

Figure 37: Ratio of Hall mobility to drift mobility versus temperature for Series B and C. In Series B, the ratio converges to 1.89 at low temperature and in Series C the ratio is approximately unity at high donor concentration.

density can be defined as

$$n_{cr} = N_c \mathcal{F}_{\frac{1}{2}}(0) \tag{59}$$

from Eq. (38), which indicates that FD statistics must be applied to a system with an electron density larger than this critical value. Thus, $n_{cr}(300K) = 1.34 \times 10^{18} cm^{-3}$, $n_{cr}(77K) = 1.75 \times 10^{17} cm^{-3}$ and $n_{cr}(25K) = 3.24 \times 10^{16} cm^{-3}$. This last value crudely corresponds to the critical donor concentration found, though compensation makes the two critical values differ.

Experimental Results

The experimental data by Park and Simmons [87] are listed below for a qualitative comparison to the present theory. The experiments are on heavily doped and intermediately doped n-ZnSe semiconductors. Table 9 enumerates the impurity concentrations for all six samples. For convenience, the ratio of acceptor concentration to donor concentration is also calculated in the table.

The chemical potential for Sample 2-5 are measured and Sample 5 is metallic as it stays within the conduction band, as shown in Fig. 38, and its free-electron density is

Table 9: Donor and Acceptor Concentrations in the Experiments [87].

Sample	$N_d\,(10^{16} cm^{-3})$	$N_a\,(10^{16} cm^{-3})$	$\frac{N_a}{N_d}$
1	2.6	0.9	0.35
2	4.6	1.4	0.30
3	20.5	7.7	0.37
4	61.0	35.0	0.57
5	153.0	103.0	0.67
6	2370.0	1510.0	0.64

a constant and high, as shown in Fig. 39. Sample 4 shows a crossover behavior while the other two samples remains semiconducting.

The free electron density behaves distinctively in different phase: in the metallic phase, the density does not change with temperature, however, in the semiconducting phase, freeze-out and saturation regimes are distinguishable. All samples have been measured for their free electron density, and Sample 1 and 2 display semiconducting behavior, Sample 5 and 6 exhibit metallic trait, with Sample 3 and 4 showing deviation towards metallic characteristics though remaining semiconducting, as shown in Fig. 39.

Also measured for all the samples is the dependence of the Hall mobility on temperature. Sample 5 and 6 show metallic behavior in a heavily doped system, *i.e.*, independent of temperature. The other samples show temperature dependence similar to intermediately doped systems. At high temperature, the phonon contribution dominates and the mobility decreases with temperature as the magnitude of the characteristic wavevector of phonons increases. However, at low temperature, the phonon population drops and ionized impurities dominate the momentum-loss processes of free carriers. The momentum-loss process due to ionized impurity scatterings depends upon the characteristic energy and momentum of the carrier, as shown in Eq. (54), which increases with temperature. Hence, the mobility increases with temperature. The crossover temperature from phonon domination to ionized impurities domination increases with impurity concentration.

Qualitative comparison of these experimental data with the results of this research follows. Comparing Figs. 38, 33, 39, and 34, similarities are seen between the experimental data and the results for Series C with the present theory. For instance, between Sample 4 and the calculations with donor concentration of $10^{17} cm^{-3}$ and

$10^{18} cm^{-3}$ for Series C, all of them show crossover behavior in chemical potential and the free electron density varies with temperature in the same style. However, from the limited experimental data on low temperature Hall mobility, the disagreement is overwhelming between experiments and theory at high donor concentration. Not only the theoretical prediction is many orders of magnitude larger than the experimental data, but also they completely differ in their temperature dependence. The possible causes for disagreements will be discussed in the next chapter.

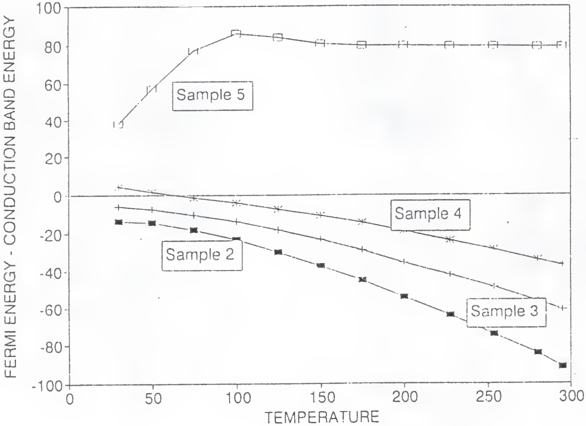

Figure 38: Measured chemical potential for *n*-ZnSe [87].

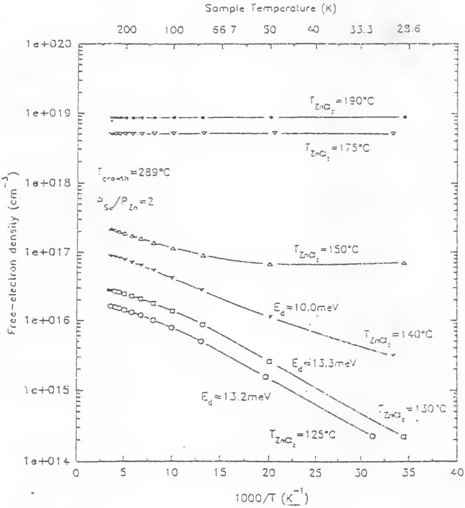

Figure 39: Measured free-electron density for *n*-ZnSe [87].

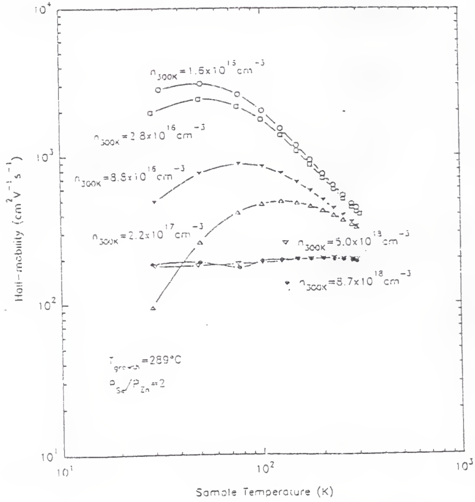

Figure 40: Measured Hall mobility versus temperature for *n*-ZnSe [87].

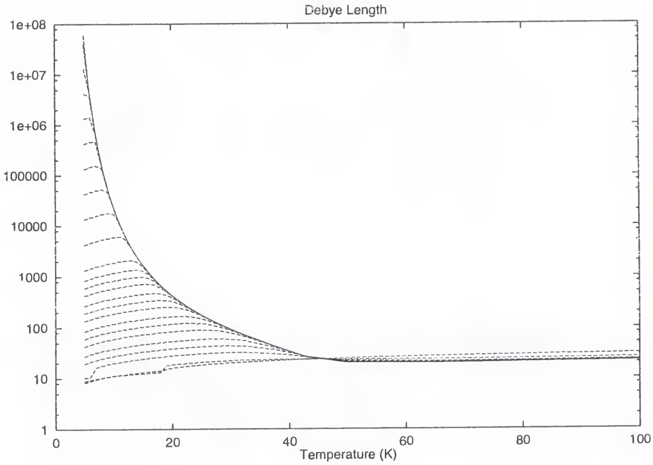

Figure 41: Debye length versus temperature for Series A with linear functional form for donor level.

CHAPTER 16
DISCUSSION

First of all, the static screening effect is not negligible[1] in semiconductors even at a donor concentration as low as $10^{15} cm^{-3}$, as suggested in Fig. 30. The critical parameter is the ratio of the Debye length to the donor hydrogenic radius for the n-type semiconductor. For III-V and II-VI semiconductors, the donor hydrogenic radius, as estimated by assuming that the relative effective mass is *0.1* and the relative dielectric constant is *10*, is one hundred times of the Bohr radius, according to $a_H^d = .529\kappa/m_e^*$. Thus, a Debye length with a value of thousands Å will modify donor level appreciably, according to Eq. (44–45). This means that impurities can change the physical properties of the host material at a much lower concentration than the critical concentration for metal-insulator transition.

The static screening effect modifies material parameters and may induce a phase transition. The Debye length affects the impurity levels. Thermodynamic equilibrium of the independent particle system, as considered in the present theory, is related to compensation and thermal excitations which are directly influenced by impurity levels. The two physical processes determine the Debye length. This nonlinear enhancement of screening may lead to critical behavior, as shown in the previous chapter. As for those controlling factors for the *critical temperature*, which no analytical expression has been found, calculations have been done concerning the functional form of the donor level reduction, *i.e.*, Eq. (44–45), dielectric constant, and the initial donor level. It is found that change of the functional form from quadratic to linear form diminishes the transition, as shown in Fig. 41. The dielectric constant κ is artificially varied without adjusting E_d^0 accordingly and the *critical temperature* diverges when lowering κ and saturates towards about *22 K* when increasing κ. When only varying E_d^0, since E_a^0 has no effect on the *critical temperature* as expected and checked, it shows that the temperature roughly varies linearly. Thus, we guess that the *critical temperature* is linearly proportional to the donor level E_d^0, as intuitively expected.

---

[1] It has been observed that the donor binding energy vanishes for impurity concentrations as low as $10^{14} cm^{-3}$ in InSb (see reference 98).

The chemical potential varies in the parametric space and strongly affects the screening capability of the doped semiconductor. The screening effect depends, primarily, upon the accessibility of those charged and thermodynamically active particles, which is determined by the chemical potential. This nonlinear relationship means that it is not plausible to assume a constant chemical potential when dealing with charged particles. Therefore, self-consistency is enforced in studying the whole parametric space.

Also, the chemical potential is directly related to the generation of free carriers, and the current-carrying capability of the doped material. Thus, it is desired to increase the efficiency of generating free charge carriers with doping. However, adding acceptors to an n-type semiconductor results in both increase of ionized impurities and lowering of the chemical potential. As a consequence, this leads to decrease in mobility and free carrier concentration. Therefore, *it is impossible to dope an intrinsically compensated semiconductor efficiently, unless making the material uncompensated.*

The present theory shows, partially and qualitatively, agreement behavior with the experimental data. Several elements hinder attempt of quantitative analysis of the experimental data. Firstly, the present theory does *not* have any fitting material parameters. For example, the donor and acceptor levels are computed self-consistently, not as fitting parameters. Furthermore, The experiments [87] for *n*-ZnSe, which is an intrinsically compensated semiconductor, do *not* have reliable data for impurity concentrations. Last but not the least, no low-temperature mobility data for ZnSe are available for comparison where the ionized impurity contribution predominates.

Several issues [96] may affect the outcome of the present theory. Discussed here are several important ones. First of all, the generalized Debye theory treats static screening perturbatively which definitely overestimates the effect, especially at high donor concentrations and MI transition region. For instance, the theoretical mobilities are not only three orders of magnitude higher than the measured values but also show different temperature dependence at high donor concentration (see Figs. 35 and 40). New experimental data (see reference 28, page 88) on high-quality, Cl-doped, uncompensated *n*-ZnSe/GaAs show a high free-electron density up to $10^{19} cm^{-3}$, semiconducting behavior, and *no* MI transition, which indicate (1) the Debye theory does overestimate static screening and (2) static screening is important, as deduced from the high carrier concentration. But this does *not* rule out possible MI transitions in other materials due to static screening effect [98]. For static electronic screening at high density, many-body theory, such as random phase approximation (RPA), may be adopted [99]. Secondly, in the present theory, acceptors are completely compensated and no correlations at high concentrations between impurities are considered. Furthermore, impurity states are treated by the hydrogenic model. Only ground states for the hydrogen-like impurities are taken into account in the present theory but excited states exist in real systems. In addition, impurities may be doubly occupied. All these would effectively reduce the static screening due to impurities at low temperature since the impurities may not be ionized when perturbed, or excited. Another assumption made in this research is homogeneity of impurities in the system. In real semiconductors, inhomogeneity exists, which will appreciably broaden DOS distributions for both electrons and impurities at high concentrations. This would lead to increase of static screening as the mini-gap between the donor levels (or band) and conduction band shrinks. The most important issue, however, is that, at high donor concentration, the system can not be treated as an ensemble of independent impurities since correlation between impurity states must be considered. In this case, many-body theory is needed to correctly treat the system. All of these issues may influence the nature of physics involved and/or alter the results of this research. It is not true, however, to imply that this research can not used at high donor concentration. As the new ZnSe/GaAs data (see reference 28, page 88) suggest, static screening will effectively reduce correlations in the system at high donor concentration such that the system still behaves as a non-degenerate semiconductor. However, considerations do have to be taken to account for the overestimate of the static screening effect, especially for the static-screening-induced MI transition. The present theory does agree with most of the experimental data. Other than these major issues, the following considerations may improve the present theory: (1) Born approximation may be replaced by more accurate partial wave phase-shift analysis; (2) bandstructure effect may be included at high carrier density; and (3) multi-scattering events may be considered in BKE.

Finally, this research is restricted to ionized impurity scatterings. However, at low temperature, neutral impurity scatterings may become important, which would smear out the critical behavior in mobility in certain parametric region. Also, as temperature rises, phonon contributions compete with impurity contributions and could predominate beyond *50 K* for semiconducting systems. Therefore, full consideration of all major scattering mechanisms is required to model the mobility data in the whole temperature range.

CHAPTER 17
CONCLUSIONS

As shown in this research, static screening effect plays an important role in determining the physical properties of intermediately to heavily doped semiconductors, especially compensated ones. For *n*-ZnSe is an intrinsically compensated semiconductor, it is imperative to treat the static screening in a self-consistent manner. A generalized Debye theory is adopted for this purpose and the analytical result of the Hulthén potential for impurity levels is used. The drift and Hall mobility are obtained by solving the Boltzmann kinetic equation under the *relaxation time approximation* and the *relaxation time* is derived quantum mechanically from the Born approximation.

Static screening effect is determined by compensation and thermal ionization of donor impurities in *n*-ZnSe. In compensated *n*-ZnSe, at low temperature, compensation creates ionized donors and acceptors, which effectively enhances the screening capability and thus changes the characteristics of the system. And as temperature rises, thermal ionization influences the system to certain degree that is dependent on compensation ratio. In contrast, in uncompensated *n*-ZnSe, above donor concentration of approximate $10^{17} cm^{-3}$, a well-defined MI transition occurs at *26.5 K*, but is smeared out when compensation increases. However, no such transition is observed experimentally, which leads the author to conclude that *the Debye theory over-estimates the static screening at high donor concentration* when the screening is strong. And the theory is applicable to a weakly screened system with its Debye length at least five times larger than the donor hydrogenic radius. Better nonlinear screening theory is needed at high donor concentration. Nevertheless, the results in this research are completely acceptable at temperatures and donor concentrations away from the transitional region.

It is found that static screening effect greatly affects carrier generation and mobility of the system even when donor concentration is far below the critical concentration for metal-insulator phase transition. Carrier density is reduced by an order of magnitude when compensation increases at high donor concentration. Therefore, it is essential to avoid compensation in semiconductors in order to achieve high doping efficiency at high donor concentration. Mobility is reduced by doping, and its temperature dependence, in highly compensated systems, changes from positive to negative relationship.

Finally, this research partially explains the experimental data by Park and Simmons. The chemical potential and free electron density data are well understood by the present theory at intermediate doping. Characteristically, the chemical potential decreases with temperature, and increases with donor concentration. And the electron density increases with temperature in the freeze-out regime and remains constant in the saturation regime. However, the mobility data differ in magnitude and behavior, which further corroborate the author's conclusion that the Debye theory over-estimates the static screening at high donor concentration.

PART V
CONCLUDING REMARKS

CHAPTER 18
SUMMARY

Given the technological importance of widegap semiconductors, it is highly desired to advance the knowledge of these materials, both individually and collectively. Despite the great diversity in characteristics and applications of semiconducting materials, there are often cases where systematic understanding is achieved. For example, the dielectric bonding theory of Philips and Van Vechten [6] explains, semi-quantitatively, how the physical properties, such as the elastic constants of CdTe, of tetrahedral semiconductors vary according to their degree of ionicity. However, more often than not, situations arise where prior systematic understanding lacks for the specific system, such as for deep impurities in phosphors. Then investigations of case after case may be needed to acquire the systematic knowledge.

This research is intended, through case studies, to understand some aspects of the widegap semiconductors when the materials are subjected to external influences, such as quantum confinement and doping. Specifically, modelling of optical reflectivity and XPS spectrum assists the implementation of bandstructure calculations and determining possible candidates for blue/green electroluminescent phosphors. Two salient features in an excellent candidate are required: a large bandgap (*3.7 eV*) and concentrated density of states for superhot electrons (at *3 eV*). Also, the modelling of quantum confinement effect on the absorption edge energy of semiconducting crystallites embedded in a transparent glass matrix leads to the realization that bandstructure effect dominates the contributions to the blue shift of absorption edge of quantum dots. This knowledge is useful in future selection of excellent nonlinear optoelectronic materials. Furthermore, the investigation of static screening effect in intermediately to heavily doped *n*-ZnSe proves that the effect is indeed important in determining the characteristics of the system. In particular, it is shown that compensation reduces carrier concentration and increases screening capability of the system. Thus, only high-quality, uncompensated semiconductors are capable of efficient generation of free carriers, which is of great importance in improving the reliability of *p-n* type injection devices and implementation of excellent ohmic contacts.

It is the aim of basic research to be able to direct future development by studying existing examples, which is a process of accumulation of knowledge. Throughout this research into several widegap semiconductors, various properties of them are computed from prior knowledge of their electronic structures in the bulk state. This systematic method relies upon the extraction of the electronic structures from known experimental data. This research fulfilled a tiny loop of this endless process of accumulation of human knowledge, *i.e.*, application of the accumulated knowledge to analyze new data and in return accumulation of new knowledge. This is what basic research is all about. And it is what this research is all about.

APPENDICES

APPENDIX A
EMPIRICAL 30 × 30 $\vec{k}\cdot\vec{p}$ THEORY [81]

The $\vec{k}\cdot\vec{p}$ method perturbatively obtains the electronic structure for a semiconductor on the basis of *a priori* knowledge about energy states at a high symmetry point of $\vec{k}$ space, which usually is the Γ point, the Brillouin zone center. Its basis set of *30* wavefunctions covers an energy range of over *30 eV* and assures an accurate description of the most relevant valence and conduction bands in applications. However, lack of consideration of the periodic symmetry in the reduced Hamiltonian lowers its accuracy away from the Γ point.

Reduced Schrödinger Equation

An electron follows the Schrödinger equation (60), in the independent electron approximation, as it moves in the periodic lattice of a semiconductor. As a consequence, the Bloch theorem allows us to rewrite Eq. (60) in terms of the periodic part of the wavefunction, $u_{n\vec{k}}(\vec{r})$, as equation (65).

$$H\psi_{n\vec{k}}(\vec{r}) = E_n\left(\vec{k}\right)\psi_{n\vec{k}}(\vec{r}) \tag{60}$$

$$H = H_0 + V^{asym}(\vec{r}) + H_{so} \tag{61}$$

$$H_0 = -\frac{\hbar^2\nabla^2}{2m} + V^{symm}(\vec{r}) \tag{62}$$

$$H_{so} = (\frac{\alpha}{2})^2\{\nabla V(\vec{r}) \times \vec{p}\}\cdot\vec{\sigma} \tag{63}$$

$$\psi_{n\vec{k}}(\vec{r}) = u_{n\vec{k}}(\vec{r})e^{i\vec{k}\cdot\vec{r}} \tag{64}$$

where the lattice potential, $V(\vec{r})$, has been separated into a symmetric part, $V^{symm}(\vec{r})$, and an antisymmetric part, $V^{asym}(\vec{r})$, with respect to the interchange of the anion atom and the cation atom in the semiconductor, and H_{so} is called the spin-orbital coupling term, which is negligible for compounds that consist of elements of small atomic weight.

$$Hu_{n,\vec{k}}(\vec{r}) + \frac{\hbar\vec{k}}{m} \cdot \vec{p}u_{n,\vec{k}}(\vec{r}) = \left(E_n\left(\vec{k}\right) - \frac{\hbar^2\vec{k}^2}{2m}\right)u_{n,\vec{k}}(\vec{r}) \tag{65}$$

Basis Functions

To solve Eq. (65), an empirical $\vec{k} \cdot \vec{p}$ method has been developed [81]. This method is based upon group theory, which allows the parameterization of the Hamiltonian if a basis set of functions $\left\{v_{n,\vec{0}}(\vec{r}),\ n = 1, \cdots, 15\right\}$, which are eigenfunctions of H_0, is used for expanding $u_{n\vec{k}}(\vec{r})$.

$$H_0 v_{n,\vec{0}}(\vec{r}) = \epsilon_n\left(\vec{0}\right) v_{n,\vec{0}}(\vec{r}), \quad n = 1, \cdots, 15 \tag{66}$$

where $\epsilon_n\left(\vec{0}\right)$, $n = 1, \cdots, 15$ are the energy levels at the Γ point and the number of 15 states is purely the result of the group theory of O_h point symmetry and a way of empirical thinking. It is enough to consider only contributions from the following states where the superscripts l and u in state labels stand for lower and upper states. Therefore, only eight energy parameters are needed for semiconductors of a zincblende or diamond crystalline structure.

When the degrees of freedom of spins are considered, the number of basis functions doubles, which is why the theory counts 30 states. Also, it is worth mentioning that the empty lattice model supplies a good starting point to understand the origin of these basis states.

Table 10: Empirical 30 × 30 $\vec{k}\cdot\vec{p}$ Theory Basis States

state	Γ_1^l	Γ_1^u	$\Gamma_{2'}^l$	$\Gamma_{2'}^u$	$\Gamma_{25'}^l$	$\Gamma_{25'}^u$	Γ_{15}	$\Gamma_{12'}$
degeneracy	1	1	1	1	3	3	3	2

Matrix Elements

Thanks to the Wigner-Eckart theorem, the number of parameters in the $\vec{k}\cdot\vec{p}$ method becomes manageable. The theorem can be expressed as

$$\langle v_k^{(\gamma)} | P_i^{(\alpha)} | v_j^{(\beta)} \rangle = c^*(\gamma\alpha\beta; kij)\, \tilde{P} \tag{67}$$

where $v_k^{(\gamma)}$ is the *k*-th function that belongs to the γ representation of the group of the system, $c^*(\gamma\alpha\beta; kij)$ are the coupling coefficients that are entirely related by the symmetry, and $\tilde{P}$ depend upon the physical properties of the particular operator $P^{(\alpha)}$, which transforms according to the α-th representation of the group of the system, but completely independent of the quantum numbers *i*, *j*, *k*. These coupling coefficients, often called the Clebsch-Gordon or Wigner coefficients, can be found in reference 100 for the thirty-two point groups.

Applications of the Wigner-Eckart theorem to the linear momentum operator, the antisymmetric potential, and the spin-orbital coupling term result in the full parameterization of the Hamiltonian *H*, and Tables 11-13 list the notation of parameters for all the matrix elements. To express all the operators in Eq. (65) in terms of these parameters, following knowledge is necessary. In O_h group, linear momentum transforms like $\Gamma_{25'}$;

the antisymmetric potential transforms like $\Gamma_{2'}$; and the angular momentum transforms like Γ_{15}. Also, the contribution from the antisymmetric potential in the spin-orbital coupling term is neglected because the linear momentum in the lattice of a solid is much less than in atoms and calculations [75] have justified this. Furthermore, it is customary to take V_6^- to zero since the involved states are far apart in energy. Therefore, the number of adjustable parameters in the empirical 30×30 $\vec{k} \cdot \vec{p}$ theory is 27.

All parameters in the 30×30 $\vec{k} \cdot \vec{p}$ theory for ZnS, ZnSe, CdTe are fitted by Sanders and the author and are listed in Table 3 in the present thesis.

Table 11: Linear Momentum Parameters for 30 × 30 $\vec{k} \cdot \vec{p}$ Theory

P/2	Q/2	R/2	P''/2	P'/2	Q'/2	R'/2	P'''/2	T/2	T'/2
$\langle\Gamma^l_{25'}\|P\|\Gamma^l_{2'}\rangle$	$\langle\Gamma^l_{25'}\|P\|\Gamma_{15}\rangle$	$\langle\Gamma^l_{25'}\|P\|\Gamma_{12'}\rangle$	$\langle\Gamma^l_{25'}\|P\|\Gamma^u_{2'}\rangle$	$\langle\Gamma^u_{25'}\|P\|\Gamma^l_{2'}\rangle$	$\langle\Gamma^u_{25'}\|P\|\Gamma_{15}\rangle$	$\langle\Gamma^u_{25'}\|P\|\Gamma_{12'}\rangle$	$\langle\Gamma^u_{25'}\|P\|\Gamma^u_{2'}\rangle$	$\langle\Gamma^u_1\|P\|\Gamma_{15}\rangle$	$\langle\Gamma^l_1\|P\|\Gamma_{15}\rangle$

Table 12: Antisymmetric Potential Parameters for 30 × 30 $\vec{k} \cdot \vec{p}$ Theory

V_1^-	V_2^-	V_3^-	V_4^-	V_5^-	V_6^-
$\langle\Gamma_{15}\|V^-\|\Gamma^l_{25'}\rangle$	$\langle\Gamma^l_{2'}\|V^-\|\Gamma^u_1\rangle$	$\langle\Gamma^l_{2'}\|V^-\|\Gamma^l_1\rangle$	$\langle\Gamma_{15}\|V^-\|\Gamma^u_{25'}\rangle$	$\langle\Gamma^u_{2'}\|V^-\|\Gamma^u_1\rangle$	$\langle\Gamma^u_{2'}\|V^-\|\Gamma^l_1\rangle$

Note: V^- is an abbreviation for V^{asym}.

Table 13: Spin-orbital Coupling Parameters for 30 × 30 $\vec{k} \cdot \vec{p}$ Theory

$\Delta_{25'}$	Δ_{15}	Δ^-
$3i\langle\Gamma^l_{25'}\vert\tilde{H}_{so}\vert\Gamma^l_{25'}\rangle$	$3i\langle\Gamma_{15}\vert\tilde{H}_{so}\vert\Gamma_{15}\rangle$	$3\langle\Gamma^l_{25'}\vert\tilde{H}_{so}\vert\Gamma_{15}\rangle$

Note: For convenience, $\tilde{H}_{so}$ is introduced, which is defined as

$$\tilde{H}so = \left(\frac{\alpha}{2}\right)^2 \left[\nabla V(\vec{r}) \times \vec{P}\right]$$

that transforms as the angular momentum under O_h group.

APPENDIX B
GILAT-RAUBENHEIMER SCHEME

Numerical calculations involving an integration over the whole Brillouin Zone (BZ) may be performed efficiently in two ways: (1) the special $\vec{k}$-point scheme [101] or (2) the Gilat-Raubenheimer (GR) scheme [102, 103]. The latter scheme has been applied in the computations of frequency- or energy-distribution functions of phonons and electrons, which ranges from simple density of states functions to generalized magnetic susceptibilities, dielectric functions, photoemission energy distributions, *etc.* Both schemes allow fine details of the distribution functions, such as the critical points, to be determined as desired. The present appendix considers the cubic systems, though it can be generalized to more complicated systems.

The cubic symmetry reduces the integration over the BZ into an integral involving only one-forty-eighth of the zone, *i.e.*, the irreducible Brillouin Zone. The GR scheme systematically breaks the irreducible BZ, as depicted in figure 42, into tetrahedra so that, within each individual tetrahedron, an analytical interpolation can be applied to simplify the dispersion curves. As a result, fast numerical implementation, thus the description of fine details of the distribution functions, becomes possible.

First of all, the irreducible BZ, labeled as ΓKWXUL by using its vertex symbols, is divided into three main tetrahedra ($itetr = 1, 2, 3$), labeled as ΓLKW, ΓLWU, and ΓUWX. Then, each of these main tetrahedra is partitioned, according to [102], into smaller tetrahedra ($i = 1, \cdots, n$) where n is the number of small tetrahedra in each of the main tetrahedra, ΓLKW, ΓLWU, and ΓUWX. Within each of the subsequent tetrahedra, dispersion curves are linearly interpolated as

$$\epsilon_n(\vec{k}) = \epsilon_n(\vec{k}_{icorn}) + \nabla_{\vec{k}}\epsilon_n(\vec{k})|_i \cdot (\vec{k} - \vec{k}_{icorn}) \,, \tag{69}$$

where $ivtx = 1, \cdots, 4$ numbers the four vertices of the tetrahedron. Consequently, equations (70) and (71) are derived for each basic tetrahedron so that a BZ integral of any slowly varying functions at the lengthscale of the lattice constant is converted into a summation over the number of basic tetrahedra.

$$\int_{tetr} \frac{2d^3k}{v}\,\delta\left(E - \epsilon_n\left(\vec{k}\right)\right) \approx$$
$$\begin{cases} 0\,, & E \leq \epsilon_4 \\ \frac{(E-\epsilon_4)^2}{(\epsilon_3-\epsilon_4)(\epsilon_2-\epsilon_4)(\epsilon_1-\epsilon_4)}\,, & \epsilon_4 < E \leq \epsilon_3 \\ \frac{(E-\epsilon_4)^2}{(\epsilon_3-\epsilon_4)(\epsilon_2-\epsilon_4)(\epsilon_1-\epsilon_4)} - \frac{(E-\epsilon_3)^2}{(\epsilon_3-\epsilon_4)(\epsilon_2-\epsilon_3)(\epsilon_1-\epsilon_3)}\,, & \epsilon_3 < E \leq \epsilon_2 \\ \frac{(E-\epsilon_1)^2}{(\epsilon_1-\epsilon_4)(\epsilon_1-\epsilon_3)(\epsilon_1-\epsilon_2)}\,, & \epsilon_2 < E < \epsilon_1 \\ 0\,, & E \geq \epsilon_1 \end{cases} \tag{70}$$

where $\epsilon_{ivtx}, ivtx = 1, \cdots, 4$ are the values of $\epsilon_n\left(\vec{k}\right)$ at the corresponding vertices, v is the volume of the tetrahedron, and $\epsilon_4 \leq \epsilon_3 \leq \epsilon_2 \leq \epsilon_1$ has been assumed as well.

$$\int_{tetr} \frac{d^3k}{\epsilon_n\left(\vec{k}\right) - E} \approx 3v\left(\frac{V_1^2}{D_1}\ln\left|\frac{V_1}{V_4}\right| + \frac{V_2^2}{D_2}\ln\left|\frac{V_2}{V_4}\right| + \frac{V_3^2}{D_3}\ln\left|\frac{V_3}{V_4}\right|\right) \tag{71}$$

where $V_{ivtx} = \epsilon_{ivtx} - E$, $ivtx = 1, \cdots, 4$ and $D_{ivtx} = \prod_{jvtx=1}^{4}{}' (V_{ivtx} - V_{jvtx})$ with the prime sign denoting that $jvtx \neq ivtx$ in the product. Care has to be taken when treating the above expression for the special cases when some of the V_{ivtx}'s are zero or equal.

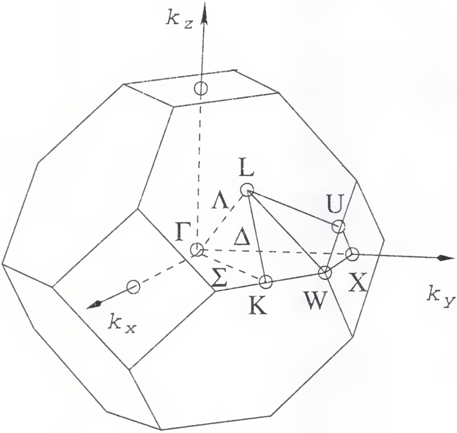

Figure 42: Brillouin Zone of face-center-cubic (FCC) and zincblende lattices.

APPENDIX C
GENERALIZED DEBYE THEORY

Basics

At thermodynamic equilibrium, we assume distribution function $f_i(E)$ for charged entity of type i at energy E. The density of charged entity of type i at energy E is given as

$$n_i(E) = g_i(E) f_i(E) \tag{72}$$

where $g_i(E)$ is the density of states at energy E. When a perturbative electric potential $V(\vec{r})$ is applied, the density of charged entity of type i used to at energy E changes to

$$n_i(E) = g_i(E) f_i[E + \bar{e}_i V(\vec{r})] \tag{73}$$

where the symbol $\bar{e}_i$ contains the sign of the charge. And we still use the old energy to label energy states. Therefore, the resultant total charge density is given as

$$\rho(\vec{r}) = \sum_i \int dE\, \bar{e}_i g_i(E) \{ f_i[E + \bar{e}_i V(\vec{r})] - f_i(E) \} . \tag{74}$$

The electric potential satisfies Poisson's equation, which reads,

$$\begin{aligned} \nabla^2 V(\vec{r}) &= -\frac{\rho(\vec{r})}{\epsilon} \\ &= -\sum_i \int dE\, \frac{\bar{e}_i}{\epsilon} g_i(E) \{ f_i[E + \bar{e}_i V(\vec{r})] - f_i(E) \} . \end{aligned} \tag{75}$$

First order Taylor expansion on the perturbative electric potential reduces Eq. (75) into

$$\nabla^2 V(\vec{r}) = -\frac{e^2}{\epsilon} V(\vec{r}) \sum_i \int dE\, g_i(E) \frac{\partial f_i(E)}{\partial E} , \tag{76}$$

which allows us to define the generalized Debye length λ_D as

$$\begin{aligned} \lambda_D^{-2} &= -\frac{e^2}{\epsilon}\sum_i \int dE\, g_i(E)\frac{\partial f_i(E)}{\partial E} \\ &= \frac{e^2}{\epsilon}\sum_i \left|\frac{\partial n_i}{\partial E_f}\right|, \end{aligned} \tag{77}$$

where n_i is the concentration of charged entities of type i, which is given by

$$n_i = \int dE\, g_i(E) f_i(E)\,. \tag{78}$$

In deducing the second part of Eq. (77) we assume that the chemical potential E_f depends upon the distribution function through $E - E_f$, as always true for independent particle systems where total energy is the sum of energies contributed by each individual particles. However, there is a catch in this deduction, that is, absolute values are taken for the derivatives The reason is simply because when real system is dealt, as in Part IV, energy reference can be changed, which may result in the negativeness of λ_D^{-2}. As a note, we use continuous notation for energy states above, which is only for convenience and can be easily generalized for discrete cases.

Following Ashcroft and Mermin [104], the relative dielectric constant $\kappa\left(\vec{k}\right)$ can be found using

$$\kappa\left(\vec{k}\right) = 1 - \frac{1}{\epsilon q^2}\frac{\rho\left(\vec{k}\right)}{V\left(\vec{k}\right)}, \tag{79}$$

where $\vec{k}$ is the wavevector in reciprocal space, $\rho\left(\vec{k}\right)$ is the $\vec{k}$-th Fourier component of the induced charge density given in Eq. (74), and $V\left(\vec{k}\right)$ is the $\vec{k}$-th Fourier component of the perturbative electric potential $V(\vec{r})$. The result, as well-known, is given below

$$\kappa\left(\vec{k}\right) = 1 + \frac{1}{\lambda_D^2 k^2}\,. \tag{80}$$

As easily seen, Eq. (77) corresponds to Eq. (43) for the specific doped semiconductor system we discussed. Also, this theory applies to both classical and quantum mechanical systems. The only condition, which is sufficient, is that the total energy of the system is the sum of all individual particle energies.

Applications of Generalized Debye Theory

A direct application of this theory on bare Coulomb potential $V(\vec{r}) = \frac{Z_i \bar{e}_i}{4\pi\epsilon r}$ gives the result of dressed Coulomb potential

$$V(\vec{r}) = \frac{Z_i \bar{e}_i}{4\pi\epsilon r} \exp\left(-\frac{r}{\lambda_D}\right). \tag{81}$$

Degenerate Electron Gas in 3D

For this given system, we have

$$f(E) = \frac{1}{1 + \exp\left[\beta(E - E_f)\right]} \tag{82}$$

and we assume parabolic energy dispersion for electrons, so

$$E_f \propto n^{\frac{2}{3}}; \qquad g(E_f) = \frac{3}{2}\frac{n}{E_f}, \tag{83}$$

where n is the electron concentration of the system, which is given by

$$n = \int dE\, g(E) f(E). \tag{84}$$

An approximation is used

$$\frac{\partial n}{\partial E_f} \approx \int dE\, g(E) \delta(E - E_f) = g(E_f) \tag{85}$$

so as to find an analytical expression for λ_D, which is given as

$$\lambda_D \propto n^{-\frac{1}{6}} \tag{86}$$

and independent of temperature.

Classical Electron Gas

In this case, the distribution function takes Maxwell-Boltzmann form

$$f(E) \propto \exp\left[-\beta(E - E_f)\right] \tag{87}$$

and no matter what energy dispersion for electrons is we have

$$\frac{\partial n}{\partial E_f} = \frac{\partial}{\partial E_f} \int dE\, g(E) C \exp\left[-\beta(E - E_f)\right] = \beta n \tag{88}$$

so that

$$\lambda_D \propto n^{-\frac{1}{2}} T^{\frac{1}{2}} \tag{89}$$

which is quite different from the previous case in its dependence on both the temperature and carrier concentration.

Singly Charged Donors

In the present case, the number of neutral donors is

$$N_d^x = \frac{N_d}{1 + \frac{1}{2} e^{-\beta(E_d + E_f)}} \tag{90}$$

according to Eq. (41) and we have

$$N_d^+ = \frac{N_d}{1 + 2e^{\beta(E_d + E_f)}} \,. \tag{91}$$

Therefore, it is easy to find that

$$\left|\frac{\partial N_d^+}{\partial E_f}\right| = \beta \frac{N_d^+ (N_d - N_d^+)}{N_d} \,, \tag{92}$$

and owing to the symmetry in their relationships, it is trivial to find the solution for the system of singly charged acceptors, for which we list the result

$$\left|\frac{\partial N_a^-}{\partial E_f}\right| = \beta \frac{N_a^- (N_a - N_a^-)}{N_a} \,. \tag{93}$$

BIBLIOGRAPHY

1. J. Bardeen and W. H. Brattain, Phys. Rev. **74**, 230 (1948).

2. J. Bardeen and W. H. Brattain, Phys. Rev. **75**, 1208 (1949).

3. W. Shockley, M. Sparks, and G. K. Teal, Phys. Rev. **83**, 151 (1951).

4. K. W. Böer, *Survey of Semiconductor Physics: Electrons and Other Particles in Bulk Semiconductors*, Van Nostrand Reinhold, New York, 1990.

5. R. G. Lerner and G. L. Trigg, editors, *Encyclopedia of Physics*, pages 1112-1120, VCH Publishers, New York, 2nd edition, 1991.

6. J. C. Philips, *Bonds and Bands in Semiconductors*, Academic Press, New York, 1973.

7. V. I. Fistul', *Heavily Doped Semiconductors*, Plenum Press, New York, 1969.

8. C. Weisbuch and B. Vinter, *Quantum Semiconductor Structures Fundamentals and Applications*, Academic Press, New York, 1991.

9. H. G. Grimmeiss, editor, *Heterostructures in Semiconductors*, Physica Scripta **T68**, 1996.

10. M. J. Kelly, Microelectronics Journal **24**, 723 (1993).

11. P. Butcher, N. H. March, and M. P. Tosi, editors, *Physics of Low-Dimensional Semiconductor Structures*, of *Physics of Solids and Liquids*, Plenum Press, New York and London, 1993.

12. R. K. Willardson and A. C. Beer, editors, *Applications of Multiquantum Wells, Selective Doping, and Superlattices*, volume 24 of *Semiconductors and Semimetals*, chapter 6, Academic Press, New York, 1987.

13. M. Reed, editor, *Nanostructured Systems*, volume 35 of *Semiconductors and Semimetals*, Academic Press, New York, 1992.

14. T. Ando, A. B. Fowler, and F. Stern, Rev. Mod. Phys. **54**, 437 (1982).

15. S. Wang, *Fundamentals of Semiconductor Theory and Device Physics*, pages 503-509, Prentice-Hall, London, 1989.

16. W. T. Tsang, editor, *Physics of Avalanche Photodiodes*, volume 22/D of *Semiconductors and Semimetals*, chapter 1, Academic Press, New York, 1985.

17. S. W. Depp and W. E. Howard, Scientific American **March**, 90 (1993).

18. R. K. Willardson and A. C. Beer, editors, *Optical Properties of III-V Compounds*, volume 3 of *Semiconductors and Semimetals*, Academic Press, New York, 1967.

19. K. von Klitzing, Rev. Mod. Phys. **58**, 519 (1986).

20. J. E. Avron, A. Raveh, and B. Zur, Rev. Mod. Phys. **60**, 873 (1988).

21. D. G. Seiler and C. L. Littler, editors, *The Spectroscopy of Semiconductors*, volume 36 of *Semiconductors and Semimetals*, Academic Press, New York, 1992.

22. A. Griffin, D. W. Snoke, and S. Stringari, editors, *Bose-Einstein Condensation*, page 246, Cambridge University Press, New York, 1995.

23. R. K. Willardson and A. C. Beer, editors, *Infrared Detectors*, volume 5 of *Semiconductors and Semimetals*, Academic Press, New York, 1970.

24. R. K. Willardson and A. C. Beer, editors, *Lightwave Communications Technology*, volume 22 of *Semiconductors and Semimetals*, Academic Press, New York, 1985.

25. R. K. Willardson and A. C. Beer, editors, *Mercury Cadmium Telluride*, volume 18 of *Semiconductors and Semimetals*, Academic Press, New York, 1981.

26. R. L. Gunshor and A. V. Nurmikko, editors, *II-VI Blue/Green Light Emitters: Device Physics and Epitaxial Growth*, volume 44 of *Semiconductors and Semimetals*, Academic Press, New York, 1997.

27. H. E. Ruda, editor, *Widegap II-VI Compounds for Opto-electronic Applications*, Chapman & Hall, London, 1992, Part Three.

28. H. E. Ruda, editor, *Widegap II-VI Compounds for Opto-electronic Applications*, of *Electronic Materials*, Chapman & Hall, London, 1992.

29. O. Madelung, editor, *Physics of II-VI and I-VII Compounds, Semimagnetic Semiconductors*, volume III/17b of *Landolt-Börnstein: Numerical Data and Functional Relationships in Science and Technology—New Series*, Springer-Verlag, Berlin, 1987.

30. J. A. Castellano, *Handbook of Display Technology*, Academic Press, San Diego, 1992.

31. W. R. Hunter, D. W. Angel, and G. Hass, J. Opt. Soc. Am. , 1319 (1978).

32. M. L. Cohen and J. R. Chelikowsky, *Electronic Structure and Optical Properties of Semiconducors*, volume 75 of *Solid-State Sciences*, Springer-Verlag, Berlin, 1988.

33. R. Mach and G. O. Müller, Phys. Stat. Sol. (a) **69**, 11 (1982).

34. R. Mach and G. O. Mueller, Semicon. Sci. Technol. **6**, 305 (1991).

35. S. Shionoya and H. Kobayashi, editors, *Electroluminescence: Proceedings of the Fourth International Workshop*, volume 387 of *Springer Proceedings in Physics*, Springer-Verlag, Berlin, 1989.

36. V. P. Singh and J. C. McClure, editors, *Electroluminescence*, Cinco Puntos Press, El Paso, 1992.

37. C. Cercignani, *Mathematical Methods in Kinetic Theory*, Plenum Press, New York and London, 1990.

38. J. M. Ziman, *Electrons and Phonons*, Oxford University, New York, 1960.

39. F. J. Blatt, *Physics of Electronic Conduction in Solids*, McGraw-Hill, New York, 1968.

40. E. M. Conwell, *High Field Transport in Semiconductors*, volume 9 (Suppl.) of *Solid State Physics*, Academic Press, New York, 1967.

41. B. R. Nag, *Electron Transport in Compound Semiconductors*, Springer-Verlag, Berlin, 1980.

42. J. Shah, editor, *Hot Carriers in Semiconductor Nanostructures: Physics and Applications*, Academic Press, Boston, 1992.

43. C. Jacoboni and P. Lugli, *The Monte Carlo Method for Semiconductor Device Simulation*, Springer, Wien, 1989.

44. K. Bhattacharyya, S. M. Goodnick, and J. F. Wager, J. Appl. Phys. **73**, 3390 (1993).

45. S. S. Pennathur, *Monte Carlo Device Modeling Applications on Parallel Computers*, PhD dissertation, Oregon State University, Corvallis, 1996.

46. G. D. Sanders, C.-K. Sun, J. G. Fujimoto, H. K. Choi, C. A. Wang, and C. J. Stanton, Phys. Rev. B **50**, 8539 (1994).

47. W. H. Press, S. A. Teukolsky, W. T. Vettering, and B. P. Flannery, *Numerical Recipes in FORTRAN: The Art of Scientific Computing*, Cambridge University Press, Cambridge, 1992.

48. R. M. Park, H. A. Mar, and N. M. Salansky, J. Appl. Phys. **58**, 1047 (1985).

49. H. E. Ruda, J. Appl. Phys. **59**, 1220 (1986).

50. K. Zanio, *Cadmium Telluride*, volume 13 of *Semiconductors and Semimetals*, Academic Press, New York, 1978.

51. B. G. Potter, *Electronic Band Structure and Optical Characteristics of Quantum-Size CdTe Crystals in Glass Films*, PhD dissertation, University of Florida, Gainesville, 1991.

52. D. Fiorani and G. Sberveglieri, editors, *Fundamental Properties of Nanostructured Materials*, World Scientific, Singapore, 1994.

53. J.-P. Leburton, J. Pascual, and C. S. Torres, editors, *Phonons in Semiconductor Nanostructures*, Kluwer Academic, Dordrecht and Boston, 1993.

54. J. Shah, editor, *Ultrafast Spectroscopy of Semiconductors and Semiconductor Nanostructures*, Springer, Berlin and New York, 1996.

55. H. Grabert and M. H. Devoret, editors, *Single Charge Tunneling: Coulomb Blockade Phenomena in Nanostructures*, Plenum Press, New York, 1992.

56. S. M. Prokes, R. C. Cammarata, K. L. Wang, and A. Christou, editors, *Surface/Interface and Stress Effects in Electronic Material Nanostructures*, volume 405, Materials Research Society, Pittsburgh, Pa., 1996.

57. M. Sarikaya, H. K. Wickramasinghe, and M. Isaacson, editors, *Determining Nanoscale Physical Properties of Materials by Microscopy and Spectroscopy*, volume 332, Materials Research Society, Pittsburgh, Pa., 1994.

58. B. G. Potter, Jr., J. H. Simmons, P. Kumar, and C. J. Stanton, J. Appl. Phys. **75**, 8039 (1994).

59. V. Sosa, P. D. Rack, and P. H. Holloway, submitted to J. Vac. Sci. Tech.

60. M. Cardona and L. Ley, editors, *Photoemission in Solids I and II*, volume 26 and 27 of *Topics in Applied Physics*, Springer-Verlag, Berlin, 1978, 1979.

61. F. Bassani and G. P. Parravicini, *Electronic States and Optical Transitions in Solids*, Pergamon, Oxford, 1975.

62. W. P. Halperin, Rev. Mod. Phys. **58**, 533 (1986).

63. S. S Nedorezov, Soviet Phys.—JETP **24**, 1061 (1967).

64. B. A. Tavger and V. Y. Demikhovskii, Soviet Phys.—USPEKHI **11**, 644 (1969).

65. S. S. Nedorezov, Soviet Phys.—Solid State **12**, 1814 (1971).

66. M. I. Kagnov, S. S. Nedorezov, and A. M. Rustamova, Soviet Phys.—Solid State **12**, 1820 (1971).

67. M. F. H. Schuurmans and G. W. 't Hooft, Phys. Rev. B **31**, 8041 (1985).

68. S. B. Zhang, C.-Y. Yeh, and A. Zunger, Phys. Rev. B **48**, 11 204 (1993).

69. J. M. Luttinger and W. Kohn, Phys. Rev. **97**, 869 (1955).

70. G. Bastard, *Wave Mechanics Applied to Semiconductor Heterostructures*, Halsted Press, New York, 1988.

71. A. Zunger, J. Phys. C **7**, 76 (1974).

72. A. L. Efros and A. L. Efros, Soviet Phys.—Semicond. **16**, 772 (1982).

73. G. Allan, G. Bastard, N. Boccara, M. Lannoo, and M. Voos, editors, *Heterostructures and Semiconductor Superlattices*, Springer-Verlag, Berlin and New York, 1985.

74. S. R. White and L. J. Sham, Phys. Rev. Lett. **47**, 879 (1981).

75. M. Cardona and F. Pollak, Phys. Rev. **142**, 530 (1966).

76. F. H. Pollak, C. W. Higginbotham, and M. Cardona, J. Phys. Soc. Japan **21**, 20 (1966).

77. M. Cardona, N. E. Christensen, and G. Fasol, Phys. Rev. B **38**, 1806 (1988).

78. M. Cardona, J. Phys. Chem. Solids **24**, 1543 (1963).

79. C. Aversa and J. E. Sipe, Phys. Rev. B **49**, 14542 (1994).

80. Y. C. Chang, Phys. Rev. B **37**, 8215 (1988).

81. R. K. Willardson and A. C. Beer, editors, *Physics of III-V Compounds*, volume 1 of *Semiconductors and Semimetals*, chapter 3, Academic Press, New York, 1966.

82. E. O. Kane, J. Phys. Chem. Solids **1**, 249 (1957).

83. J. M. Luttinger, Phys. Rev. **102**, 1030 (1956).

84. P. W. Anderson, Phys. Rev. **109**, 1492 (1958).

85. P. P. Edwards and C. N. R. Rao, editors, *The Metallic and Non-metallic States of Matter*, Taylor and Francis, London, 1985.

86. H. Fritzsche and D. Adler, editors, *Localization and Metal-Insulator Transitions*, Plenum Press, New York and London, 1985.

87. J. H. Simmons, W. A. Gobba, and C. J. Stanton, Transport Properties of *n*-ZnSe, presented at an ARPA/ONR URI REVIEW in "Visible Light Emitting Materials and Injection Devices" held in Gainesville, FL, May 26, 1993.

88. H. Brooks, *Advances in Electronics and Electron Physics*, volume 7, pages 85-182, Academic Press, New York, 1955.

89. E. M. Conwell and V. F. Weisskopf, Phys. Rev. **77**, 381 (1950).

90. M. Aven, D. T. F. Marple, and B. Segall, J. Appl. Phys. **32**, 2261 (1961).

91. D. T. F. Marple, J. Appl. Phys. **35**, 1879 (1964).

92. D. Theis, Physica Status Solidi (b) **79**, 125 (1977).

93. D. L. Rode, *Transport Phenomena*, volume 10 of *Semiconductors and Semimetals*, chapter 1, Academic Press, New York, 1975.

94. N. W. Ashcroft and N. D. Mermin, *Solid State Physics*, pages 581-582, Holt, Rinehart and Winston, New York, 1976.

95. H. Haug and S. W. Koch, *Quantum Theory of the Optical and Electronic Properties of Semiconductors*, pages 224-227, World Scientific, Singapore, 1990.

96. D. Chattopadhyay and H. J. Queisser, Rev. Mod. Phys. **53**, 745 (1981).

97. J. Singh, *Physics of Semiconductors and Their Heterostructures*, pages 336-338, McGraw-Hill, New York, 1993.

98. S. P. Li, W. F. Love, and S. C. Miller, Phys. Rev. **162**, 728 (1967).

99. D. J. W. Geldart and R. Taylor, Solid State Comm. **9**, 7 (1971).

100. G. F. Koster, *Properties of the Thirty-Two Point Groups*, M.I.T. Press, Cambridge, 1963.

101. J. Chen, *Calculation of Linear and Nonlinear Optical Susceptibilities in Wide Gap Semiconductors*, PhD dissertation, Ohio State University, Columbus, 1996.

102. W. A. Harrison, *Electronic Structure and the Properties of Solids: the Physics of the Chemical Bond*, pages 55-57, Dover, New York, 1989.

103. J. Rath and A. J. Freeman, Phys. Rev. B **11**, 2109 (1975).

104. N. W. Ashcroft and N. D. Mermin, *Solid State Physics*, pages 337-340, Holt, Rinehart and Winston, New York, 1976.

BIOGRAPHICAL SKETCH

Jianzhong Li was born on the 6th of October, 1963 in Guilin, Guangxi Zhuang Autonomous Region, the Peoples' Republic of China. He attended Guilin High School in Guilin, Guangxi, from 1977 to 1980. In the Fall of 1980 he entered Tsinghua University and received a B.S. degree in modern applied physics in June 1985. He then pursued graduate studies in the Physics Department at Peking University and in June 1988 he withdrew with a study certificate. After working at Sanming Science and Technology Consulting Services he came to the United States to continue his study in physics at the University of Florida in the Fall of 1989.

I certify that I have read this study and that in my opinion it conforms to acceptable standards of scholarly presentation and is fully adequate, in scope and quality, as a dissertation for the degree of Doctor of Philosophy.

Christopher J. Stanton

Christopher J. Stanton, Chairman
Professor of Physics

I certify that I have read this study and that in my opinion it conforms to acceptable standards of scholarly presentation and is fully adequate, in scope and quality, as a dissertation for the degree of Doctor of Philosophy.

K. A. Muttalib

Khandker A. Muttalib
Associate Professor of Physics

I certify that I have read this study and that in my opinion it conforms to acceptable standards of scholarly presentation and is fully adequate, in scope and quality, as a dissertation for the degree of Doctor of Philosophy.

John R. Klauder

John R. Klauder
Professor of Physics

I certify that I have read this study and that in my opinion it conforms to acceptable standards of scholarly presentation and is fully adequate, in scope and quality, as a dissertation for the degree of Doctor of Philosophy.

David H. Reitze
Assistant Professor of Physics

I certify that I have read this study and that in my opinion it conforms to acceptable standards of scholarly presentation and is fully adequate, in scope and quality, as a dissertation for the degree of Doctor of Philosophy.

Joseph H. Simmons
Professor of Materials Science
and Engineering

This dissertation was submitted to the Graduate Faculty of the Department of Physics in the College of Liberal Arts and Sciences, and to the Graduate School and was accepted as partial fulfillment of the requirements for the degree of Doctor of Philosophy.

December 1997

Dean, Graduate School

LD
1780
199 7
.L6928

UNIVERSITY OF FLORIDA
3 1262 08555 0464